ISSN: 2376-2136 (Print)
ISSN: 2376-2144 (Online)

Trends in Renewable Energy

Volume 5, Issue 2, August 2019

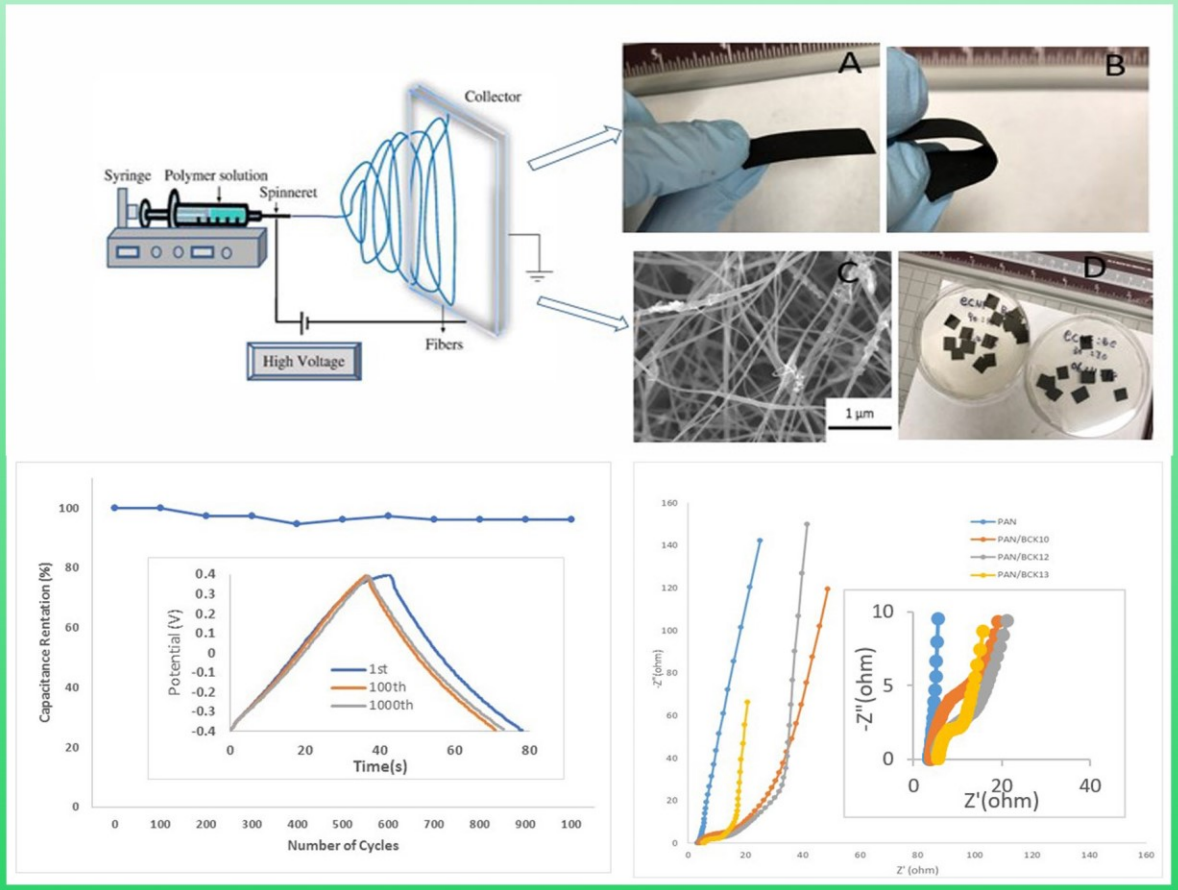

Cover image: A biochar-based supercapacitor, see article by Xiu et al. in this issue.

futureenergysp.com
thefutureenergy.org

Trends in Renewable Energy

ISSN: 2376-2136 (Print) ISSN: 2376-2144 (Online)

http://futureenergysp.com/

Trends in Renewable Energy is an open accessed, peer-reviewed semi-annual journal publishing reviews and research papers in the field of renewable energy technology and science.

The aim of this journal is to provide a communication platform that is run exclusively by scientists working in the renewable energy field. Scope of the journal covers: Bioenergy, Biofuel, Biomass, Bioprocessing, Biorefinery, Biological waste treatment, Catalysis for energy generation, Energy conservation, Energy delivery, Energy resources, Energy storage, Energy transformation, Environmental impact, Feedstock utilization, Future energy development, Green chemistry, Green energy, Microbial products, Physico-chemical process for Biomass, Policy, Pollution, Renewable energy, Smart grid, Thermo-chemical processes for biomass, etc.

The Trends in Renewable Energy publishes the following article types: peer-reviewed reviews, mini-reviews, technical notes, short-form research papers, and original research papers.

The article processing charge (APC), also known as a publication fee, is fully waived for the Trends in Renewable Energy.

Editorial Team of Trends in Renewable Energy

EDITORIAL BOARD

Dr. ALIASHIM ALBANI	School of Ocean Engineering, Universiti Malaysia Terengganu, Malaysia
Dr. Ashwini Kumar	Assistant Prof., College of Engineering, HSBPVT's Parikrama Group of Institutions, India
Dr. Hasan AYDOGAN	Associate Prof., Mechanical Engineering Department, Selcuk University, Turkey
Dr. Jiekang Wu	Professor, School of Automation, Guangdong University of Technology, China
Dr. Ong Huei Ruey	DRB-HICOM University of Automotive, Malaysia
Dr. Miguel Ángel Reyes Belmonte	IMDEA Energy Institute, Spain
Dr. Chitra Venugopal	Associate Professor in Electrical Engineering, University of Trinidad and Tobago, Trinidad
Dr. Amit Kumar Singh	Assistant Prof., Instrumentation & Control Engineering Department, Dr. B.R.A. National Institute of Technology, India
Dr. Suvanjan Bhattacharyya	University of Pretoria, South Africa
Dr. Karunesh Tiwari	Babu Banarasi Das University, India
Dr. Sharadrao A. Vhanalkar	Karmaveer Hire Arts, Science, Commerce and Education College, India
Dr. Prasenjit Chatterjee	Assistant Prof. and Head, MCKV Institute of Engineering, India
Dr. S. Balamurugan	Mindnotix Technologies, India
Dr. Mohammad Nurunnabi	University of Oxford, United Kingdom
Dr. Kenneth Okedu	Caledonian College of Engineering, Oman
Dr. Cheng Zhang	Sr. Materials Engineer, Medtronic, Inc., United States
Dr. Chandani Sharma	Assistant Prof., Department of Electrical Engineering, Graphic Era University, India
Dr. Kashif Irshad	Assistant Prof., Mechanical Engineering Department, King Khalid University, Saudi Arabia
Dr. Abhijit Bhagavatula	Principal Lead Engineer, Southern Company Services, United States
Dr. S. Sathish	Associate Prof., Department of Mechanical Engineering, Hindustan University, India
Mr. A. Avinash	Assistant Prof., KPR Institute of Engineering & Technology, India
Mr. Bindeshwar Singh	Assistant Prof., Kamla Nehru Institute of Technology, India
Dr. Yashar Hashemi	Tehran Regional Electric Company, Iran
Dr. Navanietha Krishnaraj R	South Dakota School of Mines and Technology, United States
Dr. SANDEEP GUPTA	JECRC University, India
Dr. Shwetank Avikal	Graphic Era Hill University, India
Dr. Xianglin Zhai	Poochon Scientific LLC, United States
Dr. Rui Li	Assistant Prof., College of Engineering, China Agricultural University, China
Dr. Adam Elhag Ahmed	National Nutrition Policy Chair, Department of Community Services, College of Applied Medical Sciences, King Saud University, Saudi Arabia
Dr. Jingbo Li	Massachusetts Institute of Technology, United States
Dr. Srikanth Mutnuri	Associate Prof., Department of Biological Sciences, Associate Dean for International Programmes and Collaboration, Birla Institute of Technology & Science, India
Dr. Bashar Malkawi	S.J.D., Associate Prof., College of Law, University of Sharjah, United Arab Emirates
Dr. Simona Silvia Merola	Istituto Motori - National Research Council of Naples, Italy
Dr. Hakan Caliskan	Faculty of Engineering, Department of Mechanical Engineering, Usak University, Turkey

Table of Contents

Volume 5, Issue No. 2, August 2019

Articles

Trends in Renewable Energy
OPEN ACCESS ISSN: 2376-2144
Peer-Reviewed Article futureenergysp.com/index.php/tre

The Role of Information Technology Department against the Hook Style Energy Theft in Smart Cities – Ad-Hoc Overhead Low-Voltage Broadband over Power Lines (OV LV BPL) Networks

Athanasios G. Lazaropoulos*

School of Electrical and Computer Engineering / National Technical University of Athens / 9 Iroon Polytechniou Street / Zografou, GR 15780

Received February 24, 2019; Accepted March 26, 2019; Published April 2, 2019

This paper investigates the possibility of detecting the hook style energy theft in the overhead low-voltage (OV LV) power grids through the hook style energy theft method (HS-DET method) when ad-hoc overhead Low-Voltage Broadband over Power Lines (OV LV BPL) networks are deployed by the Information Technology departments of the power utilities. Without the need for the deployment of a complete and permanent OV LV BPL network across the OV LV power grid, the impact of the deviation from the initial measurement positions and of longer ad-hoc OV LV BPL topologies on the detection efficiency of HS-DET method is assessed by using the already validated percent error sum (PES) metrics and appropriate contour plots.

Keywords: Smart Grid; Broadband over Power Lines (BPL); Power Line Communications (PLC); Distribution Power Grid; Energy Theft; Jamming; Robustness

1. Introduction

Energy theft defines a well-known problem either in traditional power systems or in the emerging smart grid while the financial losses of the power utilities reach up to $6 billion, $5 billion and $4.5 billion in United States, Brazil and India, respectively [1]-[10]. The existing portfolio of BPL broadband applications, such as Topology Identification Methodology (TIM) [11], Fault and Instability Identification Methodology (FIIM) [12], methodology to preserve power system stability [13]-[16] and Main Line Fault Localization Methodology (MLFLM) [17]-[19], that has been recently enriched with the hook style energy theft detection method (HS-DET method) [20]-[22] can monitor, meter, control and provide valuable real-time detailed information on actual operation of the power grid while it can identify and stop fraud (energy theft).

Until now [20]-[22], HS-DET method, which is based on the hybrid model [23]-[40], has been assumed to operate on the basis of a permanently installed BPL network while examining the permanent BPL cascaded topologies of this BPL network. In fact, HS-DET method adopts ΔPES metric, which is the suitable percent error sum (PES) submetric for energy theft detection, and its relevant contour plots in order to detect the hook style energy theft across the OV LV BPL topologies [20]-[22].

Corresponding author: AGLazaropoulos@gmail.com

Tr Ren Energy, 2019, Vol.5, No.2, 117-150. doi: 10.17737/tre.2019.5.2.0093

In this paper, to avoid the cost and the delay of a permanent installation of a BPL network, Information Technology departments of the power utilities can deploy ad-hoc OV LV BPL topologies so that an energy theft can be detected.

Actually, Δ*PES* and its relevant contour plots are going to be again exploited during the energy theft detection of ad-hoc OV LV BPL topologies since they are going to evaluate the asymmetry between the original and the modified ad-hoc OV LV BPL topology where the modified ad-hoc OV LV BPL topology comes from the original ad-hoc OV LV BPL topology after the hook insertion. However, the asymmetry evaluation implies that the Information Technology departments have already deployed the same ad-hoc OV LV BPL topologies during the normal operation of the power grid so that available measurements are available.

HS-DET method has first been presented in [20] where the impact of OV LV BPL topologies, hook characteristics and measurement differences on the performance of HS-DET method has been assessed through $\overline{\Delta PES}$ metric and its relevant contour plots. In [21], a first set of special issues, such as: (i) the existence / definition of a threshold of the intensity of measurement differences that may occur / be produced preventing faulty decisions concerning the existence of hook style energy theft; (ii) the impact of the installation of very long hooks; and (iii) the impact of the use of "smart" hooks, has been examined. In [22], a second set of special issues, such as: (a) the impact of different CUD measurement differences of the same maximum value when the coupling transfer functions of the original and the modified OV LV BPL topologies are measured; (b) the installation of two "smart" hooks; and (c) the impact of the full interconnection assumption of the "smart" hook during the computations of HS-DET method, has also been addressed. Taking into consideration the findings of [20]-[22] and the special nature of ad-hoc OV LV BPL topologies, a set of following issues related to the operation of ad-hoc OV LV BPL topologies is investigated in this paper, namely: (i) the effect of the deviation from the initial measurement positions of the installed ad-hoc OV LV BPL topology by the Information Technology department; and (ii) the effect of application of longer ad-hoc OV LV BPL topologies than the typical OV LV BPL topologies of the permanent BPL networks. The impact of the aforementioned two special features of the ad-hoc OV LV BPL topologies on the performance of the HS-DET method is assessed by using the already validated Δ*PES* and its appropriate contour plots.

The rest of this paper is organized as follows: In Section 2, a presentation of the proposed ad-hoc OV LV BPL topology installation concept is given as well as the required assumptions concerning the operation of ad-hoc OV LV BPL topologies. In Section 3, the synopsis of HS-DET method and PES metrics is presented. In Section 4, numerical results and discussion are provided, aiming at practically evaluating the performance of HS-DET method when ad-hoc OV LV BPL topologies are deployed.

2. Ad-hoc OV LV BPL Topologies

Ad-hoc OV LV BPL topologies are deployed upon the OV LV power grid resembling to the cascaded OV LV BPL topologies of the permanent BPL networks. A typical OV LV power grid consists of OV LV distribution power lines such as this of Fig. 1 of [20]. The dimensions of the OV LV multiconductor transmission line (MTL) configuration, the characteristics of the involved imperfect ground and the properties of

the BPL signal propagation / transmission through OV LV MTL configurations are detailed in [23], [25]-[29], [31]-[33], [41]-[46].

In the case of a permanent and complete BPL network installation, a BPL network can be divided into cascaded BPL topologies while in the case of the ad-hoc BPL topologies, which are studied in this paper, the ad-hoc BPL topology is synonym to the BPL network. In Fig. 1(a), a typical ad-hoc BPL topology with *N* branches, which does not differentiate from a typical BPL topology of a permanent BPL network, is shown. With respect to Fig. 1(a), an ad-hoc BPL topology is bounded by its transmitting and receiving ends. BPL units that operate as the transmitting and receiving ends are treated as the network gateways of the Information Technology department for its measurements. The number of branches and the topological characteristics of ad-hoc BPL topologies vary depending on the location of the examined segment of the OV LV power grid; say, this location defines the OV LV BPL topology class. In Table 1, the topological characteristics of indicative ad-hoc OV LV BPL topologies are reported. Note that same indicative ad-hoc OV LV BPL topologies with the indicative OV LV BPL topologies of typical lengths $D = \sum_{i=1}^{N+1}(L_i)$ of 1000 m are initially assumed in this paper (see [20]).

During the normal operation of the power grid, the Information Technology department should collect channel attenuation measurements from the examined ad-hoc OV LV BPL topology that is hereafter denoted as the original ad-hoc OV LV BPL topology. These measurements will also act as the reference measurements of the HS-DET method and should be properly handled by a database management system. Now, with reference to Fig. 1(b), let assume that a hook style energy theft occurs at the position A_h that is located at distance $D_h = L_h + \sum_{i=1}^{k-1}(L_i)$ from the transmitting end. The hook is located at distance $L_k - L_h$. from the *k*th branch while its length is equal to L_{bh}. In total, the modified ad-hoc OV LV BPL topology is illustrated in Fig. 1(b) with reference to the original ad-hoc OV LV BPL topology of Fig. 1(a).

Apart from the topological characteristics of Table 1, a set of assumptions concerning the transmission and propagation of the BPL signal as well as the circuital characteristics of the OV LV MTL configurations, which are required to simplify the following analysis, are detailed in [23]-[28]. Except for the aforementioned assumptions, assumptions concerning the hook handling should be made, namely:
(i) the hook termination is assumed to be open circuit; and
(ii) the hook interconnection with the distribution lines is assumed to be complete (*i.e.*, hook derivation points at the same distance from the transmitting end on all the three phases) and horizontal. Apart from the previous hook handling assumptions, no measurement differences are assumed in this paper. Although differentiations of the latter assumptions have been thoroughly examined and assessed in terms of the performance of the HS-DET method in [20]-[22], their simplest versions are assumed in this paper for the sake of the paper size reduction.

3. HS-DET Method Synopsis and the Ad-Hoc OV LV BPL Topology Case

3.1 Hybrid Model and BPL Signal Coupling

As the channel attenuation measurements of the Information Technology department are concerned, the hybrid model, which describes the BPL propagation and transmission, is here applied. Extensively analyzed in [23]-[29], [32],

hybrid model consists of two interconnected modules, say, the bottom-up and the top-down approach module, while several useful spectral efficiency metrics such as channel attenuation and capacity may be calculated. In accordance with the bottom-up approach of the hybrid model, the MTL configuration of the examined ad-hoc OV LV BPL topologies may support 4 modes that propagate across the MTL BPL configuration.

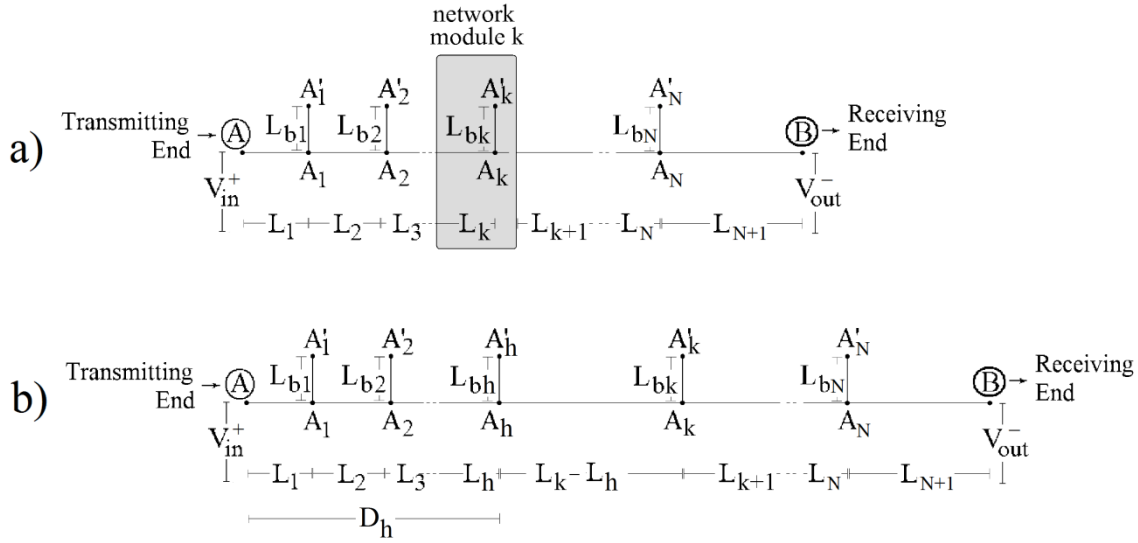

Fig. 1. (a) Typical original ad-hoc OV LV BPL topology with *N* branches [20]. (b) Typical modified ad-hoc OV LV BPL topology due to the hook insertion.

Table 1
Indicative Original Ad-Hoc OV LV BPL Topologies [20]

Topology Name (OV LV BPL Topology Class)	**Topology Description**	**Number of Branches**	**Length of Distribution Lines**	**Length of Branching Lines**
Urban case A	Typical OV urban topology	3	L_1=500m, L_2=200m, L_3=100m, L_4=200m	L_{b1}=8m, L_{b2}=13m, L_{b3}=10m
Urban case B	Aggravated OV urban topology	5	L_1=200m, L_2=50m, L_3=100m, L_4=200m, L_5=300m, L_6=150m	L_{b1}=12m, L_{b2}=5m, L_{b3}=28m, L_{b4}=41m, L_{b5}=17m
Suburban case	OV suburban topology	2	L_1=500m, L_2=400m, L_3=100m	L_{b1}=50m, L_{b2}=10m
Rural case	OV rural topology	1	L_1=600m, L_2=400m	L_{b1}=300m
"LOS" case	OV Line-of-Sight transmission	0	L_1=1000m	-

With reference to Figs. 1(a) and 1(b), through the combined operation of TM2 method, which is based on the scattering matrix formalism and is part of the top-down approach of the hybrid model [47], and CS2 module, which deals with the way that the BPL signal is injected onto and extracted from the OV LV lines and is also part of the top-down approach of the hybrid model [48], [49], the coupling scheme channel transfer function

that relates output BPL signal of the receiving end and input BPL signal of the transmitting end is given by

$$H^{\mathrm{C}}\{\cdot\} = [\mathbf{C}^{\mathrm{out}}]^{\mathrm{C}} \cdot [\mathbf{T}_{\mathrm{V}} \cdot \mathbf{H}^{\mathrm{m}}\{\cdot\} \cdot (\mathbf{T}_{\mathrm{V}})^{-1}] \cdot [\mathbf{C}^{\mathrm{in}}]^{\mathrm{C}} \quad (1)$$

where $\mathbf{H}^{\mathrm{m}}\{\cdot\}$ is the 4×4 modal channel transfer function matrix of the examined OV LV MTL configuration, $\mathbf{T}_{\mathrm{V}}^{\mathrm{C}}$ is a 4×4 matrix depending on the frequency, the examined distribution power grid type, the physical properties of the cables and the geometry of the MTL configuration, $\mathbf{C}^{\mathrm{in}}$ is the 1×4 input coupling vector, $\mathbf{C}^{\mathrm{out}}$ is the 4×1 output coupling vector and $[\cdot]^{\mathrm{C}}$ denotes the applied coupling scheme. In accordance with [48], [49], CS2 module may support three types of coupling schemes in ad-hoc OV LV BPL topologies, namely: (i) *Coupling Scheme Type 1: Wire-to-Ground (WtG)* coupling schemes; (ii) *Coupling Scheme Type 2: Wire-to-Wire (WtW)* coupling schemes, and (iii) *Coupling Scheme Type 3*: MultiWire-to-MultiWire (MtM) coupling schemes. Depending on the applied coupling scheme, $\mathbf{C}^{\mathrm{in}}$ and $\mathbf{C}^{\mathrm{out}}$ are properly defined, as dictated in [48], [49], and, then, the coupling scheme channel transfer function $H^{\mathrm{C}}\{\cdot\}$ is straightforward computed from eq. (1).

3.2 HS-DET Method

With reference to eq.(1), [20] and [21], to apply HS-DET method when no measurement differences are assumed and the original ad-hoc OV LV BPL topologies are considered, the original measured coupling scheme transfer function $\overline{H_{\mathrm{or}}^{\mathrm{C}}}\{\cdot\}$, which is measured by the Information Technology department, for given coupling scheme can be determined by

$$\overline{H_{\mathrm{or}}^{\mathrm{C}}}(f_i) = H_{\mathrm{or}}^{\mathrm{C}}(f_i) + e(f_i),\ i=1,\ldots,u \quad (2)$$

$$e(f_i) = 0,\ i=1,\ldots,u \quad (3)$$

where f_i, $i=1,\ldots,u$ denotes the measurement frequency, u is the number of subchannels in the examined frequency range and $e(f_i)$ synopsizes the total measurement difference in dB at frequency f_i. that is anyway equal to zero in this paper.

As already mentioned, each hook can be treated as an open circuit fully interconnected horizontal branch by the hybrid model while the hook insertion modifies the original ad-hoc OV LV BPL topology to the respective modified one. With reference to eqs. (2) and (3), $\overline{H_{\mathrm{mod}}^{\mathrm{C}}}\{\cdot\}$ can be considered as the modified measured coupling scheme channel transfer function, which is measured by the Information Technology department, that anyway coincides with the modified theoretical coupling scheme channel transfer function $H_{\mathrm{mod}}^{\mathrm{C}}\{\cdot\}$ due to the no measurement difference assumption of this paper.

Apart from the channel attenuation measurements of the Information Technology department, its main concern is the computation of PES submetrics that are the cornerstone metrics of HS-DET method and define whether a hook style energy theft occurs or not. In accordance with [20], the PES submetrics that are used in this paper when the no measurement difference assumption occurs are:

$$PES_{\mathrm{or}} = 100\% \cdot \frac{\sum_{i=1}^{u} |H_{\mathrm{or}}^{\mathrm{C}}(f_i) - H_{\mathrm{or}}^{\mathrm{C}}(f_i)|}{\sum_{i=1}^{u} |H_{\mathrm{or}}^{\mathrm{C}}(f_i)|} = 0\% \quad (4)$$

$$PES_{\mathrm{mod}} = 100\% \cdot \frac{\sum_{i=1}^{u} |H_{\mathrm{mod}}^{\mathrm{C}}(f_i) - H_{\mathrm{or}}^{\mathrm{C}}(f_i)|}{\sum_{i=1}^{u} |H_{\mathrm{or}}^{\mathrm{C}}(f_i)|} \quad (5)$$

$$\Delta PES = PES_{\mathrm{mod}} - PES_{\mathrm{or}} = PES_{\mathrm{mod}} \quad (6)$$

where $PES_{\mathbf{or}}$ and $PES_{\mathbf{mod}}$ assess the accuracy of the original measured coupling scheme channel transfer function and modified measured coupling scheme channel transfer functions, respectively, in relation with the original theoretical coupling scheme channel transfer function while ΔPES is the difference between the original and modified measured coupling scheme channel transfer functions. Based on ΔPES computations of eq. (6), appropriate contour plots may be plotted that facilitate the hook style energy theft detection [20]-[22]. In accordance with [21], suitable $\overline{\Delta PES}$ thresholds have been proposed towards the safe hook style energy theft detection; HS-DET method can detect the energy theft through its strict $\overline{\Delta PES}$ threshold of 10% in the vast majority of the OV LV BPL topologies while the loose $\overline{\Delta PES}$ threshold of HS-DET method of 0% allows the energy theft in the remaining OV LV BPL topologies (*e.g.*, urban OV LV BPL topologies when very high measurement differences occur) with the risk of a false alarm. In this paper, the same conclusions regarding the $\overline{\Delta PES}$ thresholds of [21] are applied for the ΔPES computations.

A number of different scenarios concerning the operation of the HS-DET method has been examined until now while two critical but special issues concerning the operation of the ad-hoc OV LV BPL topologies are here outlined and investigated. Until now, the impact of OV LV BPL topologies, hook characteristics and measurement differences on the performance of HS-DET method has been assessed in [20] through $\overline{\Delta PES}$ metric and its relevant contour plots. In [21], apart from the decision $\overline{\Delta PES}$ threshold regarding the energy theft detection, the impact of the installation of very long hooks and the use of "smart" hooks has been examined. In [22], the impact of different CUD measurement differences, the installation of two "smart" hooks and the full interconnection assumption has also been assessed. Taking into consideration the findings of [20]-[22], two issues related to the operation of ad-hoc OV LV BPL topologies are investigated in this paper, namely:

- *The effect of the deviation from the initial measurement positions*. As already mentioned, in order to detect a hook style energy theft, Information Technology department should have already installed the original ad-hoc OV LV BPL topology and should have gathered reference measurements for the topologies of interest (*e.g.*, the indicative ad-hoc OV LV BPL topologies of Table 1) during the normal operation of the OV LV power grid. Therefore, the transmitting and receiving ends, which define the initial measurement positions, are well defined while the length *D* between the ends is known (*e.g.*, the typical length of the indicative ad-hoc OV LV BPL topologies of Table 1 is equal to 1000m). With reference to eq. (6), when an energy theft is suspected, Information Technology department should again install the ad-hoc OV LV BPL topology at the same measurement positions with the original ones. But, small measurement location deviations dev_{t} and dev_{r} may occur at the transmitting and receiving end, respectively, due to either position miscalculations of the Information Technology department or physical reasons having to do with the OV LV power grid. In Table 2, the respective modified ad-hoc OV LV BPL topologies of ones of Table 1 without the hook insertion are reported when the measurement location deviations dev_{t} and dev_{r} may take positive or negative values (the meaning of a positive or negative measurement location deviation is explained in Sec. 4.1). Two scenarios concerning the measurement location deviations dev_{t} and dev_{r} can occur and are examined in this paper:

- *Scenario A:* In this first scenario, the length *D* of the modified ad-hoc OV LV BPL topology without the hook remains the same with the original one. Since the length between the two aforementioned BPL topologies remains the same, the measurement location deviations dev_t and dev_r are related according to:

$$dev_r = -dev_t \quad (7)$$

Table 2
Modified Ad-Hoc OV LV BPL Topologies without Hook Style Energy Theft with Respect to the Measurement Location Deviation

Topology Name (OV LV BPL Topology Class)	**Topology Description**	**Number of Branches**	**Length of Distribution Lines**	**Length of Branching Lines**
Urban case A	Shifted typical OV LV urban topology without hook	3	L_1=500m+dev_t, L_2=200m, L_3=100m, L_4=200m+dev_r	L_{b1}=8m, L_{b2}=13m, L_{b3}=10m
Urban case B	Shifted aggravated OV LV urban topology without hook	5	L_1=200m+dev_t, L_2=50m, L_3=100m, L_4=200m, L_5=300m, L_6=150m+dev_r	L_{b1}=12m, L_{b2}=5m, L_{b3}=28m, L_{b4}=41m, L_{b5}=17m
Suburban case	Shifted OV LV suburban topology without hook	2	L_1=500m+dev_t, L_2=400m, L_3=100m+dev_r	L_{b1}=50m, L_{b2}=10m
Rural case	Shifted OV LV rural topology without hook	1	L_1=600m+dev_t, L_2=400m+dev_r	L_{b1}=300m
"LOS" case	Shifted OV LV Line-of-Sight transmission without hook	0	L_1=1000m+dev_t+dev_r	-

- *Scenario B:* In this second scenario, the length *D* of the modified ad-hoc OV LV BPL topology without the hook is different from the original one. In this general case, the measurement location deviations dev_t and dev_r are not related each other and can be independently modified.

With reference to Table 1, 2 and Fig. 1(b), the modified ad-hoc OV LV BPL topology after the hook insertion occurs when a hook style energy theft occurs at the position A_h that is located at distance D_h from the transmitting end of the original ad-hoc OV LV BPL topology. The performance of HS-DET method should be assessed for both scenarios after the hook insertion.

- *The effect of longer ad-hoc OV LV BPL topologies than the typical ones*. With reference to Table 1 and 2, the indicative ad-hoc OV LV BPL topologies are assumed to have the typical lengths of 1000m, which are the same with the lengths of the cascaded OV LV BPL topologies of permanent BPL networks. In accordance with [11]-[14], [17]-[21], [23]-[28], although this is the typical topology length during the installation of complete BPL networks, longer ad-hoc OV LV BPL topologies can be deployed since across a length of 1000 m a hook style energy theft can be easily detected through a simple optical

inspection. For that reason, concatenations of the same indicative ad-hoc OV LV BPL topologies of Table 1 are assumed for the study of the effect of longer ad-hoc OV LV BPL topologies in urban, suburban and rural environments. In Table 3, the respective modified ad-hoc OV LV BPL topologies of ones of Table 1 without the hook insertion are reported

Table 3
Modified Ad-Hoc OV LV BPL Topologies without Hook Style Energy Theft with Respect to the Concatenation of Original Ad-Hoc OV LV BPL Topologies

Topology Name (OV LV BPL Topology Class)	**Topology Description**	**Number of Branches**	**Length of Distribution Lines**	**Length of Branching Lines**
Urban case A	Concatenated Typical OV urban topology without hook	3	$L_{v,1}$=500m, $L_{v,2}$=200m, $L_{v,3}$=100m, $L_{v,4}$=200m	$L_{v,b1}$=8m, $L_{v,b2}$=13m, $L_{v,b3}$=10m
Urban case B	Concatenated aggravated OV urban topology without hook	5	$L_{v,1}$=200m, $L_{v,2}$=50m, $L_{v,3}$=100m, $L_{v,4}$=200m, $L_{v,5}$=300m, $L_{v,6}$=150m	$L_{v,b1}$=12m, $L_{v,b2}$=5m, $L_{v,b3}$=28m, $L_{v,b4}$=41m, $L_{v,b5}$=17m
Suburban case	Concatenated OV LV suburban topology without hook	2	$L_{v,1}$=500m, $L_{v,2}$=400m, $L_{v,3}$=100m	$L_{v,b1}$=50m, $L_{v,b2}$=10m
Rural case	Concatenated OV LV rural topology without hook	1	$L_{v,1}$=600m, $L_{v,2}$=400m	$L_{v,b1}$=300m
"LOS" case	Concatenated OV LV Line-of-Sight transmission without hook	0	$L_{v,1}$=1000m	-

when the number of concatenations v may take integer values above 1. Since the length of the indicative ad-hoc OV LV BPL topologies of Table 1 is equal to 1000 m, the length of the modified ad-hoc OV LV BPL topologies of Table 3 becomes equal to v×1000 m.

4. Numerical Results and Discussion

The numerical results of this Section focus on evaluating the performance of HS-DET method after the installation of ad-hoc OV LV BPL topologies. Exploiting the already acquired knowledge of [20]-[22], the impact of the deviation from the initial measurement positions and of longer ad-hoc OV LV BPL topologies than the typical ones on the HS-DET method performance is assessed through the prism of ΔPES and its appropriate contour plots. The goal of HS-DET method is to detect the hook style energy theft when the aforementioned two special issues of the operation of the

ad-hoc OV LV BPL topologies occur. For that reason, a HS-DET method roadmap and ΔPES thresholds of [20]-[22] are going to be exploited. As the circuital, topological and coupling scheme characteristics of OV LV BPL networks are concerned, these remain the same with [20]-[22].

4.1 HS-DET Method and the Deviation from the Initial Measurement Positions

With reference to eqs. (4)-(6), when the Information Technology department can exactly install its ad-hoc OV LV BPL topology at the initial measurement positions and no hook style energy theft occurs, ΔPES values between the original ad-hoc OV LV BPL topology and the respective modified ad-hoc OV LV BPL topology without the hook are going to be equal to zero, which is anyway the obvious result. However, small measurement location deviations (*e.g.*, from few cm to approximately 10 m) from the initial measurement positions may occur having as a result a ΔPES difference between the original ad-hoc OV LV BPL topology and the respective modified ad-hoc OV LV BPL topology without hook except for the "LOS" transmission case. In accordance with Sec. 3.2, there are two scenarios that should be examined.

4.1.1 Scenario A

With reference to Tables 1 and 2, let assume that a measurement location deviation dev_t occurs between the original ad-hoc OV LV BPL topologies and the respective shifted ad-hoc OV LV BPL topologies without hook that may range from -10 m to 10 m. Since Information Technology department can accurately measure the distance between the transmitting and receiving end and can assure that this distance remains equal to D, the measurement location deviation dev_r is given by eq. (7). In Fig. 2, ΔPES is plotted with respect to the measurement location deviation dev_t between the typical OV LV urban topology and the shifted typical OV LV urban topology without hook. In the same figure, same ΔPES curves with the urban case A but for the urban case B, suburban case, rural case and "LOS" transmission case are given.

From Fig. 2, it is evident that extremely low ΔPES values are observed regardless of the applied magnitude of measurement location deviations. Practically, a positive measurement location deviation can be treated as a MTL distribution cable segment that is cascaded to the examined original ad-hoc OV LV BPL topology. At the same time, the equal in absolute value but negative measurement location deviation, which is expressed in eq. (7), can be treated as a MTL distribution cable segment that is removed from the examined original ad-hoc OV LV BPL topology. In total, since the distance between the transmitting and receiving end of Scenario A always remains equal to D, the symmetry property of BPL channels, which has been detailed in [50], [51], holds regardless of the examined ad-hoc OV LV BPL topology. Therefore, small measurement location deviations in Scenario A cannot trigger a false hook style energy theft alarm since ΔPES values remain significantly lower than the strict 10% ΔPES threshold.

Actually, it is expected that the small measurement location deviations of Scenario A cannot abrupt the high performance of HS-DET method in detecting the hook style energy theft. In order to validate the detection efficiency of HS-DET method when a hook style energy theft occurs, $\Delta(\Delta PES)$ is going to be computed and presented hereafter; $\Delta(\Delta PES)$ expresses the difference between the ΔPES when a measurement location deviation occurs and the ΔPES without the measurement location deviation –see Figs. 3(a)-(e) of [20]– for given ad-hoc OV LV BPL topology, hook distance from

the transmitting end span and hook length span. In Fig. 3(a), $\Delta(\Delta PES)$ is plotted versus the hook distance from the transmitting end and the hook length when the indicative ad-hoc OV LV BPL topology of urban case A is assumed, measurement location deviation dev_t is equal to -10 m and Scenario A is examined. In Figs. 3(b), 3(c), 3(d) and 3(e), same plots with Fig. 3(a) are given but for the case of the urban case B, suburban case, rural case and "LOS" case, respectively. In Figs. 4(a)-(e), same plots with the respective Figs. 3(a)-(e) but for the case of the measurement location deviation dev_t that is equal to 10 m. Here, it should be noted that the hook distance span and

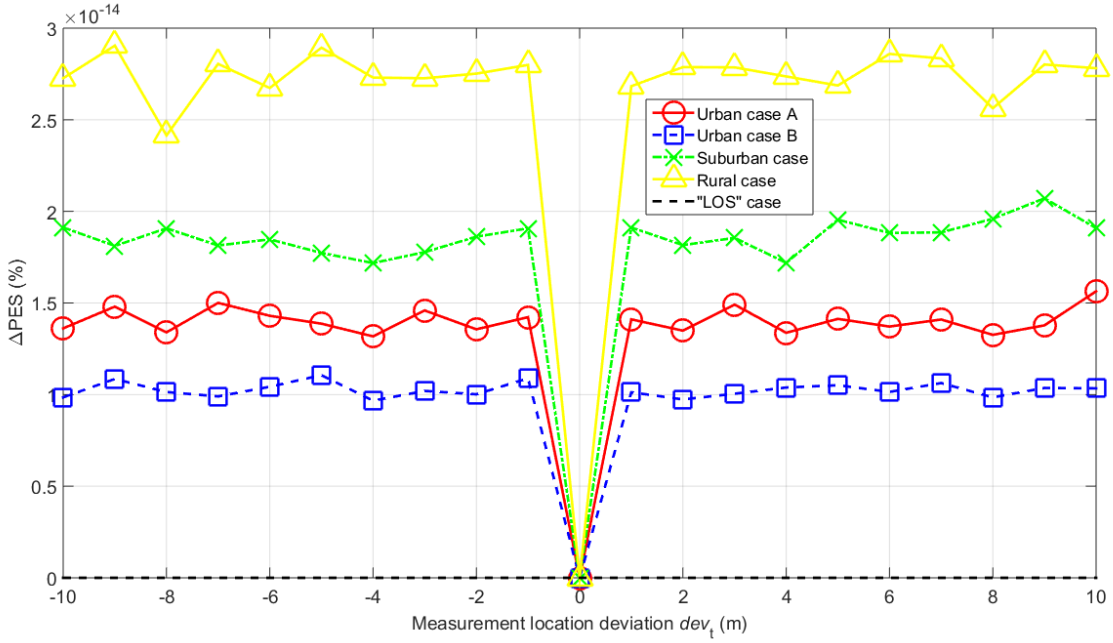

Fig. 2. ΔPES of HS-DET method for the five indicative ad-hoc OV LV BPL topologies for various measurement location deviations dev_t when no hook style energy theft occurs (Scenario A).

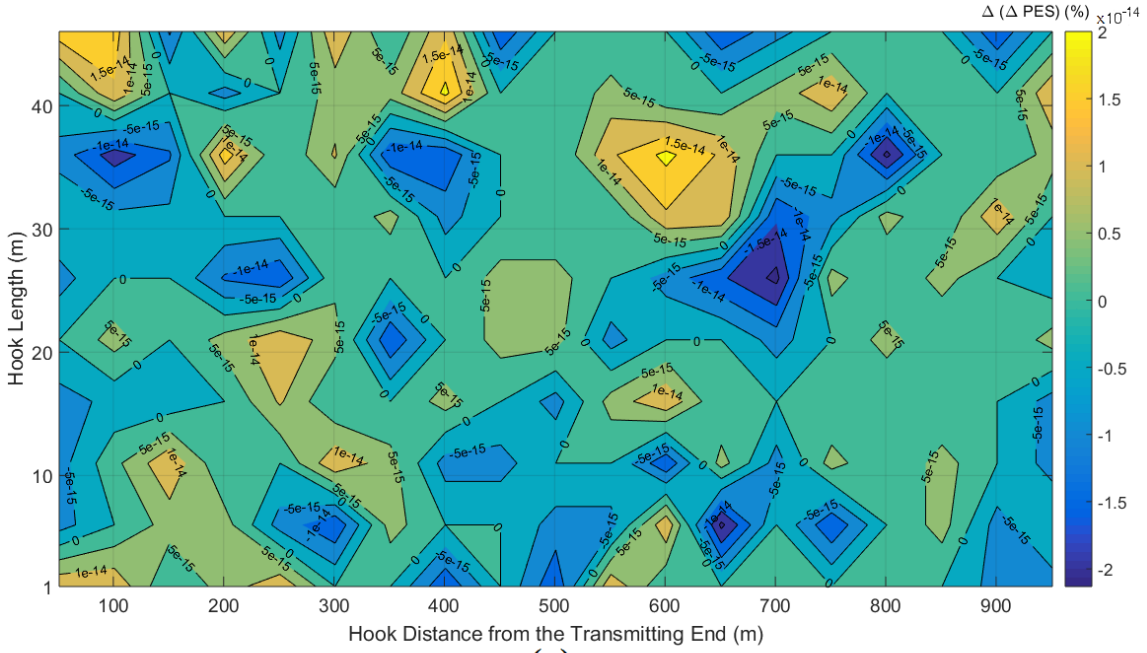
Δ (Δ PES) (%)
x10^-14
Hook Length (m)
Hook Distance from the Transmitting End (m)

(a)

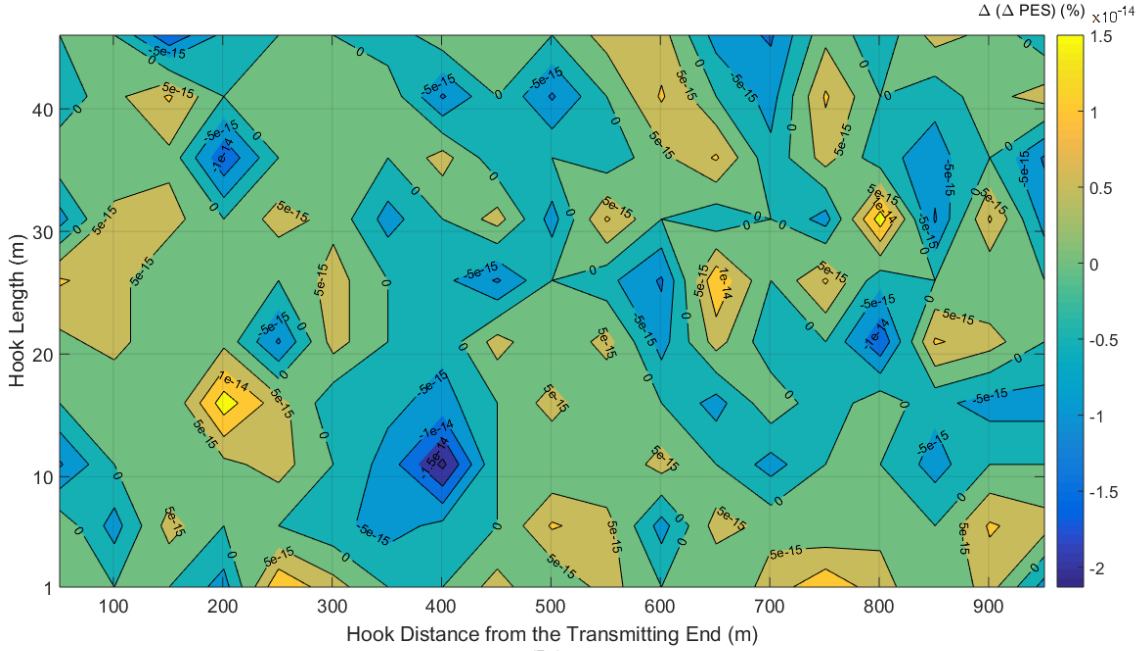
Δ (Δ PES) (%)
x10^-14
Hook Length (m)
Hook Distance from the Transmitting End (m)

(b)

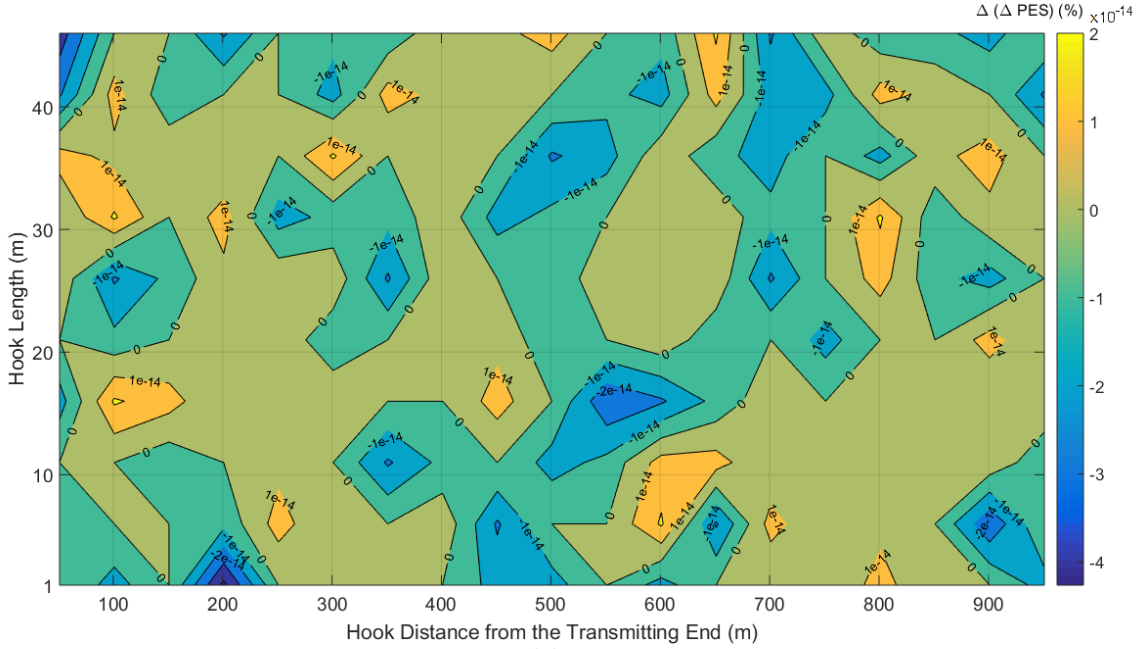
Δ (Δ PES) (%)
x10^-14
Hook Length (m)
Hook Distance from the Transmitting End (m)

(c)

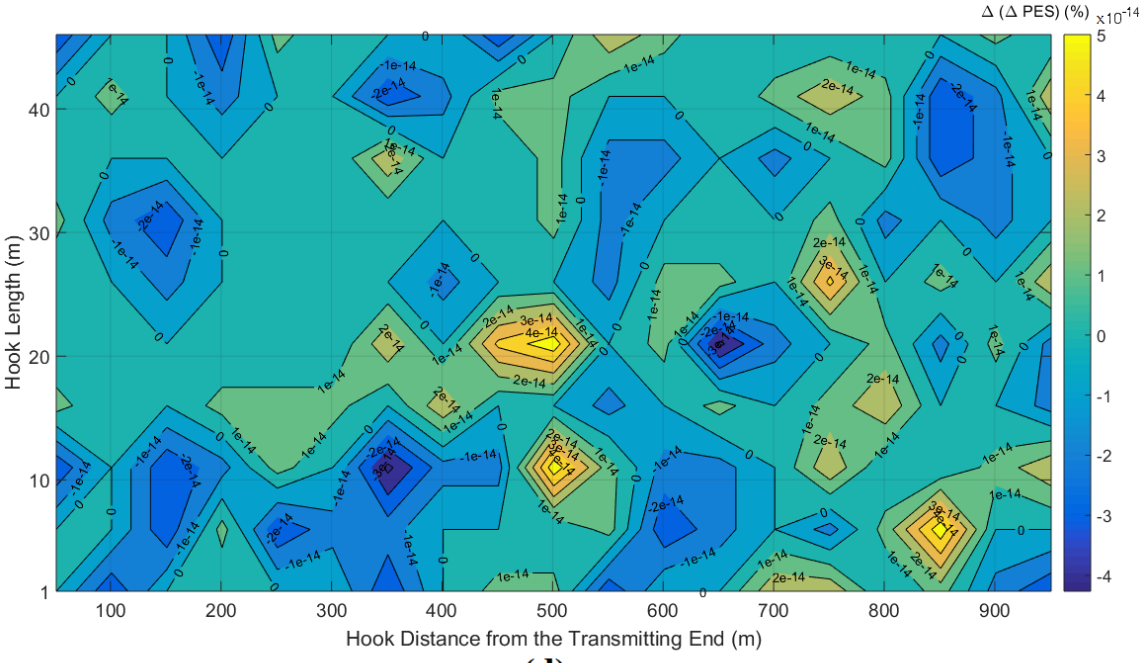
Δ (Δ PES) (%)
x10^-14
Hook Length (m)
Hook Distance from the Transmitting End (m)

(d)

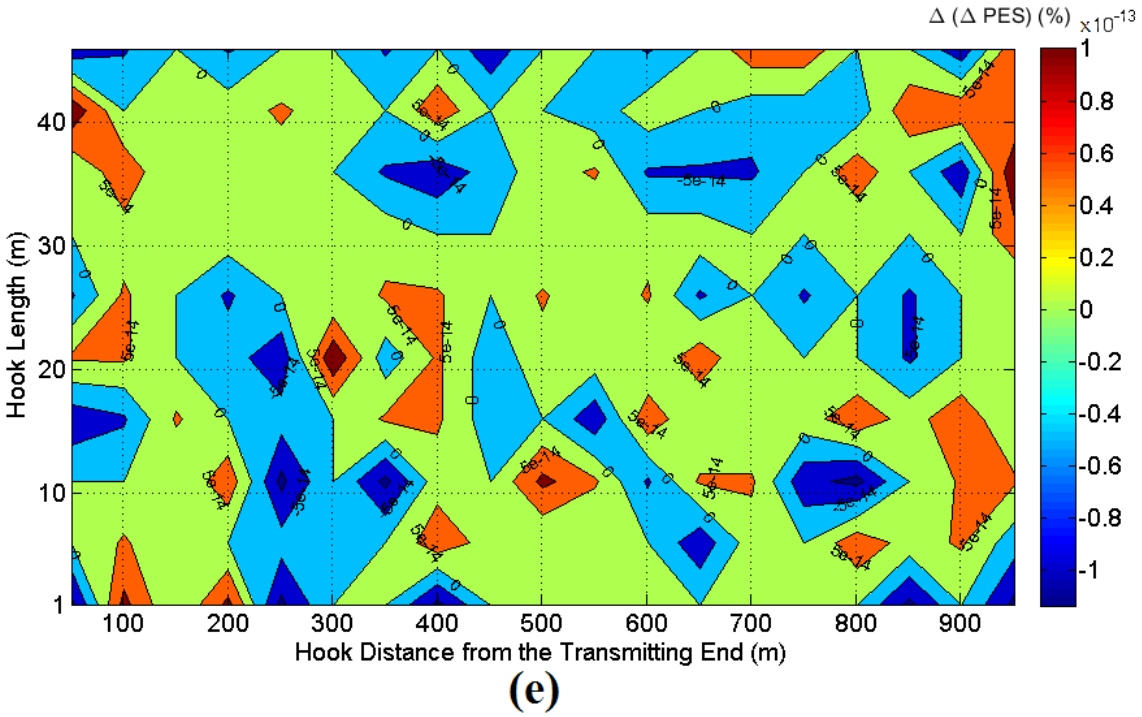

Fig. 3. $\Delta(\Delta PES)$ of the indicative OV LV BPL topologies for various hook distances from the original transmitting end and hook lengths when measurement location deviation dev_t is equal to -10 m (Scenario A). (a) Urban case A. (b) Urban case B. (c) Suburban case. (d) Rural case. (e) "LOS" case.

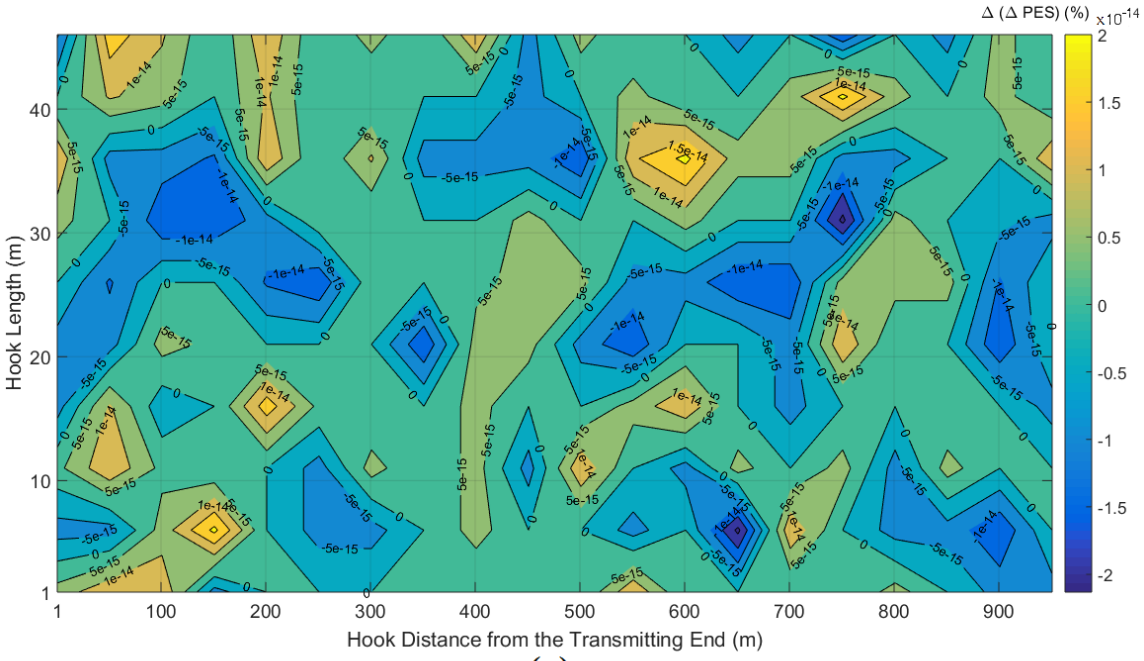
Δ (Δ PES) (%)
x10^-14
Hook Length (m)
Hook Distance from the Transmitting End (m)

(a)

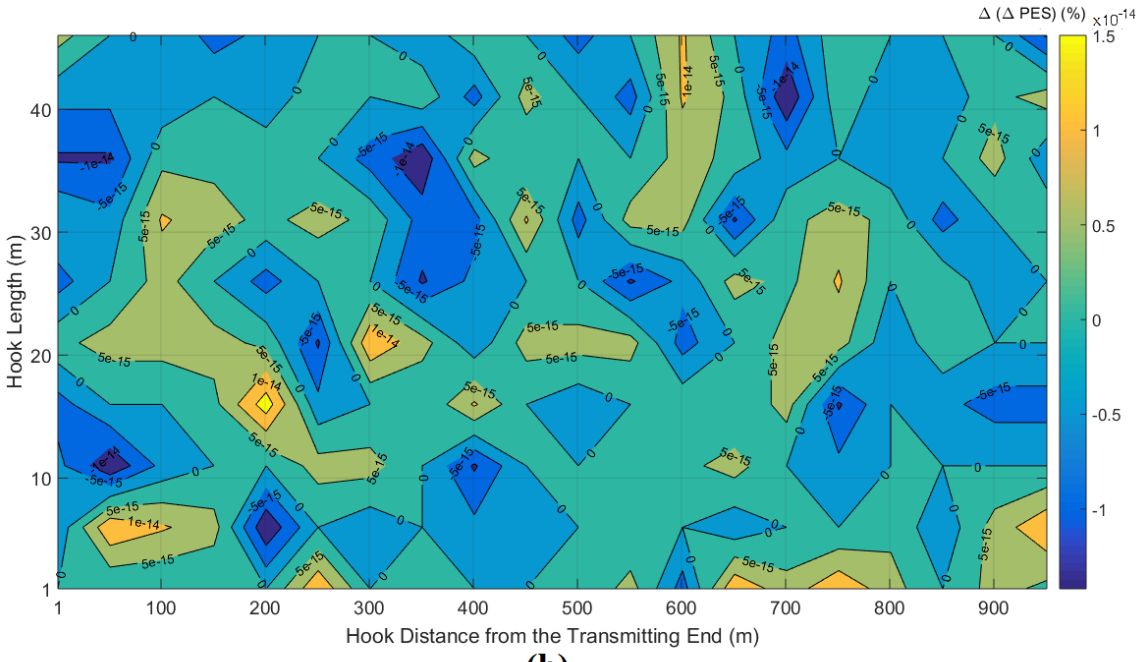
Δ (Δ PES) (%)
x10^-14
Hook Length (m)
Hook Distance from the Transmitting End (m)

(b)

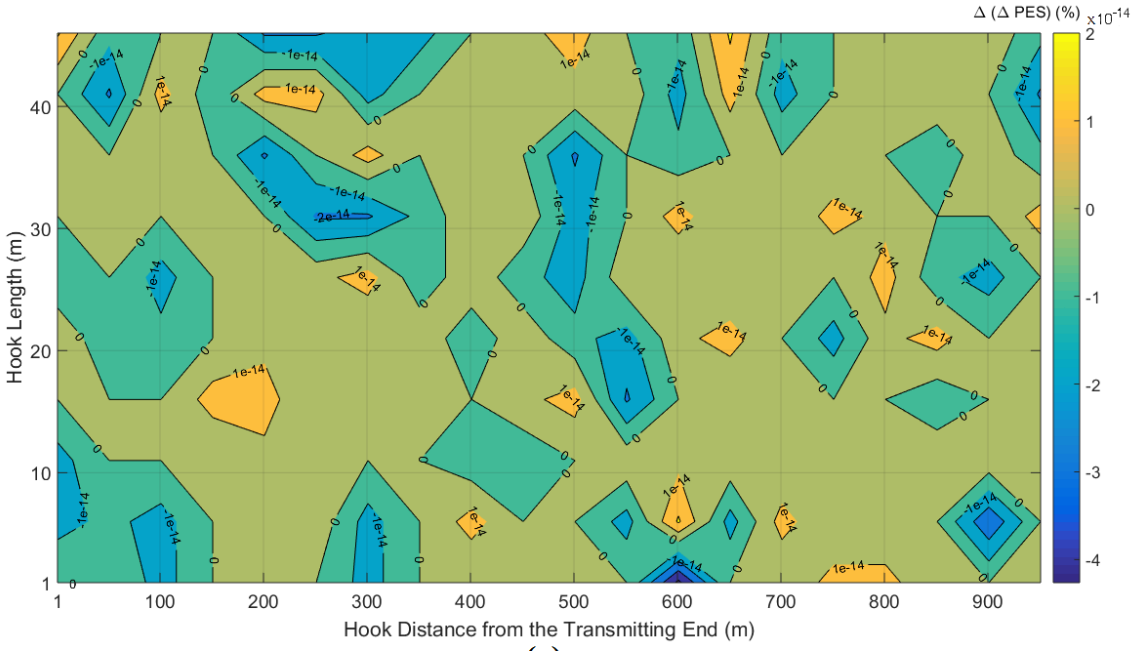
Δ (Δ PES) (%)
x10^-14
Hook Length (m)
Hook Distance from the Transmitting End (m)

(c)

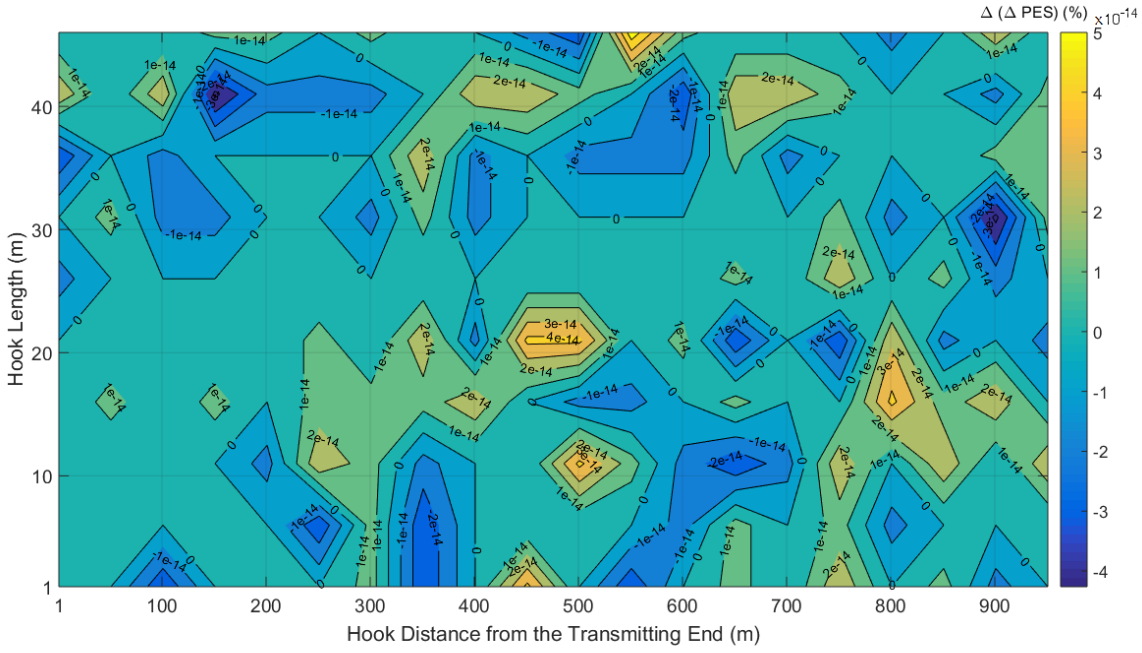
Δ (Δ PES) (%)
x10^-14
Hook Length (m)
Hook Distance from the Transmitting End (m)

(d)

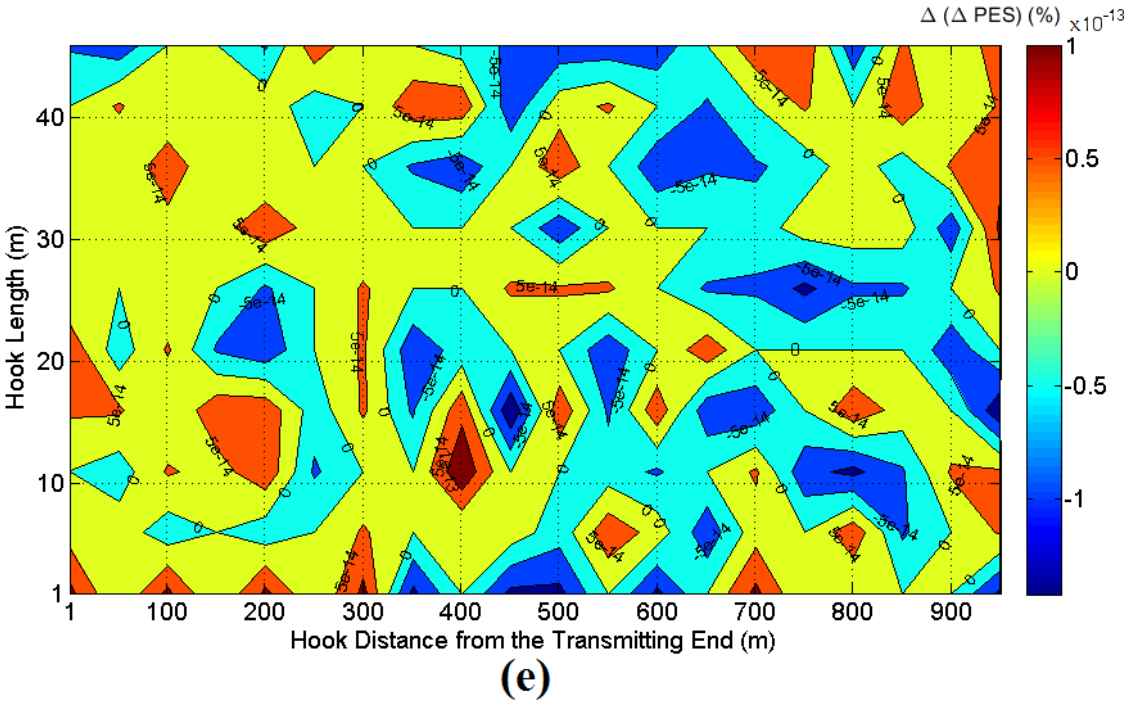

Fig. 4. Same curves with Fig. 3 but for measurement location deviation dev_t of 10 m.

the hook length span are assumed to be equal to 50 m and 5 m, respectively, while the range of the hook distance from the transmitting end of the examined original ad-hoc OV LV BPL topology and the range of the hook length are from 1 m to 951 m and from 1 m to 46 m, respectively, for all the examined contour plots of this paper. The selection of the previous plot specifications has been done for the sake of the direct PES submetric comparison against Figs. 3(a)-(e) of [20].

By comparing Figs. 3(a)-(e) and 4(a)-(e) with Figs. 3(a)-(e) of [20], several interesting comparative observations can be made regarding the performance of HS-DET method when Scenario A is adopted, namely:

- Regardless of the measurement location deviation dev_t and its dependent measurement location deviation dev_r, $\Delta(\Delta PES)$ remains extremely low in all the examined cases of Scenario A, in the order of 10^{-14}%. This indicates that the small values of ΔPES, which have already been spotted in Fig. 2, are further reflected on respective small $\Delta(\Delta PES)$ values of Figs. 3(a)-(e) and 4(a)-(e) thus unveiling the invulnerability of HS-DET method when various measurement location deviations that are in agreement with Scenario A occur.
- Since ΔPES of Figs. 3(a)-(e) of [20] remains well above the 10% threshold of the easy hook style energy theft detection and all the observed $\Delta(\Delta PES)$ values of Figs. 3(a)-(e) and 4(a)-(e) remain in the order of 10^{-14}%, ΔPES values of the modified ad-hoc OV LV BPL topologies after the hook insertion will remain significantly greater than the strict ΔPES threshold of 10% thus allowing the easy hook style energy theft detection regardless of the magnitude of the measurement location deviations.
- From Figs. 3(a)-(e) and 4(a)-(e), $\Delta(\Delta PES)$ values remain in the order of 10^{-14}% regardless of the examined ad-hoc OV LV BPL topology. Similarly to [20],

the hook detection becomes easier in the cases of ad-hoc OV LV BPL topologies of low number of long branches such as "LOS" and rural topologies. In the latter cases, a hook insertion provokes the birth of a multipath environment which is accompanied by deep and frequent spectral notches to the measured coupling scheme channel attenuation and, of course, significant increase of PES_{mod} and ΔPES. Indeed, the easy hook detection is validated by the high ΔPES values across the contour plots of the "LOS" and rural OV LV BPL topologies of [20].

- From Figs. 3(a)-(e) and 4(a)-(e), $\Delta(\Delta PES)$ values remain in the order of 10^{-14}% regardless of the hook length. Similarly to [20], the detection of the hook style energy theft of Scenario A in ad-hoc OV LV BPL topologies remains easier when the hook remains short enough (*i.e.*, shorter than 10 m) while the detection becomes less easy but safe when the hook exceeds 10 m.
- From Figs. 3(a)-(e) and 4(a)-(e), $\Delta(\Delta PES)$ values remain in the order of 10^{-14}% regardless of the hook position during the Scenario A. Similarly to [20], the hook distance from the transmitting end becomes more crucial in ad-hoc OV LV BPL topologies with high number of branches rather than in the ad-hoc OV LV BPL rural and "LOS" topologies.

From the previous observations, it is highlighted the main advantage of Scenario A that is the fixed distance between the transmitting and receiving end. This implies that even if large measurement location deviations dev_t may occur, these deviations can be counterbalanced by the equal in magnitude but opposite measurement location deviations dev_r. Hence, the most important issue during the installation of an ad-hoc OV LV BPL topology for the hook style energy theft detection by the Information Technology department is the maintenance of the same distance between the transmitting and receiving end rather than the exact installation position of the transmitting end since measurement location deviations dev_t and dev_r can be counterbalanced.

4.1.2 Scenario B

With reference to Tables 1 and 2, let assume that a measurement location deviation dev_t occurs between the original ad-hoc OV LV BPL topologies and the respective shifted ad-hoc OV LV BPL topologies without hook that may range from -10 m to 10 m. In Scenario B, it is assumed that Information Technology department cannot assure that the distance between the transmitting and receiving end is equal to *D*. Since the length of the shifted ad-hoc OV LV BPL topology is not exactly known, the measurement location deviation dev_r may also range from -10 m to 10 m independently of the measurement location deviation dev_t.

With reference to Sec. 4.1.1, it has been verified that the main issue regarding the performance of HS-DET method is the algebraic sum of the measurement location deviations dev_t and dev_r rather than their exact values. Hence, the measurement location deviation dev_t can be considered to vary from -20 m to 20 m in the following analysis so that all the different combinations of the measurement location deviations dev_t and dev_r can equivalently be studied without creating additional complexity. In Fig. 5, ΔPES is plotted with respect to the measurement location deviation dev_t between the typical OV LV urban topology and the shifted typical OV LV urban topology without hook when Scenario B is applied. In the same figure, same ΔPES curves with the urban

case A but for the urban case B, suburban case, rural case and "LOS" transmission case are given.

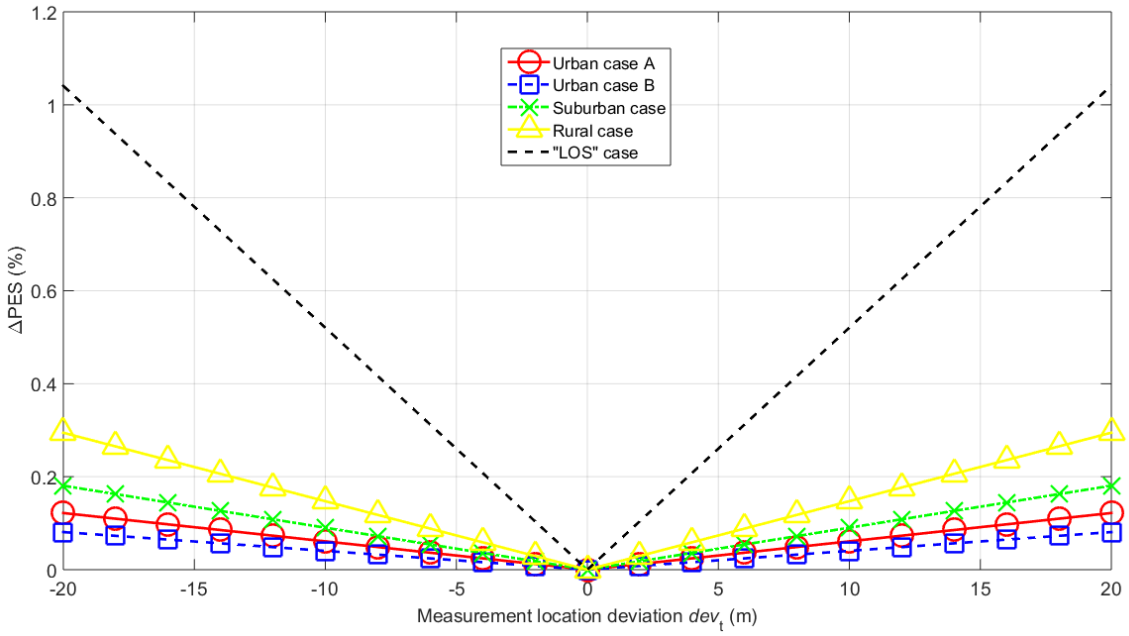

Fig. 5. ΔPES of HS-DET method for the five indicative ad-hoc OV LV BPL topologies for various measurement location deviations dev_t when no hook style energy theft occurs (Scenario B).

From Fig. 5, low ΔPES values that depend on the applied magnitude of measurement location deviation dev_t are observed in Scenario B. By comparing Figs. 2 and 5, ΔPES values of Scenario B are significantly higher than the ones of Scenario A but anyway remain significantly lower than the strict 10% ΔPES threshold. This is a logical result since insertion or removal of MTL cable segments are considered for the ad-hoc OV LV BPL topologies when positive or negative measurement location deviations dev_t are examined. Note that the symmetry property of BPL channels, which holds in Scenario A, does not stand in Scenario B except for the case where measurement location deviation dev_t is equal to 0. In the latter case, the study of Scenario B degenerates into the study of Scenario A.

In accordance with [23], [25], [27], [30], [48], the small ΔPES values of Fig. 5 are explained by the fact that multipath rather than "LOS" transmission distance is identified as the dominant factor in OV LV BPL channels thus mainly affecting BPL signal attenuation. Hence, the effect of insertion or removal of MTL cable segments at the ad-hoc OV LV BPL topologies is not so severe and is not recognized as the primary attenuation factor since multipath attenuation is the primary one. Therefore, among ΔPES values of different ad-hoc OV LV BPL topologies in Fig. 5, the most affected ones by the measurement location deviations of Scenario B are the "LOS" and rural OV LV BPL topologies since multipath attenuation remains negligible in these cases.

In addition, it should be noted that ΔPES values of ad-hoc OV LV BPL topologies remain negligible with respect to the strict 10% ΔPES threshold while they start to become important with respect to the loose 0% ΔPES threshold of [21], [22].

In fact, if the loose 0% ΔPES threshold, but risky in terms of a possible false alarm, is assumed only the "LOS" ad-hoc OV LV BPL topology can trigger this false alarm (*i.e.*, ΔPES values slightly greater than 1% when the absolute value of measurement location deviation dev_t is equal to 20 m) since the other ad-hoc OV LV BPL topologies are characterized by significantly low ΔPES values (*i.e.*, ΔPES values lower than 0.3%).

Similarly to Scenario A, it is expected that the small measurement location deviations of Scenario B cannot foment the high performance of HS-DET method against the hook style energy theft. In order to validate the detection efficiency of HS-DET method when a hook style energy theft occurs, $\Delta(\Delta PES)$ is going to be computed and presented for Scenario B; in Fig. 6(a), $\Delta(\Delta PES)$ is plotted versus the hook distance from the transmitting end and the hook length when the indicative ad-hoc OV LV BPL topology of urban case A is assumed, measurement location deviation dev_t is equal to -20 m and Scenario B is applied. In Figs. 6(b), 6(c), 6(d) and 6(e), same plots with Fig. 6(a) are given but for the case of the urban case B, suburban case, rural case and "LOS" case, respectively. In Figs. 7(a)-(e), same plots with the respective Figs. 6(a)-(e) but for the case of the measurement location deviation dev_t that is equal to 20 m are given. As the hook characteristics are concerned for the examined contour plots, these are the same with Figs. 3(a)-(e) and 4(a)-(e).

By comparing Figs. 6(a)-(e) and 7(a)-(e) with Figs. 3(a)-(e), 4(a)-(e) and 3(a)-(e) of [20], additional observations can be made regarding the performance of HS-DET method when Scenario B is examined, namely:

- Similarly to Figs. 3(a)-(e), the first value of the hook distance from the original transmitting end in Figs. 6(a)-(e) is equal to 51 m. Since a measurement location deviation dev_t of -10 m and -20 m is assumed in Figs. 3(a)-(e) and Figs. 6(a)-(e), respectively, this is equal to a respective MTL cable segment removal of 10 m and 20 m from the transmitting end of the original ad-hoc OV LV BPL topologies with reference to Table 2. Since the range of the hook distance from the transmitting end of the examined original ad-hoc OV LV BPL topology is equal to 1 m, the hook distance from the original transmitting end span is equal to 50 m and the first value of the range of the hook distance from the transmitting end cannot be used, the first value of the hook distance from the original transmitting end in Figs. 3(a)-(e) and 6(a)-(e) is equal to 51m.
- Negative $\Delta(\Delta PES)$ values are observed in Figs. 6(a)-(e) whereas positive $\Delta(\Delta PES)$ values are observed in Figs. 7(a)-(e). Conversely to Figs. 3(a)-(e) and 4(a)-(e) where a mixed scenario regarding the sign of $\Delta(\Delta PES)$ occurs, the negative $\Delta(\Delta PES)$ values but of small magnitudes that are observed in Figs. 6(a)-(e) indicate that HS-DET method slightly more difficult detects the hook style energy theft; the opposite occurs when the positive $\Delta(\Delta PES)$ values are demonstrated in Figs. 7(a)-(e). Hence, positive measurement location deviations that entail larger length between the transmitting and receiving end of the modified ad-hoc OV LV BPL topologies can facilitate the detection of hook style energy theft.
- In accordance with [20], the hook distance from the transmitting end influences the performance of HS-DET method only in the cases of ad-hoc OV LV BPL topologies with high number of branches thus creating areas of different hook style energy theft detection difficulty in contour plots. Hence, with reference to Figs. 3(a)-(e) of [20], higher ΔPES values characterize areas of easier hook style

energy theft detection. With reference to Figs. 6(a)-(e) and 7(a)-(e),

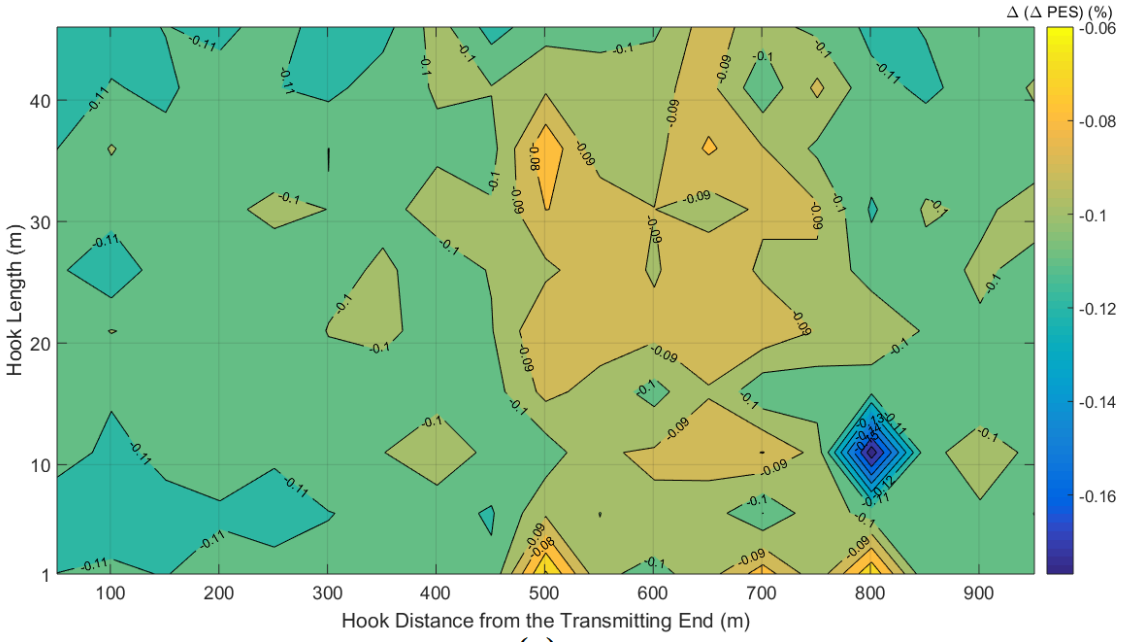

(a)

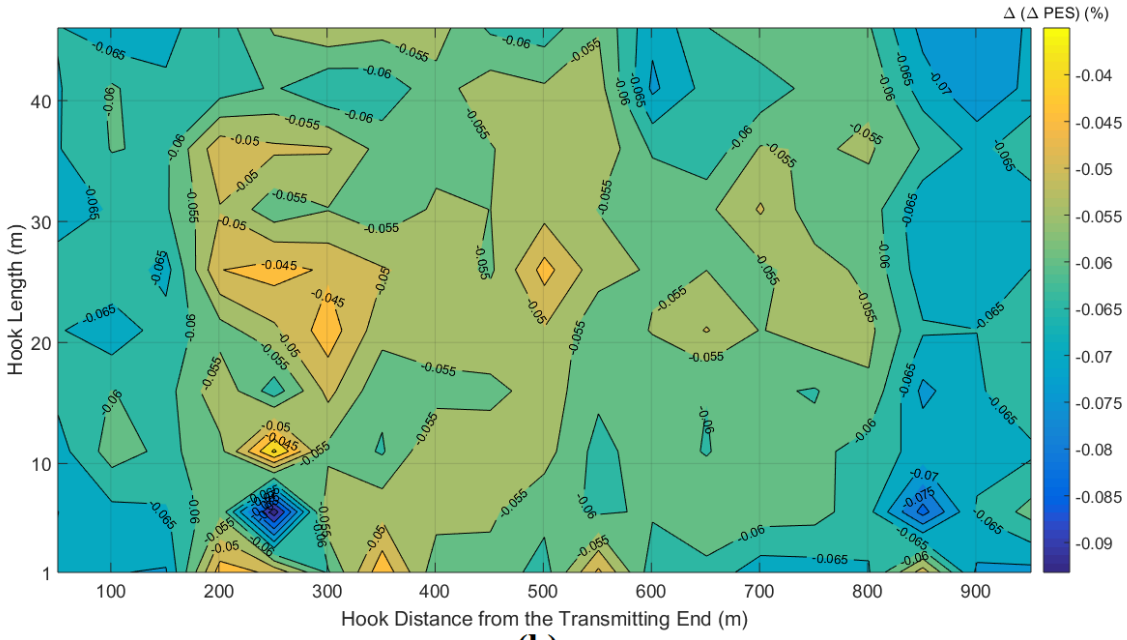

(b)

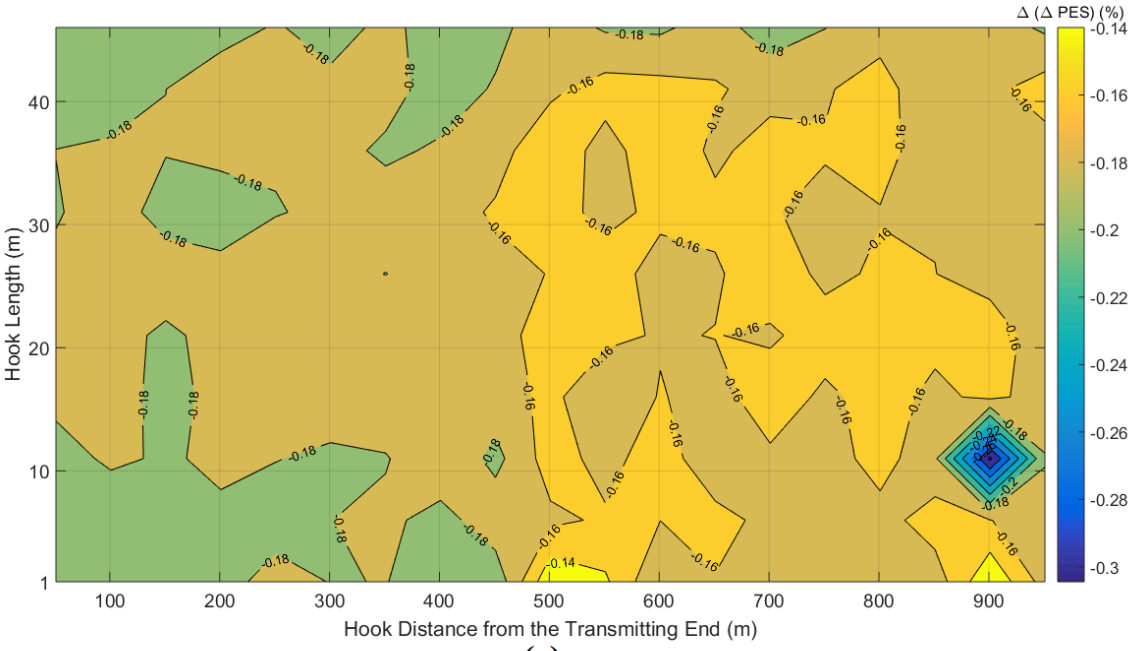
Δ (Δ PES) (%)
Hook Length (m)
Hook Distance from the Transmitting End (m)

(c)

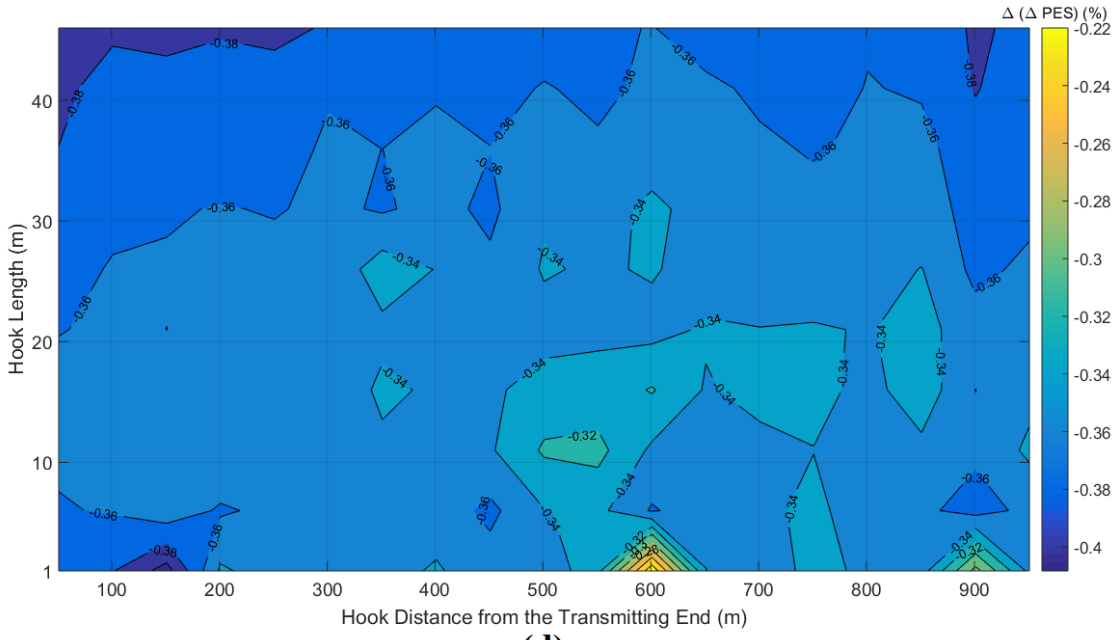
Δ (Δ PES) (%)
Hook Length (m)
Hook Distance from the Transmitting End (m)

(d)

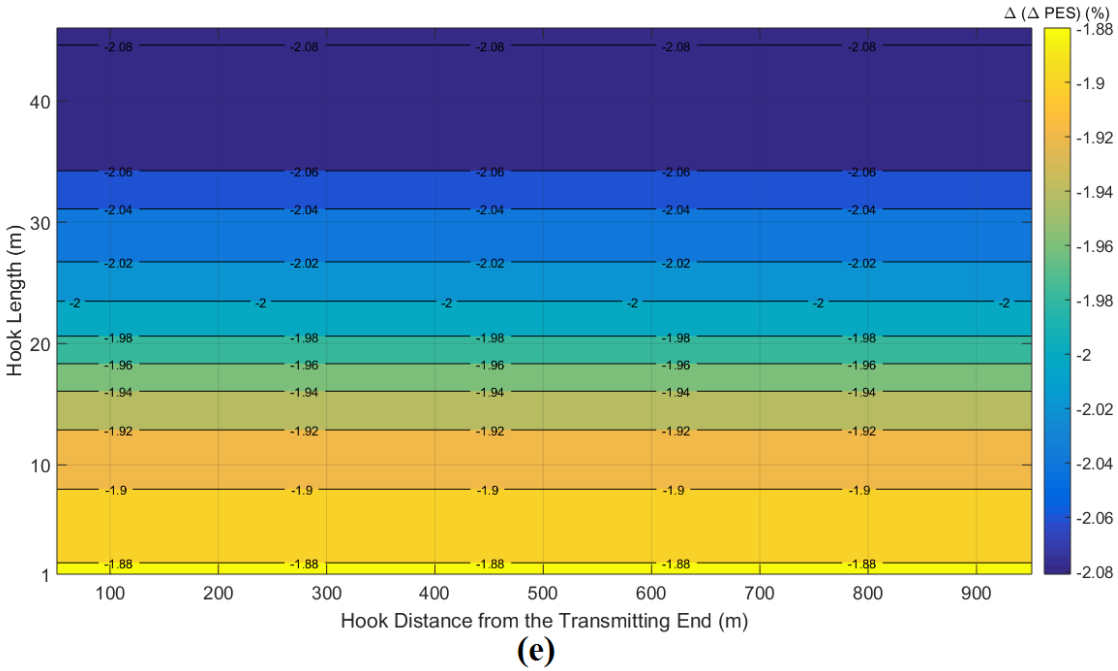

Fig. 6. $\Delta(\Delta PES)$ of the indicative OV LV BPL topologies for various hook distances from the original transmitting end and hook lengths when measurement location deviation dev_t is equal to -20 m (Scenario B). (a) Urban case A. (b) Urban case B. (c) Suburban case. (d) Rural case. (e) "LOS" case.

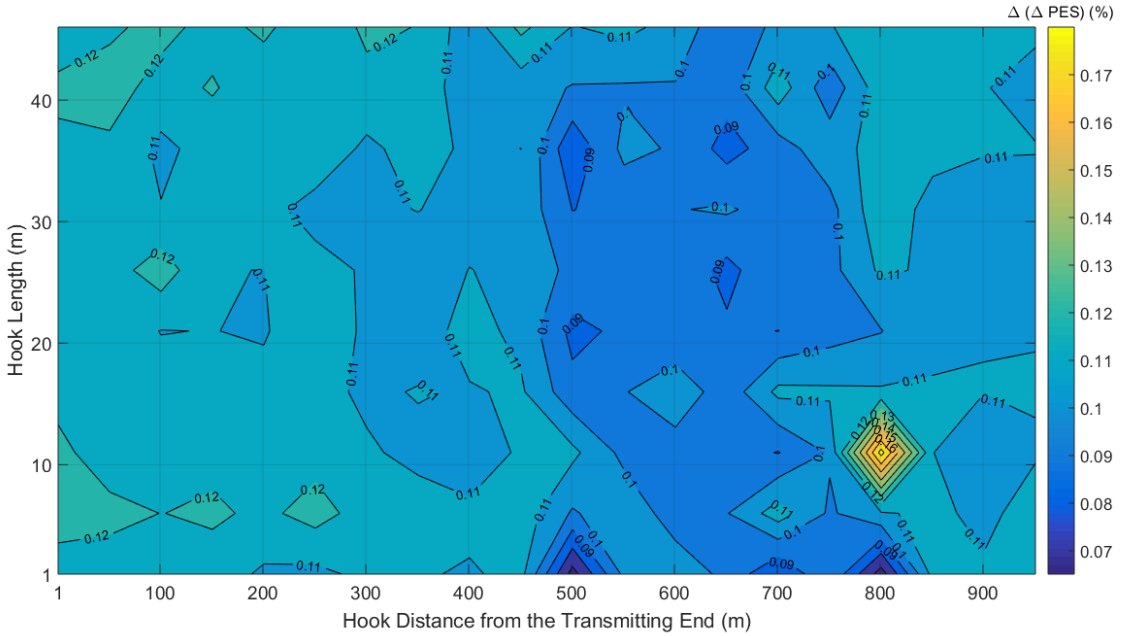
Δ (Δ PES) (%)
Hook Length (m)
Hook Distance from the Transmitting End (m)

(a)

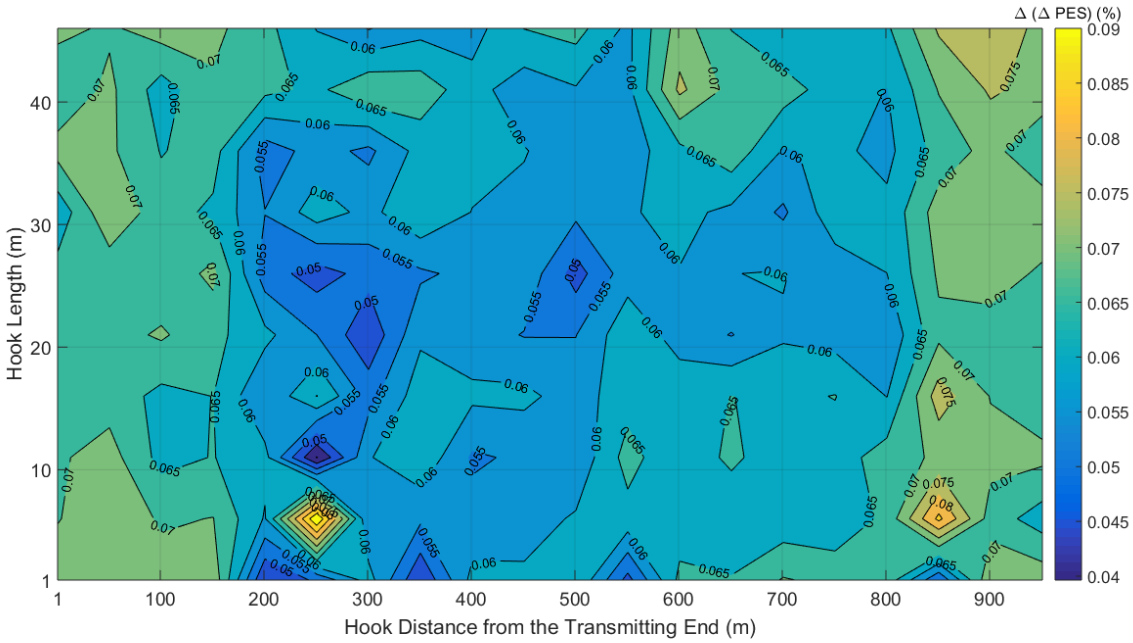
Δ (Δ PES) (%)
Hook Length (m)
Hook Distance from the Transmitting End (m)

(b)

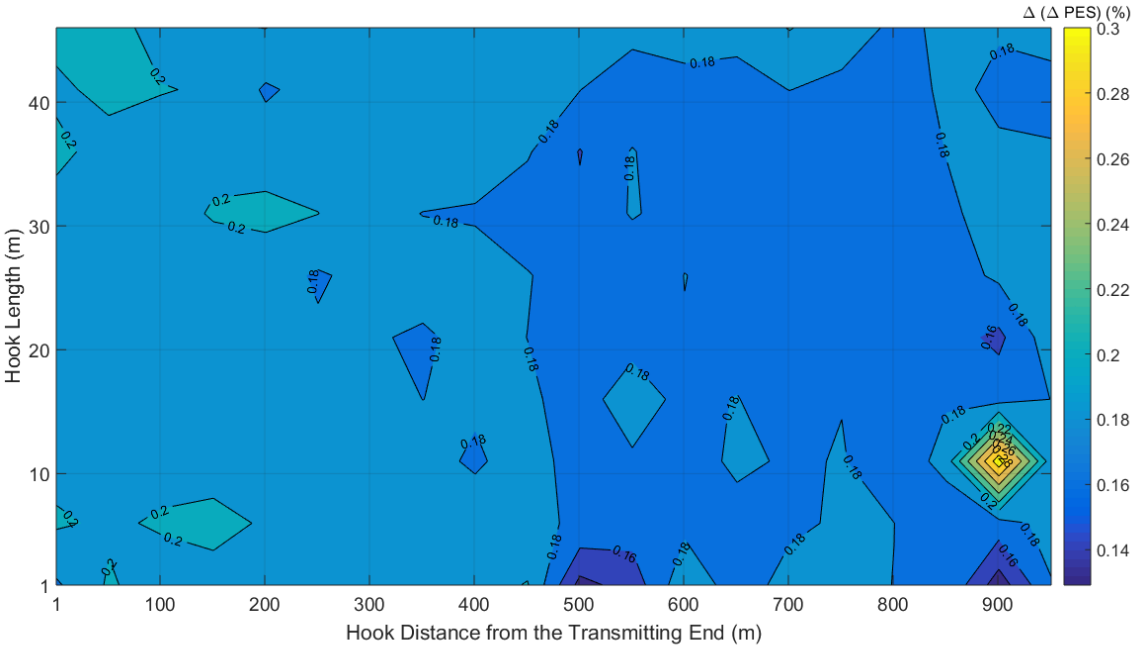
Δ (Δ PES) (%)
Hook Length (m)
Hook Distance from the Transmitting End (m)

(c)

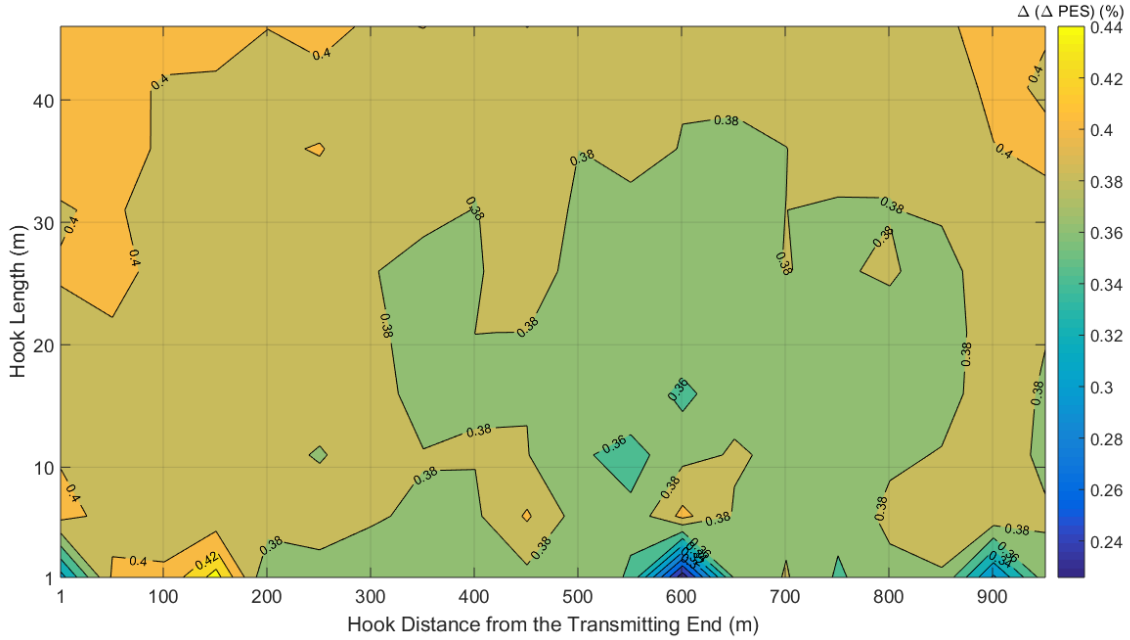
Δ (Δ PES) (%)
Hook Length (m)
Hook Distance from the Transmitting End (m)

(d)

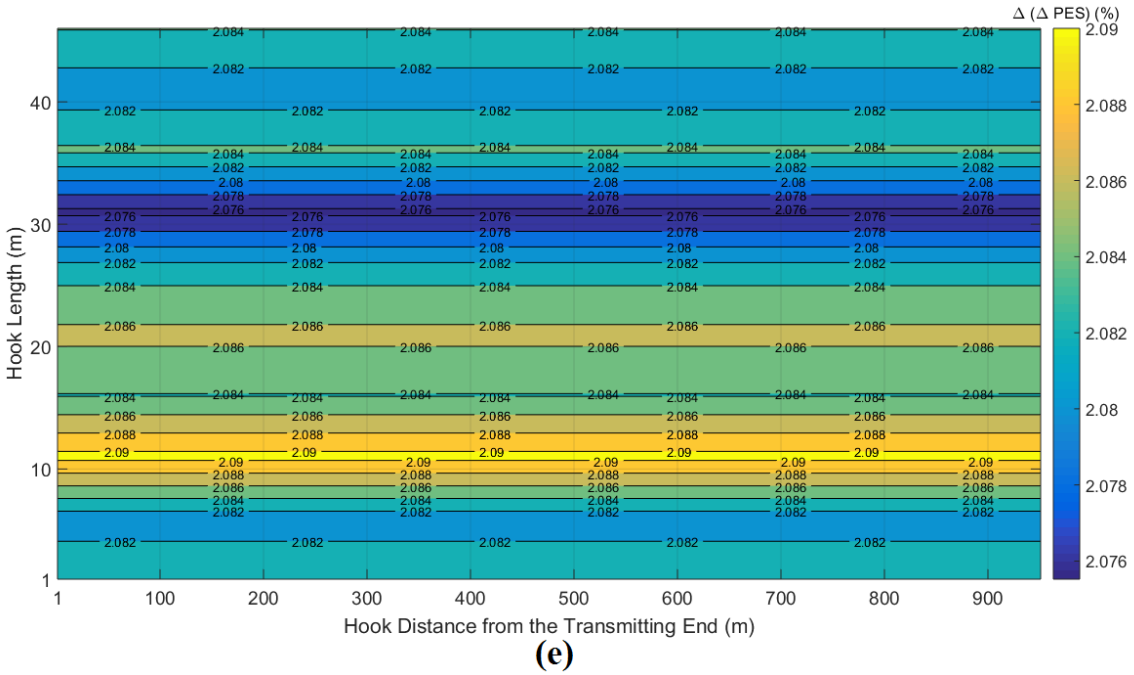

Fig. 7. Same curves with Fig. 6 but for measurement location deviation dev_t of 20 m.

the aforementioned areas are less affected by the measurement location deviations of Scenario B since the lowest in magnitude $\Delta(\Delta PES)$ values occur there. The opposite situation holds in the areas of more difficult hook style energy theft detection. For example, with reference to Figs. 3(a)-(e) of [20], the hook style energy theft detection in OV LV BPL "LOS" topologies remains easier when short hooks are applied regardless of the distance from the transmitting end while among the lowest $\Delta(\Delta PES)$ values occur in these cases with reference to Figs. 6(e) and 7(e).

From the previous findings, the main advantage of Scenario B is underlined that is the consideration of longer modified ad-hoc OV LV BPL topologies by the Information Technology department for the hook style energy theft detection since positive $\Delta(\Delta PES)$ values imply better performance of HS-DET method. When longer modified ad-hoc OV LV BPL topologies are used, the algebraic sum of measurement location deviations dev_t and dev_r rather than the exact installation positions of the transmitting and receiving end remain the important issue for Scenario B.

4.2 HS-DET Method and Longer Ad-Hoc OV LV BPL Topologies than the Typical OV LV BPL Topologies

When a complete OV LV BPL network is installed, this network can be divided into cascaded OV LV BPL topologies of typical lengths of 1000 m. In contrast, the main advantage of the installation of ad-hoc OV LV BPL topologies can be a more relaxed perspective regarding their lengths. If the hook style energy theft detection remains safe by HS-DET method, significantly longer lengths can be exploited for the ad-hoc OV LV BPL topologies. In order to assess the performance of HS-DET method through ΔPES, longer ad-hoc OV LV BPL topologies should be examined in urban,

suburban, rural and "LOS" environments. Note that each environment corresponds to a respective ad-hoc OV LV BPL topology class with reference to Tables 1-3. To examine the length impact of ad-hoc OV LV BPL topologies in the aforementioned environments, concatenated OV LV BPL topologies will be used; for example, the indicative ad-hoc OV LV BPL urban topology of Table 1 is equal to 1000 m, while the respective concatenated ad-hoc OV LV BPL urban topology without hook of v×1000m length is given in Table 3 where v is the number of concatenations. Although the concatenation of same OV LV BPL topology classes is a rather simplified and pessimistic approach, it can describe the BPL topology complexity of the urban, suburban, rural and "LOS" environments.

With reference to Tables 1 and 3, let assume that a concatenated ad-hoc OV LV BPL topology of v indicative ad-hoc OV LV BPL topologies (*i.e.*, the number of concatenation is equal to v) is first installed by the Information Technology department and collect the required reference data. After the uninstallation, a hook style energy theft occurs by using a hook of length L_{bh} that is hung at distance D_{h} from the transmitting end. Information Technology department reinstalls the same concatenated ad-hoc OV LV BPL topology without any measurement location deviations. In Fig. 8, ΔPES is plotted with respect to the number of concatenation v when $L_{\mathrm{bh}} = 5\mathrm{m}$ and $D_{\mathrm{h}} = 50\mathrm{m}$ are assumed for the five concatenated ad-hoc OV LV BPL topologies as described in Table 3. In Fig. 9, same curves with Fig. 8 are given but for $L_{\mathrm{bh}} = 40\mathrm{m}$ and $D_{\mathrm{h}} = (v \times 1000/2 + 1)\mathrm{m}$ while same curves with Fig. 8 are given in Fig. 10 but for $L_{\mathrm{bh}} = 20\mathrm{m}$ and $D_{\mathrm{h}} = (v \times 1000 - 30)\mathrm{m}$.

From Figs. 8-10, interesting findings can be reported concerning the detection of hook style energy theft when longer ad-hoc OV LV BPL topologies are installed by the Information Technology department. More specifically:

- The length and the class of the ad-hoc OV LV BPL topologies play critical role towards the hook style energy theft detection by ΔPES. However, the adoption of the conservative 1000 m typical length of OV LV BPL topologies remains an extremely safe decision regardless of the applied ad-hoc OV LV BPL topology class. Anyway, the hook style energy theft detection performance inversely depends on the length of the installed ad-hoc OV LV BPL topology.
- Depending on the examined OV LV BPL topology class, Information Technology department can adaptively install ad-hoc OV LV BPL topologies of different lengths. On the basis of a safe hook style energy theft detection that is assured by the strict 10% ΔPES threshold, Information Technology department can install:
    - ad-hoc "LOS" OV LV BPL topologies whose length may exceed 10 km;
    - ad-hoc rural OV LV BPL topologies whose length may reach up to 8 km;
    - ad-hoc suburban OV LV BPL topologies whose length may reach up to 4 km; and
    - ad-hoc urban OV LV BPL topologies whose length may reach up to 2 km (aggravated cases) even to 3 km (typical cases).
- Comparing Figs. 8-10, small ΔPES differences are observed for given ad-hoc OV LV BPL topology. This is due to the fact the hook length and the hook distance from the transmitting end has smaller effect on ΔPES rather than the number of

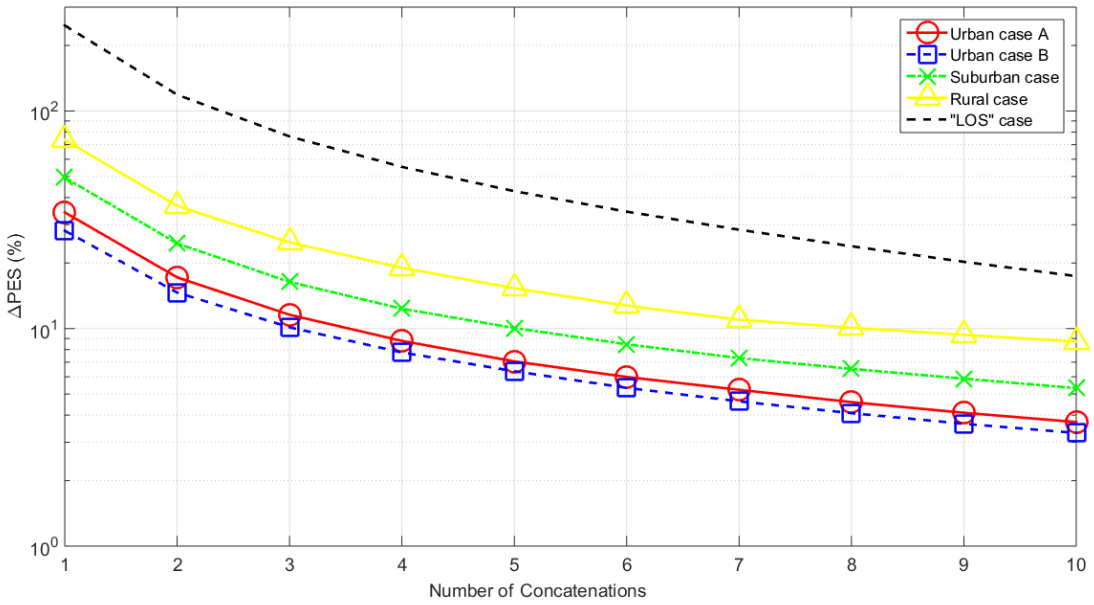

Fig. 8. ΔPES of HS-DET method for the five concatenated OV LV BPL topologies of Table 3 when hook length of 5 m and hook distance from the transmitting end of 50 m is assumed for different numbers of concatenations (y-axis is in logarithmic scale).

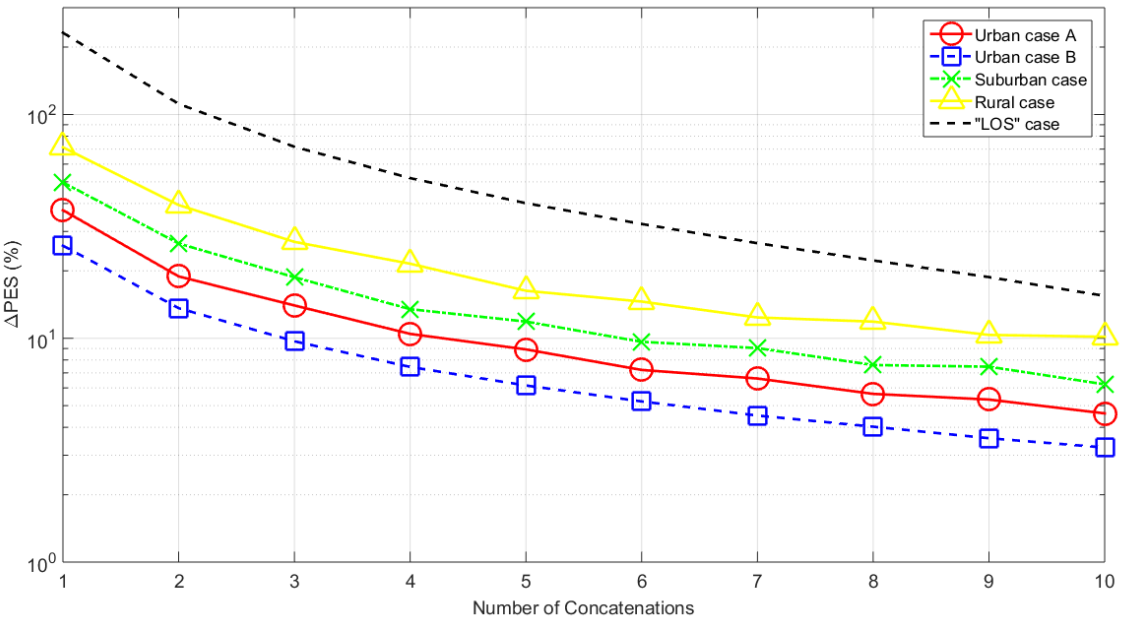

Fig. 9. Same curves with Fig. 8 but for hook length of 40 m and hook distance from the transmitting end of $(v \times 1000/2 + 1)$m.

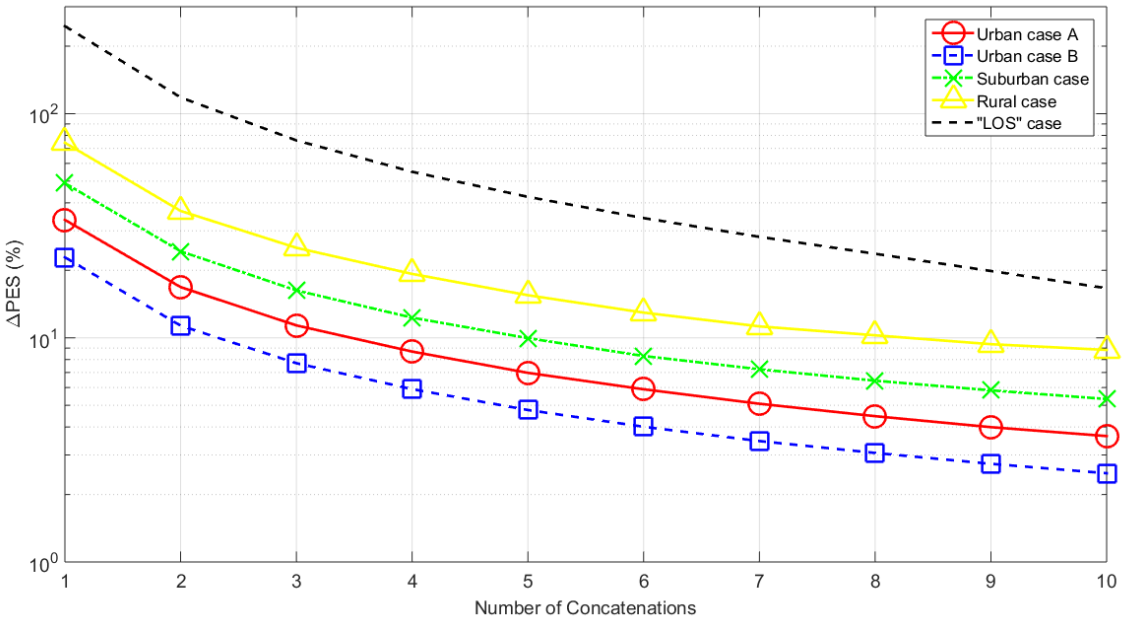

Fig. 10. Same curves with Fig. 8 but for hook length of 20 m and hook distance from the transmitting end of $(v \times 1000 - 30)$m.

concatenations. Anyway, a high number of concatenations implies that stronger multipath environments are created where the channel attenuation imposed by the hook remains smaller than the channel attenuation by the multipath environment because of the *v* multiple branches.

- In accordance with the findings of Secs. 4.1.1 and 4.1.2, Information Technology department can exploit the longer ad-hoc OV LV BPL topologies even if high accuracy regarding the installation positions lacks. Practically, Information Technology department should carefully report the first and the last branch of the ad-hoc OV LV BPL topology from which the reference measurements had been collected as the effect of additional or fewer MTL cable segments outside the topology range of the first and last branch on Δ*PES* remains negligible.
- In accordance with [20]-[22], measurement differences and various jamming techniques, which are not taken into consideration in this paper, have as impact the reduction of Δ*PES* values. In order to comply with the strict 10% Δ*PES* threshold, a small reduction of the number of concatenations can counteract this Δ*PES* aggravation.

Concluding this Section, an important remark is that there is no need for deploying a complete OV LV BPL network but a careful installation of an ad-hoc OV LV BPL topology for a hook style energy theft detection. In order to detect a hook style energy theft, longer ad-hoc OV LV BPL topologies than the typical OV LV BPL topologies can be installed by Information Technology department and the hook style energy theft detection can be successfully and easily made even with the strict 10% Δ*PES* threshold. Successful hook style energy theft detections can be made even if the lengths of the ad-hoc OV LV BPL topologies exceed 10km in "LOS" cases. But among the most critical topics of this Section is that there is no need for absolute

accuracy regarding the installation of the original and modified ad-hoc OV LV BPL topology. Even if measurement deviations occur at the transmitting and receiving end, the length should be assured by the Information Technology department that remains the same. Even if the length between the original and modified ad-hoc OV LV BPL topology is not the same, the influence of measurement deviations of transmitting and receiving end can be negligible if these measurement deviations are small fractions of the length of the examined ad-hoc OV LV BPL topology.

5. Conclusions

This paper has focused on the performance of HS-DET method when ad-hoc OV LV BPL topologies are installed by Information Technology departments of power utilities. In fact, two critical issues regarding the operation of ad-hoc OV LV BPL topologies have been discussed in this paper while their impact on the hook style energy theft detection by ΔPES of HS-DET method has been assessed; first, two scenarios regarding the measurement location deviation of the transmitting and receiving ends of the ad-hoc OV LV BPL topologies from the initial reference ad-hoc OV LV BPL topologies have been identified. In Scenario A, it has been proven that small measurement location deviations from the initial positions of the transmitting and receiving ends of the ad-hoc OV LV BPL topologies (*i.e.*, measurement location deviations up to 10 m) negligibly affect the hook style energy theft detection due to the symmetry attribute of BPL networks when the length of the original and the shifted ad-hoc OV LV BPL topology remains the same. In Scenario B, the effect of the measurement location deviations from the initial positions of the transmitting and receiving ends of the ad-hoc OV LV BPL topologies has been assessed but without the same length between the original and the shifted ad-hoc OV LV BPL topologies. Again, the hook style energy theft detection practically remains unaffected since ΔPES aggravation remains below 1% in the vast majority of the cases, which is significantly lower than the strict 10% ΔPES threshold for a safe hook style energy theft decision, when small measurement location deviations from the initial positions of the transmitting and receiving ends of the ad-hoc OV LV BPL topologies occur. Second, the impact of longer ad-hoc OV LV BPL topologies on the performance of hook style energy theft detection has been assessed. It has been proven that Information Technology department can deploy ad-hoc OV LV BPL topologies whose length can comfortably exceed 2 km and even 10 km depending on the examined OV LV BPL topology class; say, the smart grid environment. In conclusion, a wise management of ad-hoc OV LV BPL topologies by Information Technology department, *e.g.*, an accurate installation plan and an updated database management system, can secure extremely safe decisions concerning the hook style energy theft detection in all the cases examined without the need of additional costs concerning either specialized equipment or a complete BPL network.

CONFLICTS OF INTEREST

The author declares that there is no conflict of interests regarding the publication of this paper.

References

[1] C. H. Lo, and N. Ansari, "CONSUMER: A Novel Hybrid Intrusion Detection System for Distribution Networks in Smart Grid," *IEEE Transactions on Emerging Topics in Computing*, vol. 1, no. 1, pp. 33-44, 2013.

[2] R. Jiang, R. Lu, Y. Wang, J. Luo, C. Shen, and X. S. Shen, "Energy-theft Detection Issues for Advanced Metering Infrastructure in Smart Grid," *Tsinghua Science and Technology*, vol. 19, no. 2, pp. 105-120, 2014.

[3] P. Jokar, N. Arianpoo, and V. CM Leung, "Electricity Theft Detection in AMI Using Customers' Consumption Patterns," *IEEE Transactions on Smart Grid*, vol. 7, no. 1, pp. 216-226, 2016.

[4] S. Salinas, M. Li, and P. Li, "Privacy-preserving Energy Theft Detection in Smart Grids: A P2P Computing Approach," *IEEE Journal on Selected Areas in Communications*, vol. 31, no. 9, pp. 257-267, 2013.

[5] D. R. Pereira, M. A. Pazoti, L. A. Pereira, D. Rodrigues, C. O. Ramos, A. N. Souza, and J. P. Papa, "Social-Spider Optimization-based Support Vector Machines applied for energy theft detection," *Computers & Electrical Engineering*, vol. 49, pp. 25-38, 2016.

[6] S. Salinas, M. Ming, and P. Li, "Privacy-preserving Energy Theft Detection in Smart Grids," *Sensor, Mesh and Ad Hoc Communications and Networks (SECON), 2012, in proc. 9th Annual IEEE Communications Society Conference on. IEEE*, pp. 605-613, 2012.

[7] S. McLaughlin, B. Holbert, S. Zonouz, and R. Berthier, "AMIDS: A Multi-sensor Energy Theft Detection Framework for Advanced Metering Infrastructures," in *Smart Grid Communications (SmartGridComm), in proc of 2012 IEEE Third International Conference on*, pp. 354-359, Nov. 2012.

[8] P. McDaniel and S. McLaughlin, "Security and Privacy Challenges in the Smart Grid," *IEEE Security & Privacy*, vol. 7, no. 3, pp. 75-77, 2009.

[9] Federal Court of Audit, "Operational Audit Report Held in National Agency of Electrical Energy, ANEEL, Brazil", *Rep. no. TC 025.619/2007-2*, Brasília, Brazil, 2007.

[10] Ministry of Power, India, "Overview of power distribution," *Tech. Rep.*, http://www.powermin.nic.in, 2013.

[11] A. G. Lazaropoulos, "Measurement Differences, Faults and Instabilities in Intelligent Energy Systems – Part 1: Identification of Overhead High-Voltage Broadband over Power Lines Network Topologies by Applying Topology Identification Methodology (TIM)," *Trends in Renewable Energy*, vol. 2, no. 3, pp. 85 – 112, Oct. 2016.

[12] A. G. Lazaropoulos, "Measurement Differences, Faults and Instabilities in Intelligent Energy Systems – Part 2: Fault and Instability Prediction in Overhead High-Voltage Broadband over Power Lines Networks by Applying Fault and Instability Identification Methodology (FIIM)," *Trends in Renewable Energy*, vol. 2, no. 3, pp. 113 – 142, Oct. 2016.

[13] A. G. Lazaropoulos, "Power Systems Stability through Piecewise Monotonic Data Approximations – Part 2: Adaptive Number of Monotonic Sections and Performance of L1PMA, L2WPMA and L2CXCV in Overhead Medium-Voltage Broadband over Power Lines Networks," *Trends in Renewable Energy*, vol. 3, no. 1, pp. 33 – 60, Jan. 2017.

[14] A. G. Lazaropoulos, "Power Systems Stability through Piecewise Monotonic Data Approximations – Part 1: Comparative Benchmarking of L1PMA, L2WPMA and L2CXCV in Overhead Medium-Voltage Broadband over Power Lines Networks," *Trends in Renewable Energy*, vol. 3, no. 1, pp. 2 – 32, Jan. 2017.

[15] A. N. Stefanidi, I. A. Panos, A. N. Milioudis, and G. T. Andreou, "Sympathetic Tripping in a Field Case Study," In *2018 IEEE 53rd International Universities Power Engineering Conference (UPEC)*, pp. 1-5, Sep. 2018.

[16] A. G. Paspatis, G. C. Konstantopoulos, T. A. Papadopoulos, and V. C. Nikolaidis, "Dynamic grid voltage support from distributed energy resources during short-circuits," In *2017 IEEE 52nd International Universities Power Engineering Conference (UPEC)*, pp. 1-6, Aug. 2017.

[17] A. G. Lazaropoulos, "Main Line Fault Localization Methodology in Smart Grid – Part 1: Extended TM2 Method for the Overhead Medium-Voltage Broadband over Power Lines Networks Case," *Trends in Renewable Energy*, vol. 3, no. 3, pp. 2-25, Dec. 2017.

[18] A. G. Lazaropoulos, "Main Line Fault Localization Methodology in Smart Grid – Part 2: Extended TM2 Method, Measurement Differences and L1 Piecewise Monotonic Data Approximation for the Overhead Medium-Voltage Broadband over Power Lines Networks Case," *Trends in Renewable Energy*, vol. 3, no. 3, pp. 26-61, Dec. 2017.

[19] A. G. Lazaropoulos, "Main Line Fault Localization Methodology in Smart Grid – Part 3: Main Line Fault Localization Methodology (MLFLM)," *Trends in Renewable Energy*, vol. 3, no. 3, pp. 62-81, Dec. 2017.

[20] A. G. Lazaropoulos, "Detection of Energy Theft in Overhead Low-Voltage Power Grids – The Hook Style Energy Theft in the Smart Grid Era," *Trends in Renewable Energy*, vol. 5, no. 1, pp. 12 – 46, Oct. 2018.

[21] A. G. Lazaropoulos, "Special Cases during the Detection of the Hook Style Energy Theft in Overhead Low-Voltage Power Grids through HS-DET Method – Part 1: High Measurement Differences, Very Long Hook Technique and "Smart" Hooks," *Trends in Renewable Energy*, vol. 5, no. 1, pp. 60-89, Jan. 2019.

[22] A. G. Lazaropoulos, "Special Cases during the Detection of the Hook Style Energy Theft in Overhead Low-Voltage Power Grids through HS-DET Method – Part 2: Different Measurement Differences, Feint "Smart" Hooks and Hook Interconnection Issues," *Trends in Renewable Energy*, vol. 5, no. 1, pp. 90-116, Jan. 2019.

[23] A. G. Lazaropoulos, "Towards Modal Integration of Overhead and Underground Low-Voltage and Medium-Voltage Power Line Communication Channels in the Smart Grid Landscape: Model Expansion, Broadband Signal Transmission Characteristics, and Statistical Performance Metrics (Invited Paper)," *ISRN Signal Processing*, vol. 2012, Article ID 121628, pp. 1-17, 2012. [Online]. Available: http://www.hindawi.com/isrn/sp/2012/121628/

[24] A. G. Lazaropoulos, "Towards broadband over power lines systems integration: Transmission characteristics of underground low-voltage distribution power lines," *Progress in Electromagnetics Research B*, 39, pp. 89-114, 2012. [Online]. Available: http://www.jpier.org/PIERB/pierb39/05.12012409.pdf

[25] A. G. Lazaropoulos and P. G. Cottis, "Transmission characteristics of overhead medium voltage power line communication channels," *IEEE Trans. Power Del.*, vol. 24, no. 3, pp. 1164-1173, Jul. 2009.

[26] A. G. Lazaropoulos and P. G. Cottis, "Capacity of overhead medium voltage power line communication channels," *IEEE Trans. Power Del.*, vol. 25, no. 2, pp. 723-733, Apr. 2010.
[27] A. G. Lazaropoulos and P. G. Cottis, "Broadband transmission via underground medium-voltage power lines-Part I: transmission characteristics," *IEEE Trans. Power Del.*, vol. 25, no. 4, pp. 2414-2424, Oct. 2010.
[28] A. G. Lazaropoulos and P. G. Cottis, "Broadband transmission via underground medium-voltage power lines-Part II: capacity," *IEEE Trans. Power Del.*, vol. 25, no. 4, pp. 2425-2434, Oct. 2010.
[29] A. G. Lazaropoulos, "Broadband transmission characteristics of overhead high-voltage power line communication channels," *Progress in Electromagnetics Research B*, vol. 36, pp. 373-398, 2012. [Online]. Available: http://www.jpier.org/PIERB/pierb36/19.11091408.pdf
[30] A. G. Lazaropoulos, "Green Overhead and Underground Multiple-Input Multiple-Output Medium Voltage Broadband over Power Lines Networks: Energy-Efficient Power Control," *Springer Journal of Global Optimization*, vol. 2012 / Print ISSN 0925-5001, pp. 1-28, Oct. 2012.
[31] A. G. Lazaropoulos, "Deployment Concepts for Overhead High Voltage Broadband over Power Lines Connections with Two-Hop Repeater System: Capacity Countermeasures against Aggravated Topologies and High Noise Environments," *Progress in Electromagnetics Research B*, vol. 44, pp. 283-307, 2012. [Online]. Available: http://www.jpier.org/PIERB/pierb44/13.12081104.pdf
[32] A. G. Lazaropoulos, "Broadband transmission and statistical performance properties of overhead high-voltage transmission networks," *Hindawi Journal of Computer Networks and Commun.*, 2012, article ID 875632, 2012. [Online]. Available: http://www.hindawi.com/journals/jcnc/aip/875632/
[33] P. Amirshahi and M. Kavehrad, "High-frequency characteristics of overhead multiconductor power lines for broadband communications," *IEEE J. Sel. Areas Commun.*, vol. 24, no. 7, pp. 1292-1303, Jul. 2006.
[34] T. Calliacoudas and F. Issa, ""Multiconductor transmission lines and cables solver," An efficient simulation tool for plc channel networks development," presented at the *IEEE Int. Conf. Power Line Communications and Its Applications*, Athens, Greece, Mar. 2002.
[35] T. Sartenaer and P. Delogne, "Deterministic modelling of the (Shielded) outdoor powerline channel based on the multiconductor transmission line equations," *IEEE J. Sel. Areas Commun.*, vol. 24, no. 7, pp. 1277-1291, Jul. 2006.
[36] C. R. Paul, *Analysis of Multiconductor Transmission Lines*. New York: Wiley, 1994.
[37] H. Meng, S. Chen, Y. L. Guan, C. L. Law, P. L. So, E. Gunawan, and T. T. Lie, "Modeling of transfer characteristics for the broadband power line communication channel," *IEEE Trans. Power Del.*, vol. 19, no. 3, pp. 1057-1064, Jul. 2004.
[38] B. Li, D. Mansson, and G. Yang, "An efficient method for solving frequency responses of power-line networks," Progress In Electromagnetics Research B, Vol. 62, 303-317, 2015. doi:10.2528/PIERB15013008 http://www.jpier.org/pierb/pier.php?paper=15013008
[39] M. Chaaban, K. El KhamlichiDrissi, and D. Poljak, "Analytical model for electromagnetic radiation by bare-wire structures," Progress In Electromagnetics

Research B, Vol. 45, 395-413, 2012. doi:10.2528/PIERB12091102 http://www.jpier.org/pierb/pier.php?paper=12091102

[40] Y. H. Kim, S. Choi, S. C. Kim, and J. H. Lee, "Capacity of OFDM two-hop relaying systems for medium-voltage power-line access networks," *IEEE Trans. Power Del.*, vol. 27, no. 2, pp. 886-894, Apr. 2012.

[41] P. Amirshahi and M. Kavehrad, "Medium voltage overhead powerline broadband communications; Transmission capacity and electromagnetic interference," in *Proc. IEEE Int. Symp. Power Line Commun. Appl.*, Vancouver, BC, Canada, Apr. 2005, pp. 2-6.

[42] M. Tang, and M. Zhai, "Research of transmission parameters of four-conductor cables for power line communication," in *Proc. Int. Conf. on Computer Science and Software Engineering*, Wuhan, China, Dec. 2008, vol. 5, pp. 1306–1309.

[43] M. D'Amore and M. S. Sarto, "A new formulation of lossy ground return parameters for transient analysis of multiconductor dissipative lines," *IEEE Trans. Power Del.*, vol. 12, no. 1, pp. 303-314, Jan. 1997.

[44] M. D'Amore and M. S. Sarto, "Simulation models of a dissipative transmission line above a lossy ground for a wide-frequency range-Part I: Single conductor configuration," *IEEE Trans. Electromagn. Compat.*, vol. 38, no. 2, pp. 127-138, May 1996.

[45] M. D'Amore and M. S. Sarto, "Simulation models of a dissipative transmission line above a lossy ground for a wide-frequency range-Part II: Multi-conductor configuration," *IEEE Trans. Electromagn. Compat.*, vol. 38, no. 2, pp. 139-149, May 1996.

[46] N. Theethayi, "Electromagnetic interference in distributed outdoor electrical systems, with an emphasis on lightning interaction with electrified railway network," Ph.D. dissertation, Uppsala Univ., Uppsala, Sweden, Sep. 2005, [Online]. Available: http://uu.diva-portal.org/smash/get/diva2:166746/FULLTEXT01

[47] A. G. Lazaropoulos, "Review and Progress towards the Common Broadband Management of High-Voltage Transmission Grids: Model Expansion and Comparative Modal Analysis," *ISRN Electronics*, vol. 2012, Article ID 935286, pp. 1-18, 2012. [Online]. Available: http://www.hindawi.com/isrn/electronics/2012/935286/

[48] A. G. Lazaropoulos, "New Coupling Schemes for Distribution Broadband over Power Lines (BPL) Networks," *Progress in Electromagnetics Research B*, vol. 71, pp. 39-54, 2016. [Online]. Available: http://www.jpier.org/PIERB/pierb71/02.16081503.pdf

[49] A. G. Lazaropoulos, "Broadband Performance Metrics and Regression Approximations of the New Coupling Schemes for Distribution Broadband over Power Lines (BPL) Networks," *Trends in Renewable Energy*, vol. 4, no. 1, pp. 43 – 73, 2018.

[50] T. C. Banwell and S. Galli, "On the symmetry of the power line channel," in *Proc. Int. Symp. Power-Lines Commun*, pp. 325-330. 2001.

[51] S. Galli and T. Banwell, "A novel approach to the modeling of the indoor power line channel-Part II: Transfer function and its properties," *IEEE Transactions on Power Delivery*, vol. 20, no. 3, pp. 1869-1878, 2005.

Trends in Renewable Energy
OPEN ACCESS ISSN: 2376-2144
Peer-Reviewed Article futureenergysp.com/index.php/tre

Production of Biochar Based Porous Carbon Nanofibers for High-Performance Supercapacitor Applications

Shuangning Xiu[1,a], Spero Gbewonyob[2,a], Abolghasem Shahbazi[1,*], Lifeng Zhang[2,*]

1. *Biological Engineering Program, Department of Natural Resource and Environmental Design, North Carolina A&T State University, Greensboro, NC, U.S.A*
2. *Joint School of Nanoscience and Nanotechnology, North Carolina A&T State University, Greensboro, NC, U.S.A*

[a] *These two authors contributed equally to this work.*

Received February 10, 2019; Accepted April 4, 2019; Published April 8, 2019

Biomass-derived biochar was used as the precursor to synthesize porous carbons for supercapacitor electrodes. The biochar was first activated with KOH to generate porous carbon material and then fabricated into highly flexible porous carbon nanofibers (ECNF) by electrospinning technique. Activated carbons with a surface area of around 2258 m^2/g were found. The resultant biochar based ECNF mats exhibited outstanding mechanical flexibility and electrochemical properties as free-stranding and binder free electrodes of supercapacitor. The PAN/BCK3 ECNFs, which were made from the composite of polyacrylonitrile (PAN) and KOH-activated biochar (mass ratio of Biochar/KOH =1:3) exhibited the highest gravimetric capacitance (108 F/g at current density of 0.5 A/g) with high retention (96% at 1 A/g) due to its well-developed micro-mesoporosity. The results indicated that biomass-derived biochar is a promising material which can be used for the production of low cost high performance electrode materials for supercapacitor.

Keywords: Biochar; Pyrolysis; Supercapacitor; Nanofiber; Activated carbon

Introduction

The excessive burning of fossil fuel has caused serious problems such as the global warming, environmental pollution, and energy crisis. Sustainable development requires discovering renewable and environmentally friendly technologies with the aim of resolving these problems. Among various newly developed energy technologies, supercapacitor, an energy storage device, has received great attention due to its high-power density, long cycle life, and quick charge/discharge capability [1, 2]. Supercapacitor can be used as uninterruptible power sources in electric vehicles, digital communications system, pulsing techniques, etc. [3, 4]. The microstructure of supercapacitor electrodes has a great influence on supercapacitor performance. Carbon material with high surface area and rich porous structure are the primary raw materials for making supercapacitors due to its high electric conductivity, strong mechanical property, wide availability, and low environmental impacts [5, 6]. However, high quality carbon materials like fullerene, graphene, and carbon nanotubes are hard to synthesize

*Corresponding author: ash@ncat.edu (A. Shahbazi); lzhang@ncat.edu (L. Zhang)

Tr Ren Energy, 2019, Vol.5, No.2, 151-164. doi: 10.17737/tre.2019.5.2.0095

and expensive for massive production [6, 7]. Therefore, producing attractive, high quality carbon materials from sustainable and low cost precursors is critical for the development of the supercapacitor industry [8].

Recently, biochar, a product from biomass thermochemical conversion, has received increasing attention for the use in several applications due to the cheap, abundant, and sustainable advantages [9]. In general, the bio-char is considered as waste byproduct or low value product [10]. The most common biochar application is soil amendment to mitigate greenhouse gas emission and improve soil health. Recent developments in activation procedures and/or precursors allow a better control over the pore structure and surface property. These characteristics have widened the use of biochar to more demanding applications, including using biochar as a precursor for making catalysts, energy storage, gas storage and contaminant adsorbents [9]. These new high-value applications are still in their infancy, and further research and development are needed to reach commercialization.

Up to now, various type porous carbon based electrode materials have been reported in the literature, such as spherical carbon [11], fibrous carbon [12], powdery carbon [13] *et al.* Among which, activated carbon fibers attract increasing interests owning to their unique microspores, light weight, free standing, high strength, fatigue endurance, and thermal resistance [14]. However, binders (organic/polymeric materials) are typically required for binding the powders/particles of the carbons to prepare the free-standing electrodes [15]. Such binders would reduce the overall performance of the electrodes. Hence, it is still a technological challenge to develop mechanically flexible electrodes with superior electrochemical performance.

The recent reported freestanding electrospun carbon nanofibers (ECNFs) prepared by electrospinning technique showed some promising advantages in the preparation process, ion transmission, and cost for using as free-standing, and binder-free electrode materials [12, 16]. However, the specific surface area (SSA) of ECNF (10-30 m^2/g) is much lower than those of graphene (272 m^2/g) and carbon nanotubes (909 m^2/g) [16, 17]. To improve the specific capacitance and energy density of ECNFs based supercapacitors, many researchers have tried to incorporate some conductive and flexible materials such as graphene nanosheet, cobalt nitrite, and transition metal oxidizes to improve the SSA, flexibility, and conductivity of ECNF [16, 18, 19]. Although the performance of ECNF materials has been greatly improved, it still remains a challenge to prepare a flexible and low cost ECNF for energy storage systems due to the rigid nature of the metal materials, poor electrical conductivity, high cost, and toxicity.

In this work, biomass-derived biochar was used as the precursor to synthesize porous carbons for supercapacitor electrodes. Highly flexible porous biochar based ECNFs were for the first time fabricated by electrospinning technique and explored as electrode material. The main advantage of the prepared carbon material is its source (*i.e.*, abundant/inexpensive biochar), and the biochar-based ECNFs can be directly used as binder-free electrode for high performance supercapacitor electrodes.

Materials and Methods

2.1. Biochar and Activation

The raw biochar was prepared by fast pyrolysis of loblolly pine sawdust, which was followed by sieving into the particle size range of 0.18-0.25 mm [20]. The biochar based actived carbons were prepared from raw biochar via KOH activation method. Typically, the raw biochar was mixed with potassium hydroxide (KOH, Fisher Scientific Inc.) in a different mass ratio (1:1, 1:2, 1:3) and small amount of water in a crucible. Then the crucible was placed in a muffle furnace and activated at 800°C for 1 h at a heating rate of 10 °C /mn under N_2 protection with a flow rate of 96 ml/min. After cooling down to room temperature, the KOH activated carbon were washed with 0.1 M HCl at 60°C for 1 h in a shaker to remove the residual KOH and impurities. Finally, the carbon was washed several times with deionized water until the pH value became neutral. The carbon material was then dried at 105°C overnight in an conveintal oven. The KOH activated biochar based carbons were denoted as BCK1, BCK2 and BCK3 for biochar/KOH mass ratio of 1:1, 1:2 and 1:3, respectively. For comparison purpose, samples prepared using the same procedure but without KOH treatment was denoted as BCK0.

2.2. Preparation of Biochar Based Carbon Nanofibers

Polyacrylonitrile (PAN, Mw = 150,000, product number: 227056) and *N*,*N*-dimethylformamide (DMF) (product number: 227056) were purchased from Sigma-Aldrich. The chemicals were used as received without further purification.

A 10 wt% bicomponent solution was prepared by dissolving PAN and biochar in the mass ratio of 30:70 in DMF. Biochar was first dispersed in DMF and sonicated for 30 mins, and then added to PAN solution under constant stirring. A 30 ml syringe was next filled with the spinning solution and fitted with a blunt end 15-gauge stainless steel needle. As shown in Fig.1, the electrospinning setup comprised of a high voltage power supply (Series FX, Glassman High Voltage Inc., New Jersey, USA) and a flat movable stainless steel collector plate. The collector setup was fabricated in house and made up of two slides, a computer with a software that controls the motion, and a 30 inch by 30-inch stainless steel plate. The solution was electrospun at a flow rate of 1 ml/h and 15 kV and collected on a grounded aluminum foil that was placed at 20 cm from the tip of the syringe. The resulting electrospun fiber mats were detached from the collector and dried at room temperature in a fume hood for at least 24 h before further use. The collected electrospun fiber mats were then cut and stacked between 6×6 in. graphite plates (graphite store), and placed in a furnace (Carbolite HTF 18/8, Sheffield, UK) for further heat treatment. All the samples were stabilized in air from room temperature to 280°C at a heating rate of 1 °C/min and the temperature was held at 280°C for 6 h to allow complete stabilization. After the stabilized fibers were cooled down to room temperature, they are carbonized in nitrogen at 1200°C with a heating rate of 5 °C/min and held for 1 h before cooled down to room temperature.

2.3. Material Characterization

The physical characterization of biochar based activated carbon and biochar based ECNFS was conducted by using elemental analysis, nitrogen sorption method, and scanning electron microscopy (SEM). The surface morphology and structure of biochar based carbon and biochar based ECNFs were examined by a Carl Zeiss Auriga-BU FIB field emission scanning electron microscope (FESEM, Oberkochen, Germany). Specific surface area, pore volume, and pore size distribution were measured with a surface area and porosity analyzer (Micromeritics ASAP2020, Georgia, USA). The multilayer

adsorption model developed by Brunauer-Emmett-Teller (BET) was used to evaluate the surface area (SBET), while the pore size distribution of the sample was evaluated using the Barrett-Joyner-Halenda (BJH) model. Elemental analyses for carbon, hydrogen, and nitrogen contents were determined by using a Perkin-Elmer 2400 CHN/S analyzer (Waltham, MA, USA).

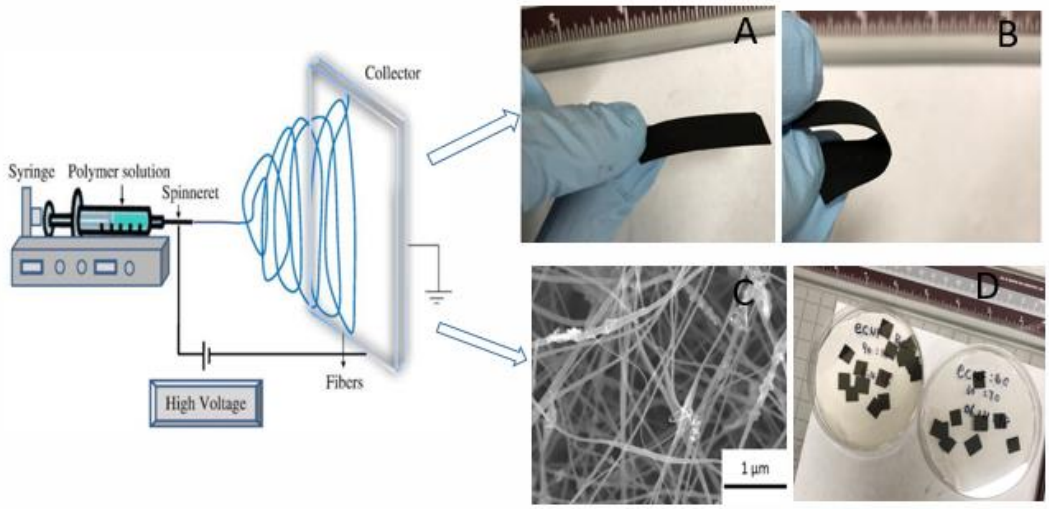

Fig. 1. Schematic illustration for obtaining porous ECNF electrodes using electrospinning method. A) and B) Photo of the ECNF; C) SEM of the ECNF; D) Photo of the electrode

2.4. Electrochemical Test

The system for measuring the electrochemical performance of the supercapacitor electrode material is composed of three key components: the electrochemical cell, the electrochemical workstation, and a computer for acquiring test data and control of the workstation. All required electrochemical parameters of the supercapacitor electrode material can be measured using the CHI660E electrochemical workstation (CH Instruments, Inc., Texas, USA). The three-electrode configuration was assembled using different PAN/Biochar ECNFs mats as working electrodes (size ~1.0 cm^2). The mass of each carbon fiber mat was measured with an electronic balance. A Pt wire and the Ag/AgCl electrode were applied as the counter and reference electrodes, respectively. The working and reference electrodes were first immersed in aqueous electrolyte solution 6 M NaOH for 24 h; subsequently, cyclic voltammetry (CV) measurement was performed at the scan rate of 5–100 $mV \cdot s^{-1}$, and the potential window was selected from −0.4 to 0.4 V. For the galvanostatic charge/discharge measurements, the potential window was set from −0.4 to 0.4 V with current densities from 2 to 0.4 A/g. The electoral conductivity of the ECNFs was also measured through electrochemical impedance spectroscope (EIS) (*i.e.,* frequency response analysis yields over the frequency ranging from 0.1 Hz to 100,1000 Hz with potential amplitude of 5 mV). All of the electrochemical tests were performed on CHI660E electrochemical testing station.

The specific capacitance of the prepared carbons was calculated from the galvanostatic charge/discharge test at different current density, by the following formula:

$$C = \frac{2I \times \Delta t}{m \times \Delta V} \quad (1)$$

Where, I is the charge or discharge current density, Δt is the discharge time, m is the mass of the electrode, and ΔV is potential voltage, while C is the gravimetric capacitance (F/g).

Results and Discussion

3.1. The Effect of Activation on the Elemental Composition of Biochar

Table 1 shows the elemental analysis results of the raw biochar and activated biochar carbons obtained from different KOH ratios. It was observed that the hydrogen, oxygen, nitrogen and sulfur content were all decreased while the carbon content increased after the chemical activation. This indicates an effective carbonization due to the heat treatment during the activation process. The activated biochar BCK2 has the highest carbon content of 78.48%, while BCK3 sample has the highest nitrogen content among the three samples.

Table 1. Elemental analysis results of the biochar and activated biochar carbon

Sample	C (%)	H (%)	O (%)	N (%)	S (%)
Original Biochar (BCK0)	72.38	4.07	23.78	2.91	0.83
Activated Biochar BCK1 (Char: KOH=1:1)	77.21	1.33	22.41	0.15	0.23
Activated Biochar BCK2 (Char:KOH=1:2)	78.48	2.02	20.69	0.46	0.37
Activated Biochar BCK3 (Char:KOH=1:3)	77.85	1.64	21.11	0.72	0.32

3.2. The Effect of Aactivation on the Pore Characteristics of Biochar

The morphology and microstructure of the typical samples were analyzed by using SEM. Fig. 2 depicts the surface morphologies of the raw biochar and activated biochars obtained via KOH treatment with different KOH ratios. SEM images of BCK1 are not presented here due to the similarity to BCK2 and BCK3. It was observed that the raw biochar revealed relatively smooth irregular surfaces. On contrast, the activated biochar showed rougher surfaces with hierarchical and porous structure clearly appeared, indicating more porous structure than the relatively less porous of raw biochar. This change is believed to be originated from KOH activation under pyrolysis.

In the KOH activation process, synergistic effects, including etching, gasification, and intercalation were found to be responsible for the pore network formation, porosity enhancement and lattice expansion, respectively [21] . These synergistic effects produced hierarchical porous carbon materials with large SSA and high porosity. Large SSA can increase the double layer capacitance since it provides more chances contacting between the electrode materials and electrolyte. This is desired for the electrode application and were expected to lead to an improvement in capacitance performance.

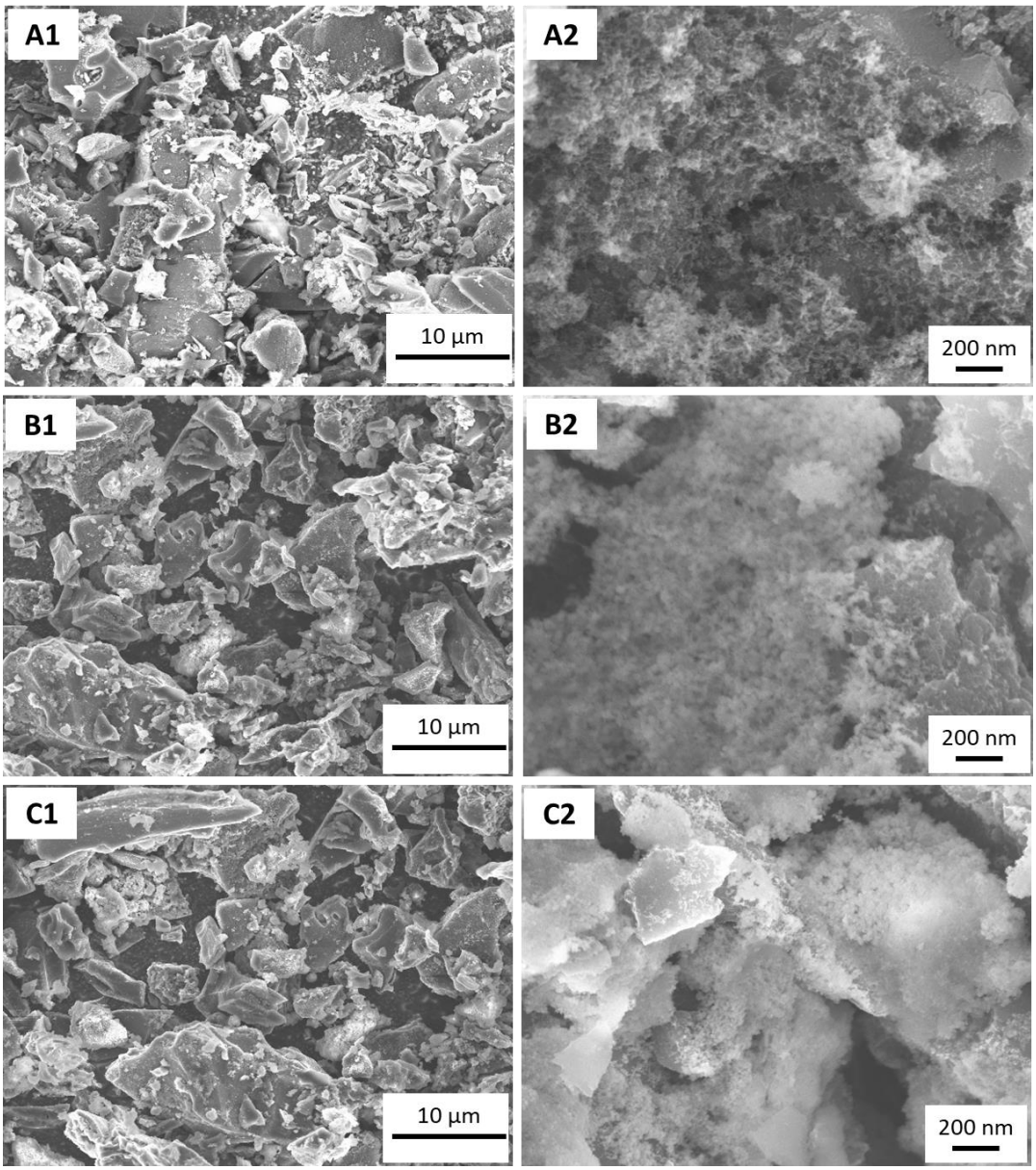

Fig. 2. SEM showing the morphology of biochar A1 and A2) raw biochar BCK0; B1 and B2) BCK2; C1 and C2) BCK3

To verify the speculation on high SSA and pore structure observed in SEM images, Specific surface area, pore volume, and pore size distribution were measured. Details of the pore characteristic of biochar and activated biochar carbon samples are given in Table 2. This result indicates that the KOH activation greatly enhanced the pore development during the activation process. The ratio of KOH/biochar significantly affects the microstructure of the resultant carbon. The higher the KOH to biochar ratio, the higher surface area and larger pore volume. The optimized biochar based activated carbon material possesses typical hierarchical porosity composed of multi-leveled pores with high surface area and pore volume up to 2,258 m^2/g and 1.19 cm^3/g, respectively.

Table 2 The specific surface area (SSA), volume, pore size, and average diameter of biochar based Carbon

Sample	BET SSA (m^2g^{-1})	Average Pore Size (nm)	Pore Volume (cm^3g^{-1})
Original Biochar (BCK0)	627	5.78	0.42
Activated Biochar BCK1 (Char: KOH=1:1)	1083	2.4	0.65
Activated Biochar BCK2 (Char:KOH=1:2)	1799	2.1	0.95
Activated Biochar BCK3 (Char:KOH=1:3)	2258	2.1	1.19

3.3. Morphological and structural properties of Biochar/PAN derived ECNFs.

An aqueous mixture containing biochar alone could not be electrospun into nanofibers due to the lack of macromolecular structure/entanglements. Uniform PAN solution, by contrast, could be electrospun into PAN nanofibers with an average diameter of ~300 nm according to our earlier research [12]. As can be seen from Fig. 1 A&B, the resultant PAN/Biochar derived ECNFs is not only free standing but also displays outstanding mechanical flexibility. There are no identifiable cracks or broken fibers can be observed under repeatedly bending, even to 180^o. In comparison, the PAN only nanofibers are more fragile. The improved flexibility of biochar derived ECNF might due to the flexible nature of biochar derived from lignocellulosic biomass and high graphitization degree caused by the thermal treatment. The mechanical flexibility would make the PAN/Biochar derived ECNF film suitable for various potential applications such as wearable and portable devices and flexible electronics.

Fig. 3 shows the morphological structures of the PAN/Biochar derived ECNFs. As shown in Fig.3, these PAN/Biochar derived ECNFs consisted of non-woven, randomly oriented carbon nanofibers with a coarse morphology and a large quantity of biochar particles entrapped among the fibers considering the size of most of the biochar particles was large to be incorporated in the fibers. The magnified SEM images in Fig. 3 A2, B2 and C2 further demonstrate that there is certain amount of fine biochar incorporated into the electrospun carbon fibers. The average diameter of the biochar/PAN derived ECNFs was between 56~100 nm, while the average diameter of the PAN alone ECNF was around 300 nm. This significant deduction in fiber diameter might be due to that most of the hydrogen, oxygen and sulfur in the biochar were removed during the thermal treatments, leading to deduction in diameter and the formation of carbonaceous structures. This was also confirmed by the elemental analysis result listed in Table 1. SEM results also revealed that with the increase of KOH ratio in the chemical activation of the biochar particles, the average diameters of the ECNFs gradually increased from ~56 nm to ~100nm. This could be because after activation, the biochar particles are easier to be broken down into smaller sizes during sonication. Hence a lot more are embedded in the fibers thereby increasing their average sizes.

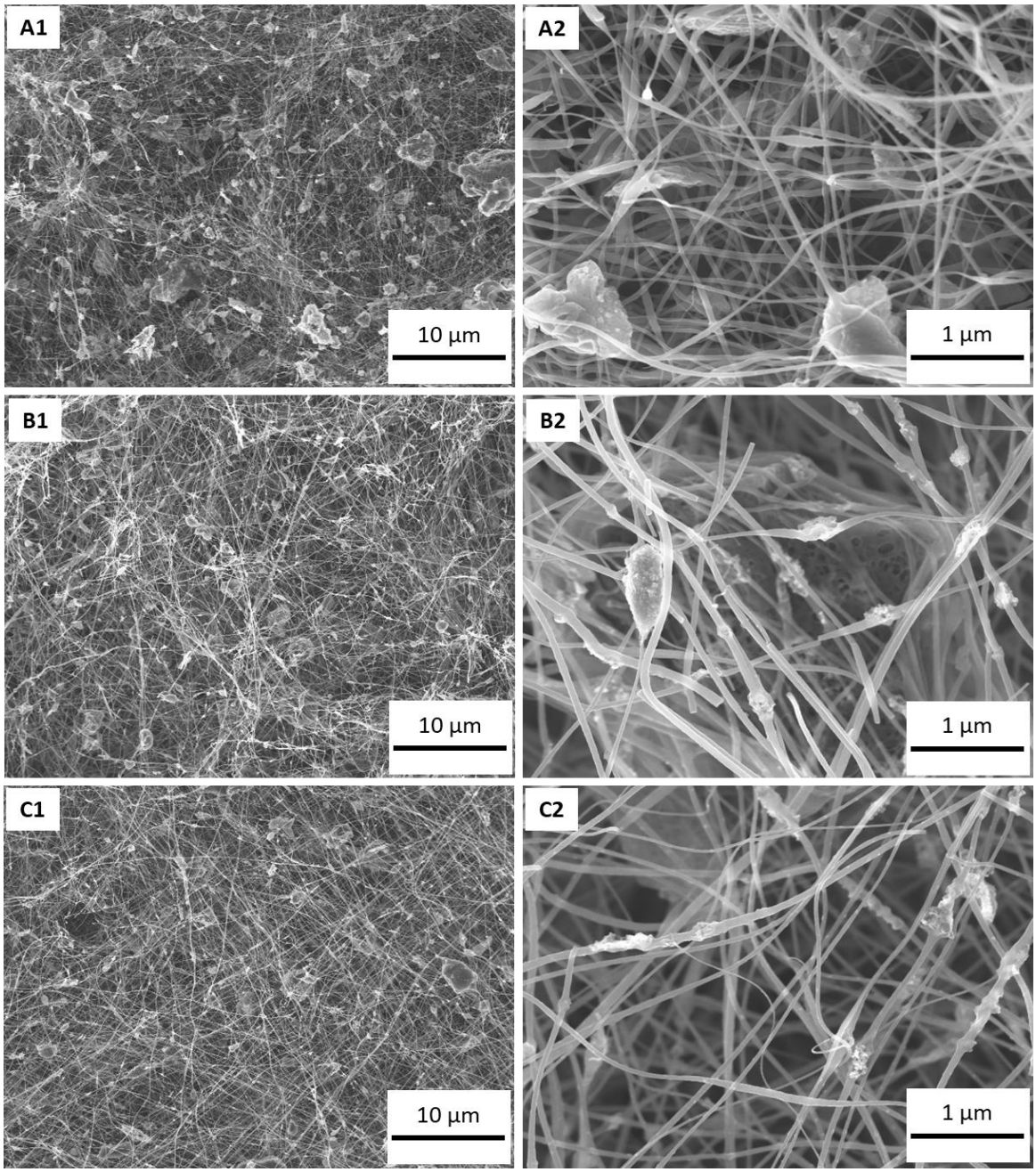

Fig. 3. SEM of electrospun carbon nanofibers (ECNFs) from electrospinning PAN and biochar bicomponent solutions: A1 and A2) ECNF from PAN and raw biochar BCK0; B1 and B2) ECNF from PAN and BCK2; C1 and C2) ECNF from PAN and BCK3

The porous structure and size distribution of PAN/Biochar derived ECNFs were analyzed by BET measurement. It was evident that incorporation of biochar particles into electrospun PAN nanofibers led to larger BET SSA and larger pore volume than the PAN alone ECNFs (Table 3). The larger SSA allowed an efficient contact of nanofibers with electrolyte, which is beneficial for electronic and ionic transport. As shown in Table 3, the PAN derived ECNFs has the lowest specific surface areas of 11 m^2/g, while the

PAN/Biochar derived ECNFs exhibited much higher SSA than the PAN derived ECNFs, with the highest SSA of 505 m^2/g from the PAN/BCK2 ECNFs. It's believed that the high porosity of the activated carbon is attributed to the significant change of the SSA and pore volume of the resultant ECNFs.

Table 3 The specific surface area (SSA), volume, pore size and average diameter of PAN/Biochar Derived ECNFs

Sample	BET SSA (m^2g^{-1})	Average Pore Size (nm)	Pore Volume (cm^3g^{-1})	Average Fiber Diameter (nm)
PAN ECNF	11	8.6	0.024	300
PAN/BCK0 ECNF	97.37	7.23	0.18	56.36 ± 6.93
PAN/BCK2 ECNF	505.92	2.49	0.31	95.17 ± 18.61
PAN/BCK3 ECNF	381.11	2.77	0.26	99.71 ± 16.35

3.4. Electrochemical performance

The electrochemical capacitive performance of the PAN/Biochar derived ECNFs were evaluated by cyclic voltammetry and galvanostatic charge/discharge measurement. Typical CV curves of the ECNFs electrode were collected at a scan rate between 5–100 mV/s within a potential window from −0.4 to 0.4 V in 6 M KOH aqueous electrolyte. Fig. 4 (a) shows the cyclic voltammetry loops of PAN derived and different PAN/Biochar derived ECNFs at scan rate of 100 mv/s. At a scan rate of 100 mV/s, CV curve of the PAN derived ECNF exhibited a long and narrow non-rectangular shape and enclosed a very small loop area, suggesting very small electrochemical double layer capacitive behavior. This result can be attributed to the low conductivity and hydrophobicity of the PAN derived ECNF [16]. CV curves of PAN/Biochar derived ECNFs exhibited Quasi-rectangular shape and enclosed much larger loop area, indicating these biochar incorporated ECNFs have higher gravimetric capacitance and would be more desired electrode materials for the supercapacitor. Among the four ECNFs, the PAN/BCK13 ECNF has the CV curve with the largest loop area, suggesting the highest gravimetric capacitance. The sample of ECNF PAN/BCK3 was further scanned at varied scan rate of 5-100 mV/s (Fig. 4b). With the increase of voltage sweep rate, the CV curves well maintain the quasi-rectangular shape with little distortion, indicating a reversible supercapacitor behavior in organic electrolyte within the potential range. This can be attributed to the excellent conductivity and low mass-transport resistance of the samples.

The charge and discharge curves of different ECNF electrodes were obtained at constant current density of 0.5 A/g with potential window from -0.4 to 0.4 V in 6 M KOH aqueous electrolyte (Fig. 4c). The charge/discharge curves of these ECNFs were approximately isosceles, indicating excellent capacitive performance such as great electrochemical stability and reversibility [22]. The galvanostatic charge/discharge behavior of PAN/BCK3 ECNFs was further investigated at various current densities of 1 A/g and 2 A/g (Fig. 4d). The charge and discharge curves were almost linear and the isosceles triangles indicated excellent supercapacitor behaviors.

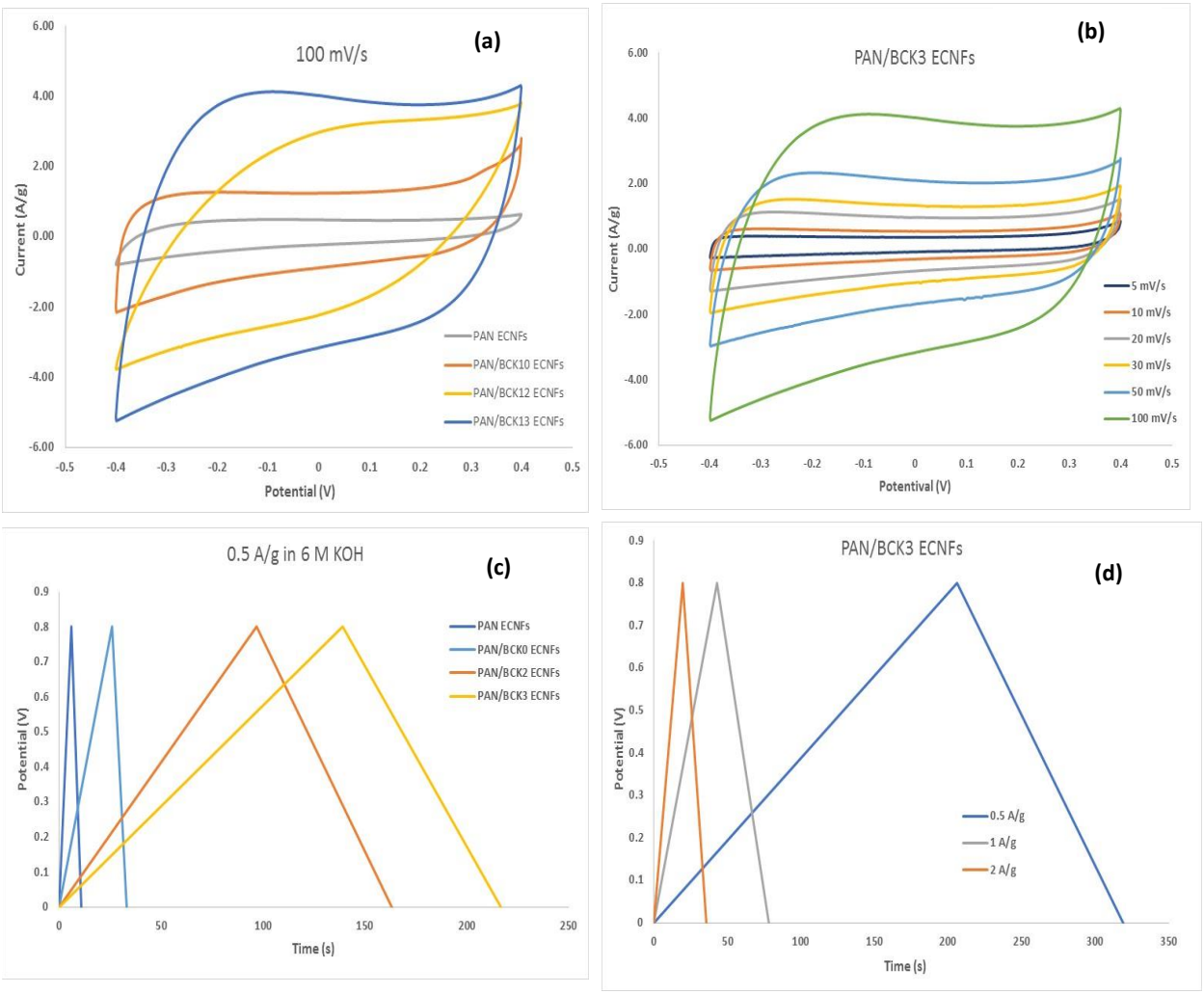

Fig. 4. Electrochemical characterization of different Biochar-based ECNF electrodes in 6 M KOH aqueous electrolyte: (a) Cyclic voltammetry loops at scan rate of 100 mv/s; (b) Cyclic voltammetry loops of PAN/BCK3 ECNFs at different voltage sweeping rates; (c) Galvanostatic charge/discharge curves at the current density of 0.5 A/g; and (d) Galvanostatic charge/discharge curves of PAN/BCK3 ECNFs at different current densities.

The gravimetric capacitance of PAN/BCK0, PAN/BCK2, PAN/BCK3 ECNFs electrodes at the current density of 0.5 A/g were 32, 87, and 108 F/g, respectively. With the increase of KOH ratio in the chemical activation of biochar, the decrease in average pore size and increase in of the SSA can be contributed to the increase of the gravimetric capacitance. The gravimetric capacitances of PAN/BCK3 ECNFs at 0.5, 1, and 2 A/g were 108, 88, and 80 F/g respectively. As the current density increased, the corresponding capacitance reduced slightly. It was observed that ~78% of the initial capacitance was retained at a relatively large current density of 2 A/g when PAN/BCK3 ECNFs was used as the electrode. It is worth noting that the capacitance of PAN/BCK3 ECNFs is substantially higher than the most recent reported values for using freestanding ENCFs as electrode materials for supercapacitor, such as ECNF/MnO_2 (83.3 F/g) [23], HTL Biochar/PAN ECNFs (37.6 F/g), and lignin-derived ECNFs (64 F/g) [15]. This

suggests that the ECNFs made from activated biochar might be innovative carbon nanomaterials for energy storage applications.

Long term cycling performance is a crucial parameter for electrode material of supercapacitor. The stability of capacitance performance of PAN/BCK3 ECNFs was investigated through galvanostatic/charge/discharge test for 1,000 cycles within a potential window from -0.4 V to 0.4 V at high current density of 1 A/g (Fig. 5a). The gravimetric capacitance was merely reduced by 4% after 1,000 cycles of charge and discharge, indicating that the PAN/BCK3 ECNFs is electrochemical stable and durable.

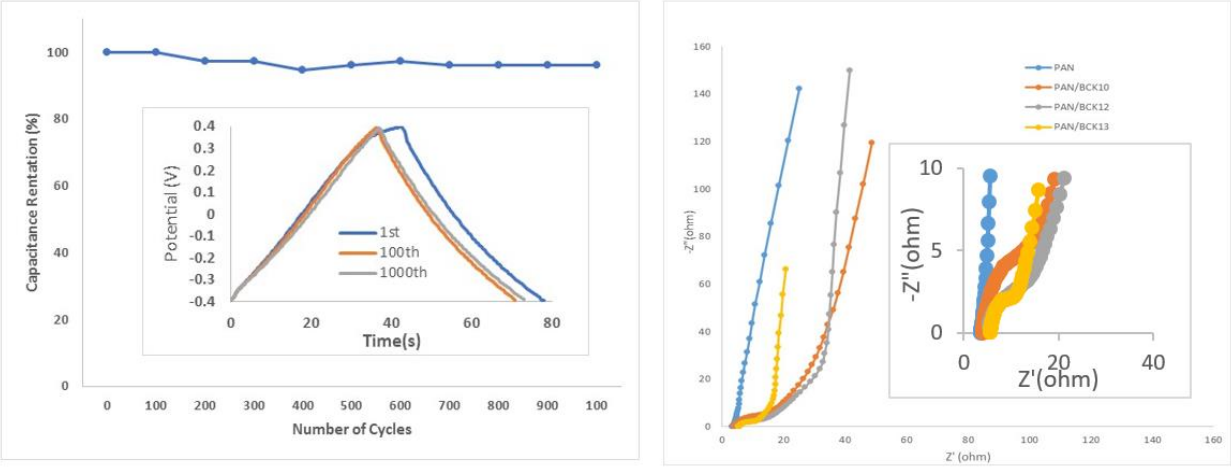

Fig. 5. a) Cycling stability of PAN/BCK3 ECNFs electrode material under current density of 1 A/g with embedded charge/discharge curves of 1st, 100th, and 1000th cycles; b) Nyquist plots of different biochar based ECNF electrodes

To further investigate the electrochemical behavior of ECNFs electrodes, electrochemical impedance spectroscopy (EIS) was carried out as shown in Fig. 5(b). EIS is a powerful technique to obtain the information on both the characteristics of pores and the dynamic ion diffusion in porous electrodes. For biochar based ECNFs, the impedance spectra included a distorted semicircle in the high frequency regime and a liner part nearly vertical to the realistic impedance axis at the low frequency regime. No evident semicircle corresponding to charge transfer resistance was found for PAN alone ECNFs. In the high frequency range, the plot intersection at real part Z' is associated with the electrolyte resistance (R_S) and the square resistance of the samples. The semicircle region in the plot curve corresponds to the charge transfer resistance (R_{ct}), which represents the migration rate of ions at the interface between the solution and the electrode surface.

The diameters of the semicircles are listed in the following order: PAN/BCK0>PAN/BCK1>PAN/BCK3. The smaller diameter of semicircle in the EIS spectrum of PAN/BCK3 ECNFs indicates lower charge transfer resistance. In the low frequency region, the line has finite slope representing the diffusive resistivity of the electrolyte within the pore of the electrode, as represented by Warburg impedance. The slope of PAN/BCK3 ECNFs approached to an ideally straight line implying outstanding capacitive performance thanks to the enhanced accessibility of the ions [16]. All these results revealed that the PAN/BCK3 ECNFs have the lowest internal resistance and the

best ion transition and diffusion among all three bio-char based ECNFs, in good agreement with the CV curves and specific galvanostatic plots.

CONCLUSIONS

Highly flexible porous biochar based ECNFs were fabricated by electrospinning technique and explored as electrode material. It was found that KOH plays an important role on the creation of porous structures. The increase of KOH loading amount in the activation process would lead to the increase of specific surface area of the activated char as well as the ECNFs after fabrication. The biochar based ECNFs not only showed a large SSA, but also exhibited high flexibility and an improved conductivity. As designed, the biochar based ECNFs showed high specific capacitance, high cycle stability and excellent electrochemical performance. This research illustrates that this biochar based ECNF is a promising electrode material for high performance supercapacitor.

ACKNOWLEDGMENTS

The authors thank USDA-CSREES-Evans-Allen Project (NCX-303-5-17-130-1) for the financial support.

CONFLICTS OF INTEREST

The authors declare that there is no conflict of interests regarding the publication of this paper.

REFERENCES

[1] Wang, K., Xu, M., Gu, Z., Ahrenkiel, P., Lee, J., Gibbons, W., Croat, J., and Fan, Q. (2016). Pyrrole modified biomass derived hierarchical porous carbon as high performance symmetrical supercapacitor electrodes. *International Journal of Hydrogen Energy*, 41(30), 13109-13115. DOI: 10.1016/j.ijhydene.2016.05.090

[2] Jin, H., Wang, X., Shen, Y., and Gu, Z. (2014). A high-performance carbon derived from corn stover via microwave and slow pyrolysis for supercapacitors. *Journal of Analytical and Applied Pyrolysis*, 110, 18-23. DOI: 10.1016/j.jaap.2014.07.010

[3] Dyatkin, B., Presser, V., Heon, M., Lukatskaya, M. R., Beidaghi, M., and Gogotsi, Y. (2013). Development of a Green Supercapacitor Composed Entirely of Environmentally Friendly Materials. *ChemSusChem*, 6(12), 2269-2280. DOI: 10.1002/cssc.201300852

[4] Qiu, Z., Wang, Y., Bi, X., Zhou, T., Zhou, J., Zhao, J., Miao, Z., Yi, W., Fu, P., and Zhuo, S. (2018). Biochar-based carbons with hierarchical micro-meso-macro porosity for high rate and long cycle life supercapacitors. *Journal of Power Sources*, 376, 82-90. DOI: 10.1016/j.jpowsour.2017.11.077

[5] Liu, M.-C., Kong, L.-B., Zhang, P., Luo, Y.-C., and Kang, L. (2012). Porous wood carbon monolith for high-performance supercapacitors. *Electrochimica Acta*, 60, 443-448. DOI: 10.1016/j.electacta.2011.11.100

[6] Cheng, B.-H., Zeng, R. J., and Jiang, H. (2017). Recent developments of post-modification of biochar for electrochemical energy storage. *Bioresource Technology*, 246, 224-233. DOI: 10.1016/j.biortech.2017.07.060

[7] Gao, F., Shao, G., Qu, J., Lv, S., Li, Y., and Wu, M. (2015). Tailoring of porous and nitrogen-rich carbons derived from hydrochar for high-performance supercapacitor electrodes. *Electrochimica Acta*, 155, 201-208. DOI: 10.1016/j.electacta.2014.12.069

[8] Zhang, L. L., and Zhao, X. S. (2009). Carbon-based materials as supercapacitor electrodes. *Chemical Society Reviews*, 38(9), 2520-2531. DOI: 10.1039/B813846J

[9] Xiu, S., Shahbazi, A., and Li, R. (2017). Characterization, Modification and Application of Biochar for Energy Storage and Catalysis: A Review. *Trends in Renewable Energy*, 3(1), 86-101. DOI: 10.17737/tre.2017.3.1.0033

[10] Zhang, S., Su, Y., Zhu, S., Zhang, H., and Zhang, Q. (2018). Effects of pretreatment and FeCl3 preload of rice husk on synthesis of magnetic carbon composites by pyrolysis for supercapacitor application. *Journal of Analytical and Applied Pyrolysis*, 135, 22-31. DOI: 10.1016/j.jaap.2018.09.026

[11] Li, W., Chen, D., Li, Z., Shi, Y., Wan, Y., Wang, G., Jiang, Z., and Zhao, D. (2007). Nitrogen-containing carbon spheres with very large uniform mesopores: The superior electrode materials for EDLC in organic electrolyte. *Carbon*, 45(9), 1757-1763. DOI: 10.1016/j.carbon.2007.05.004

[12] Aboagye, A., Liu, Y., Ryan, J. G., Wei, J., and Zhang, L. (2018). Hierarchical carbon composite nanofibrous electrode material for high-performance aqueous supercapacitors. *Materials Chemistry and Physics*, 214, 557-563. DOI: 10.1016/j.matchemphys.2018.05.009

[13] Duan, P., and Savage, P. E. (2011). Hydrothermal Liquefaction of a Microalga with Heterogeneous Catalysts. *Industrial & Engineering Chemistry Research*, 50(1), 52-61. DOI: 10.1021/ie100758s

[14] Du, X., Zhao, W., Wang, Y., Wang, C., Chen, M., Qi, T., Hua, C., and Ma, M. (2013). Preparation of activated carbon hollow fibers from ramie at low temperature for electric double-layer capacitor applications. *Bioresource Technology*, 149, 31-37. DOI: 10.1016/j.biortech.2013.09.026

[15] Lai, C., Zhou, Z., Zhang, L., Wang, X., Zhou, Q., Zhao, Y., Wang, Y., Wu, X.-F., Zhu, Z., and Fong, H. (2014). Free-standing and mechanically flexible mats consisting of electrospun carbon nanofibers made from a natural product of alkali lignin as binder-free electrodes for high-performance supercapacitors. *Journal of Power Sources*, 247, 134-141. DOI: 10.1016/j.jpowsour.2013.08.082

[16] Liu, Y., Zhou, J., Chen, L., Zhang, P., Fu, W., Zhao, H., Ma, Y., Pan, X., Zhang, Z., Han, W., and Xie, E. (2015). Highly Flexible Freestanding Porous Carbon Nanofibers for Electrodes Materials of High-Performance All-Carbon Supercapacitors. *ACS Applied Materials & Interfaces*, 7(42), 23515-23520. DOI: 10.1021/acsami.5b06107

[17] Sevilla, M., Yu, L., Zhao, L., Ania, C., and Titiricic, M.-M. (2014). Surface Modification of CNTs with N-Doped Carbon: An Effective Way of Enhancing Their Performance in Supercapacitors. *ACS Sustainable Chem. Eng.*, 2 (4), 1049–1055. DOI: 10.1021/sc500069h

[18] Cheng, Y., Lu, S., Zhang, H., Varanasi, C. V., and Liu, J. (2012). Synergistic Effects from Graphene and Carbon Nanotubes Enable Flexible and Robust Electrodes for High-Performance Supercapacitors. *Nano Letters*, 12(8), 4206-4211. DOI: 10.1021/nl301804c

[19] Hao, J., Zhong, Y., Liao, Y., Shu, D., Kang, Z., Zou, X., He, C., and Guo, S. (2015). Face-to-face self-assembly graphene/MnO2 nanocomposites for supercapacitor applications using electrochemically exfoliated graphene. *Electrochimica Acta*, 167, 412-420. DOI: 10.1016/j.electacta.2015.03.098

[20] Li, R., Shahbazi, A., Wang, L., Zhang, B., Chung, C.-C., Dayton, D., and Yan, Q. (2018). Nanostructured molybdenum carbide on biochar for CO2 reforming of CH4. *Fuel*, 225, 403-410. DOI: 10.1016/j.fuel.2018.03.179

[21] Wang, J., and Kaskel, S. (2012). KOH activation of carbon-based materials for energy storage. *Journal of Materials Chemistry*, 22(45), 23710-23725. DOI: 10.1039/C2JM34066F

[22] Razaq, A., Nyholm, L., Sjödin, M., Strømme, M., and Mihranyan, A. (2012). Paper-based energy-storage devices comprising carbon fiber-reinforced polypyrrole-cladophora nanocellulose Composite electrodes. *Advanced Energy Materials*, 2(4), 445-454. DOI: 10.1002/aenm.201100713

[23] Ma, X., Kolla, P., Zhao, Y., Smirnova, A. L., and Fong, H. (2016). Electrospun lignin-derived carbon nanofiber mats surface-decorated with MnO2 nanowhiskers as binder-free supercapacitor electrodes with high performance. *Journal of Power Sources*, 325, 541-548. DOI: 10.1016/j.jpowsour.2016.06.073

Trends in Renewable Energy
OPEN ACCESS ISSN: 2376-2144
Peer-Reviewed Article futureenergysp.com/index.php/tre

Green Refining of Waste Lubricating Oil: A China Perspective

Jinlong Wu[1], Bo Li[1], Wei Wang[1], Shu Yang[1], Peng Liu[1], Bo Zhang[1,*], Changyan Yang[1,2,*], Yigang Ding[1]

1: Key Laboratory for Green Chemical Process of Ministry of Education, Hubei Key Laboratory of Novel Chemical Reactor and Green Chemical Technology, School of Chemical Engineering and Pharmacy, Wuhan Institute of Technology, Hubei, China
2: Hubei Key Laboratory for Processing and Application of Catalytic Materials, Huanggang Normal University, Hubei, China

Received January 5, 2019; Accepted April 3, 2019; Published April 25, 2019

Presently, many regeneration processes of waste lubricating oil, such as catalytic hydrogenation, are available. However, some of these processes are highly costly and not suitable for Chinese economic conditions, and some may produce contaminated impurities such as acid slag, which cannot meet environmental protection requirements. This study aims to develop a green process for the regeneration of waste lubricating oil into a base oil, which should meet the requirements of green chemistry, have the characteristics of simple operation, low cost, less pollution and high recovery rate, and turn wastes into renewable resources. The new process developed via this research has three stages. First, mechanical and large particle impurities in the waste lubricating oil were removed by pretreatment. Second, most of the colloid and asphaltene were removed by thermal extraction and sedimentation. Finally, the activated bleaching earth was used to further purify the waste lubricating oil. The performance evaluation of the finally obtained lubricating base oil conformed to the standard of the HVI-100 lubricating oil. The total recovery rate of the process was about 63.5%.

Keywords: Waste lubricating oil; Green refining; Pretreatment; Thermal extraction and sedimentation; Response surface methodology

1. Introduction

1.1 Overview

The development of the lubricant industry is directly linked to the development of the transportation industry and has a greater impact on the ups and downs of the macro economy. From 2000 to 2010, along with the rapid development of China's economy, the scale of the lubricant market has continued to grow rapidly. In 2010, the consumption of lubricating oil reached 8.5-8.8 million tons/year [1]. Since 2013, China's economic development has entered a steady growth phase. Many industries including the lubricant industry have been affected and showed a gradual slowdown in development. The lubricant industry in China has been continuously eliminating outdated products and switching to high-end products with the extended oil-changing period.

In 2017, the domestic demand for automotive lubricants was 3.572 million tons, accounting for 53% of the total lubricant market, and the share of industrial ones was reduced to 28% [2]. Lubricant or motor oil is a consumer product for all vehicles, which

Corresponding author: bzhang_wh@foxmail.com, ychy1969@163.com

Tr Ren Energy, 2019, Vol. 5, No.2, 165-180. doi: 10.17737/tre.2019.5.2.0084

needs to be replaced every 5000-7000 km or 3000-5000 miles. Correspondingly, the amount of waste lubricating oil produced in China is proportional to this market demand (Figure 1) [3].

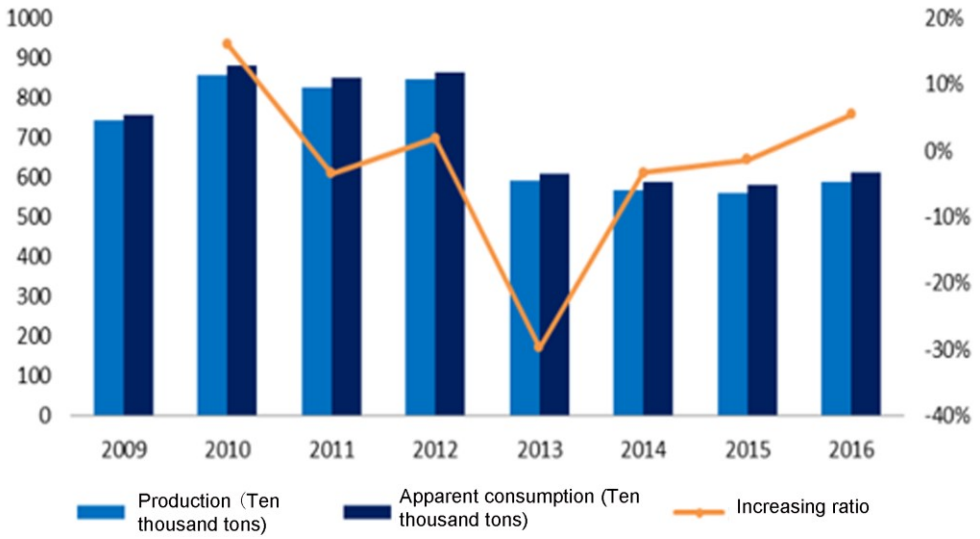

Figure 1. Lubricant production and apparent consumption (Adapted from http://www.chyxx.com/industry/201708/555496.html, Public Domain)

During the use, some hydrocarbons in the lubricating oil will react with oxygen at high temperature and pressure to produce peroxides, carboxylic acids, alcohols, ketones, asphaltenes, gums, etc. The color of the oil becomes darker [4]. The produced acids cause the increased acidity of the lubricating oil, which can corrode easily the mechanical parts, resulting in the reduced service life. Meanwhile, incomplete combustion in the engine produces carbon residue, and mutual friction between mechanical parts tends to generate minute metal powder particles. Dust, moisture, and soil in the environment are also components of impurities in the lubricating oil. These impurities may form deposits on the surface of mechanical parts, which are liable to cause engine blockage and reduce its service life [5]. When the metamorphic portion reaches 5-10%, the lubricating oil must be disposed of as waste lubricating oil.

Waste lubricating oil is mainly composed of base oil, asphaltene, colloids, oxides, carbon residue, sludge, moisture, and other components [6]. The main oxides in waste lubricating oils are carboxylic acids, carboxylates, and aldehydes [7]. Metals such as Ni, Sn, Cr, and Fe are produced by corrosion of the engine, while metals like Ag, B, Ba, Ca, Cd, Co, Hg, Mg, Mo, P, Pb, Sb, Se, Ti, Zn, etc. are derived from the additives [8]. Waste lubricating oil is mainly processed in the following ways [9-12]:

(1) Directly discarded as wastes;
(2) Catalytic cracking;
(3) Used as a fuel after removing heavy metals;
(4) Raw materials for road oiling;
(5) Regeneration into a lubricating base oil

Among them, the regeneration of waste lubricating oil into a base oil has better economics and reflects the concept of green chemistry. As early as the beginning of the 20th century, the recycling process of waste lubricating oil was commercialized on a large scale in the United States and Germany. China has carried out research on the

regeneration process of waste lubricating oil since the 1940s. So far, most of China's manufacturers are still using the sulfuric acid-bleaching earth process, which was mainly used in the early 1960s by other countries. Currently, petroleum has become an increasingly important resource, and environmental protection became an unavoidable issue. Many countries have raised the standard for the recycling of waste lubricating oil and issued the policies to encourage the recycling.

1.2 Regeneration Processes of Waste Lubricating Oil

1.2.1 Sulfuric Acid - Bleaching Earth Process

The sulfuric acid-bleaching earth process (Figure 2) utilizes the principle that properties of oil and water are incompatible, and the boiling point of water is lower than that of waste oil. [13, 14]. The water is first removed by heating. Then, concentrated sulfuric acid is used to oxidize organic matters, which is removed by washing with alkali. The active bleaching earth absorbs impurities such as pigments. Final filtration could remove solid residues.

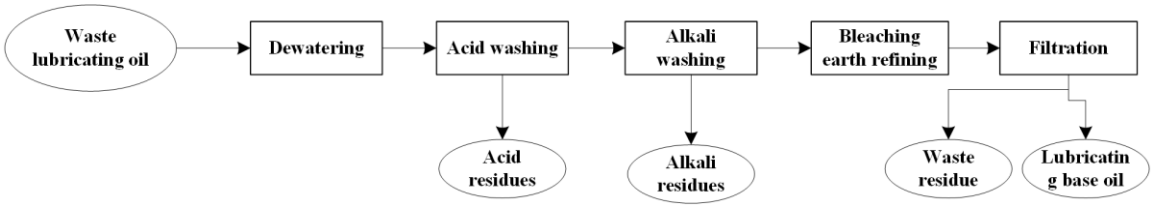

Figure 2. Sulfuric acid- bleaching earth process

1.2.2 Hydrotreating

The hydrotreating process has advantages including the high oil yield, simple operation and well-established process, but its cost is relatively high [15]. It is widely used abroad. Under certain conditions of catalysis and pressure, impurity elements such as N, O, S, etc. in the waste oil are removed as their hydrides such as NH_3, H_2O, H_2S, etc [16]. The olefin and aromatic hydrocarbons can be partially hydrogenated to improve the quality of the oil.

1.2.3 Molecular Distillation

The mass transfer and heat transfer of the device for molecular distillation is very efficient, and the material requirements are relatively demanding. It is necessary to remove the pollutants such as mechanical impurities in the waste lubricating oil before further purification (Figure 3). The quality of the lubricating oil obtained by the molecular distillation process [4, 17] satisfies the national standard of the lubricating base oil. But the distillation process has higher requirements on the environment and requires a higher degree of vacuum. The size of the reactor is fixed and has certain limitations.

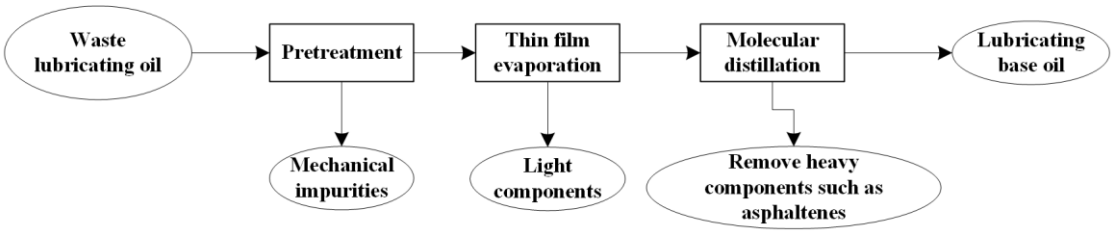

Figure 3. Molecular distillation process

1.2.4 Solvent Refining

Solvent refining is one of the commonly used methods for refining petroleum products. Figure 4 shows the solvent refining process flow chart. It utilizes different solubility of components of the lubricating oil in a solvent to remove impurities and non-ideal component [18, 19].

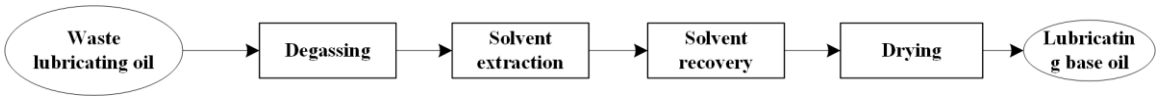

Figure 4. Solvent refining process

The degassing process removes oxygen dissolved in the oil to prevent the solvent from being slowly oxidized. After solvent extraction, two layers are formed. The lower layer is a mixture of solvent and impurities, and the upper layer mainly contains refined oil. The energy consumption of the solvent recovery part accounts for 80% of the process. The solvent in the upper layer is removed in the evaporation stripper, and then dewatered to obtain the lubricating base oil.

1.2.4 Membrane Separation

Recently, membrane separation process [20] has been proposed as new mean to regenerate waste lubricating oil. Because of its high cost, related studies remain at the research stage. Figure 5 is a flow chart of the membrane separation process.

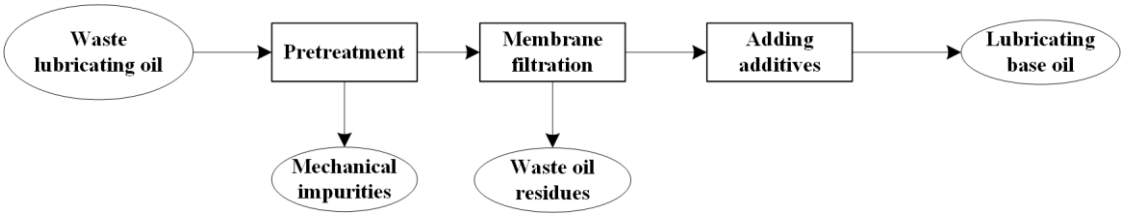

Figure 5. Membrane separation process

1.3 The Choice of Waste Lubricating Oil Regeneration Process in China

The hydrofining process is used by many developed countries for waste lubricant treatment. However, the investment in hydrotreating process is relatively high. For the time being, there is no waste lubricating oil recycling plant in China that uses hydrotreating process.

The problems with the solvent refining process are the loss of the solvent, the low base oil yield, and the high sulfur content of the base oil product. At present, the solvent formulation has been improved, and the consumption of the solvent has been significantly reduced. Compared with the hydrofining process, the investment cost of the solvent refining plant is lower, and the technology is more mature.

The sulfuric acid-bleaching earth process is mature and requires relatively low investment cost. Many domestic refineries are using this method. However, the residual acid slag and alkali slag have a great impact on the environment. With the gradual strict environmental policy in China, the process will gradually be eliminated by the market.

2. Materials and Methods

2.1 Materials

The waste lubricating oil used in this study was provided by Tianan Chemical Co., Ltd (Macheng, Hubei Province, China). The color of the waste lubricating oil is carbon black, which is very thick at room temperature, and has an unpleasant pungent odor. Its properties are listed in Table 1.

Table 1. Performance evaluation results of the waste lubricating oil

Property	Value	Method
Viscosity (mPa·s)/40℃	78.50	LVDV-1 viscometer
Acid value (mg·KOH/g)	0.59	GB/T264-1983
Moisture (%)	0.55	GB/T260-2016
Mechanical impurity (%)	1.42	GB/T511-2010
Ash (%)	0.57	GB/T508-1985

The chemical reagents of isopropanol, n-butanol, isobutanol, and butanone were purchased from Sinopharm Chemical Reagent Co., Ltd (Shanghai, China).

Table 2. Properties and prices of alcohol and ketone solvents*

Solvent	Isopropanol	n-butanol	Isobutanol	Butanone
Boiling point (℃)	82.5	117.7	108.1	75.9
Freezing point (℃)	-88.5	-90.2	-108.0	-85.9
Price (¥ YMB/ton)	7800	7600	7400	7500

*All solvents listed in Table 2 have intermediate toxicity and stable at room temperature.

The activated bleaching earth (also called activated clay) was provided by Zhengzhou Fengquan Water Treatment Plant (Henan, China). The physical and chemical properties of the products are shown in Table 3.

Table 3. Physical properties and composition of the activated bleaching earth

Property	Index	Composition	Weight %
Appearance	White fine powder	SiO_2	62.34
Surface area	＞130m^2/g	Al_2O_3	17.24
Moisture	＜5%	Fe_2O_3	2.73
Decolorization	＞154	FeO	0.12
Heavy metal content	＜10mg/kg	TiO	0.15
Arsenic content	＜3mg/kg	CaO	2.09
Free acid	＜0.1%	MgO	5.44
Granularity (<0.076mm)	＞95%	MnO	0.15

The activated bleaching earth was dried in an oven at 110°C for 2 hours prior to the experiments.

2.2 Characterization of Lubricating Oil

Viscosity was measured by using the LVDV-1 rotary electronic viscometer (Shanghai Jingtian Electronic Instrument Co., Ltd, China). The acid value was measured by the indicator titration method according to the national standard GB/T264-1983. The moisture content of the oil was measured by the distillation method according to the national standard GB/T260-2016, while the ash content was determined according to the national standard GB/T508-85.

Mechanical impurities in the oil refer to solid small particles that cannot be dissolved in a solvent such as toluene or gasoline. To measure mechanical impurities, the oil was first dissolved in the toluene, which was followed by filtration (GB/T511-2010).

Color of the oil (*i.e,* chromaticity) could reflect the degree of refinement and its stability. A lighter oil color generally indicates a higher degree of purification of the waste lubricating oil [21]. The color of the recycled oil was determined according to ASTM D1500-12. The sample oil and standard swatches are placed under a certain light source, and the color is compared to determine the ASTM color of the oil.

2.3 Thermal Settlement

Thermal settling is used as a pretreatment method, which is an effective physical method of removing the mechanical impurity from a large volume of waste lubricating oil, which has the advantages of low energy consumption and easy handling. For each test, about 60 ml of waste lubricating oil was added to a 100 ml beaker, which was placed into an oven at 40-80 °C for 3-24 h. The mechanical impurity content was measured after each test.

2.4 Thermal Extraction and Sedimentation

Solvents such as short-chain alcohols and ketones have poor dissolving ability for substances with relatively high molecular weight such as asphaltenes, colloids, gray matter and additives, but strong dissolving ability for oil components. Heating can reduce the viscosity of the waste lubricating oil, making the extraction process more complete. Therefore, high molecular weight substances settle down during thermal extraction and sedimentation. Commonly used extractants are polar solvents such as C3 or C4 alcohols and butanone, which showed good solubility to the waste lubricating base oil [22, 23].

Considering the cost, solvents of isopropanol, n-butanol, isobutanol, and butanone were used for comparison.

2.5 Response Surface Methodology for Thermal Extraction and Sedimentation using Double Solvents

To further analyze the effect of using two extraction solvents on thermal extraction flocculation, the response surface methodology was used to design the experiments (Table 4).

Table 4. Box-Behnken response surface test design factors and levels

Level	A: solvent to oil	B: solvent ratio	C: Temperature (℃)
-1	2:1	1:4	30
0	4:1	2.13:1	50
1	6:1	4:1	70

The yield of waste lubricating oil is the response value, and three factors of A, B, and C are the ratio of solvent to oil (A: the volume ratio of the extractant: mass of crude lubricating oil), the solvent ratio (B: the volume ratio of n-butanol: isobutanol), and temperature (C), respectively. This three-factor three-level response surface analysis included 17 extraction experiments. Each extraction experiment was performed for 45 min, and then the solvent was distilled under reduced pressure at 70°C.

2.6 Bleaching with Activated Bleaching Earth

A certain amount of waste lubricating oil after extraction and sedimentation was accurately weighed into a three-necked flask. A relatively excess amount of activated bleaching earth was added to determine the effect of temperature on the degree of refining. After finding the optimum temperature, the amount of activated bleaching earth was adjusted to select the best proportion of activated clay. The stirring speed was fixed at 300 rpm, and the stirring time was fixed at 30 min. After the stirring, the upper layer solution in the three-necked flask was placed in a beaker that was placed in a constant temperature drying oven at 70°C for 6-8 hours. The final upper yellow liquid was the purified waste lubricating base oil.

The most intuitive color of waste lubricating oil is used as the evaluation standard. According to ASTM D1500-12, the final result is represented by the color code (*i.e.,* chromaticity) of 0.5-8. When the color of the oil exceeds 8 or more, it is necessary to add kerosene and then measure. This experiment simplifies the measurement method and treats it with 8 when the chromaticity exceeds 8. The smaller the number, the lighter the color of the oil and the higher the degree of refining, and vice versa.

3. Results and Discussion

3.1 Pretreatment with Thermal Settlement

The contents of the mechanical impurities of the waste lubricating oil after thermal settling are shown in Figure 6. As the settling time increased, the five curves gradually become flat. After 24-h, it can be regarded as a horizontal line. Therefore, 24-h was considered as the optimal settling time.

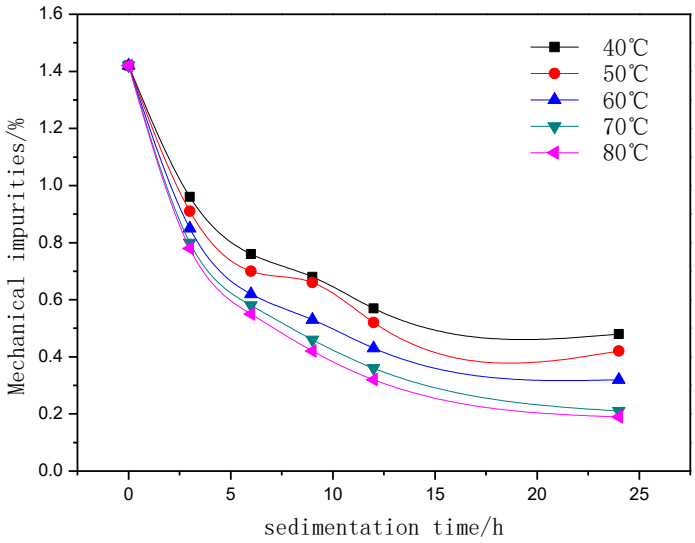

Figure 6. The effects of thermal settling temperature and time

The increase in the pretreatment temperature can significantly reduce the amount of mechanical impurities in the waste lubricating oil. At 70°C and 80°C, the change of mechanical impurity content in waste lubricating oil was small. Because a higher temperature can increase the cost and the oxidative deterioration of oil, 70°C was considered as the optimal settling temperature. Subsequent tests used the waste lubricating oil after thermal settling at 70°C as experimental materials.

3.2 Thermal Extraction and Sedimentation using Single Solvent

Four solvents of isopropanol, n-butanol, isobutanol, and butanone were tested. The solvent was mixed with the waste lubricating oil in the ratio of 1:1, 2:1, 3:1, 4:1, and 6:1, and then heated at 50°C for 30 min. The yield of waste lubricating oil was measured after purification. It was found that butanone had no obvious extraction effect and was basically miscible with lubricating oil. Figure 7 shows the relationship between the solvent to oil ratio and the yield of the recycled waste lubricating oil. When the ratio was higher than 3:1, there is no obvious yield change.

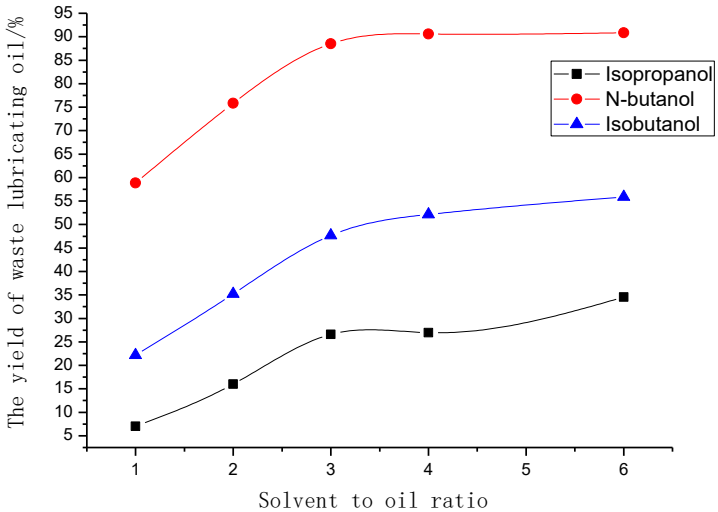

Figure 7. Effect of single solvent extraction on the yield of recovered lubricating oil

3.3 Thermal Extraction and Sedimentation using Double Solvents

The selection of two solvents in the thermal extraction and sedimentation tests was based on the conclusions of single-solvent extraction. N-butanol has a strong ability to dissolve effective components of the waste lubricating oil, and isobutanol can reduce the ash content. Therefore, a combination of n-butanol and isobutanol was selected as the extractant.

Table 5. Analysis of variance of regression equation

Source of variance	sum of squares	Degree of freedom	Mean squares	F value	P value*	Significance
Model	4928.83	9	555.84	32.77	<0.0001	significant
A	3262.30	1	3262.30	195.22	<0.0001	significant
B	425.01	1	425.01	25.43	0.0015	significant
C	31.13	1	31.13	1.86	0.2146	
AB	48.30	1	48.30	2.89	0.1329	
AC	59.99	1	59.99	3.59	0.1000	
BC	45.77	1	45.77	2.74	0.1419	
A^2	323.95	1	323.95	19.39	0.0031	significant
B^2	188.81	1	188.81	11.30	0.0121	significant
C^2	436.26	1	436.26	26.11	0.0014	significant
Residual	116.97	7	16.71			
Lack of Fit	86.04	3	28.68	3.71	0.1190	Not significant
Pure error	30.94	4	7.73			
Cor. total	5045.81	16				
		R^2=0.9768	R_{ADJ}^2=0.9470			

* The cut-off value for P value was 0.05.

The results are shown in Figure 8. The multivariate quadratic regression fitting was performed, and the regression model of the process parameters was established. The coded regression equation for the specific yield Y is:

$$Y(\%)=82.95+20.19\times A+7.29\times B+1.97\times C-3.48\times A\times B-3.87\times A\times C-3.38\times B\times C-8.77\times A^2-6.70\times B^2-10.18\times C^2 \quad \text{(Equation 1)}$$

A, B, and C, respectively, correspond to the coding values of the three factors, and the values are in the range of -1 to 1. Therefore, the regression equation can be used instead of the test real point to calculate the experimental results.

The larger the F value of the dependent variable, the greater the effect on the yield of the waste lubricating oil. It can be seen from Table 5 that the solvent to oil ratio (A) has the greatest influence on the yield of the waste lubricating oil, and the solvent ratio (B) has the second influence on the waste lubricating oil yield, and the temperature C has the least influence on the waste lubricating oil yield.

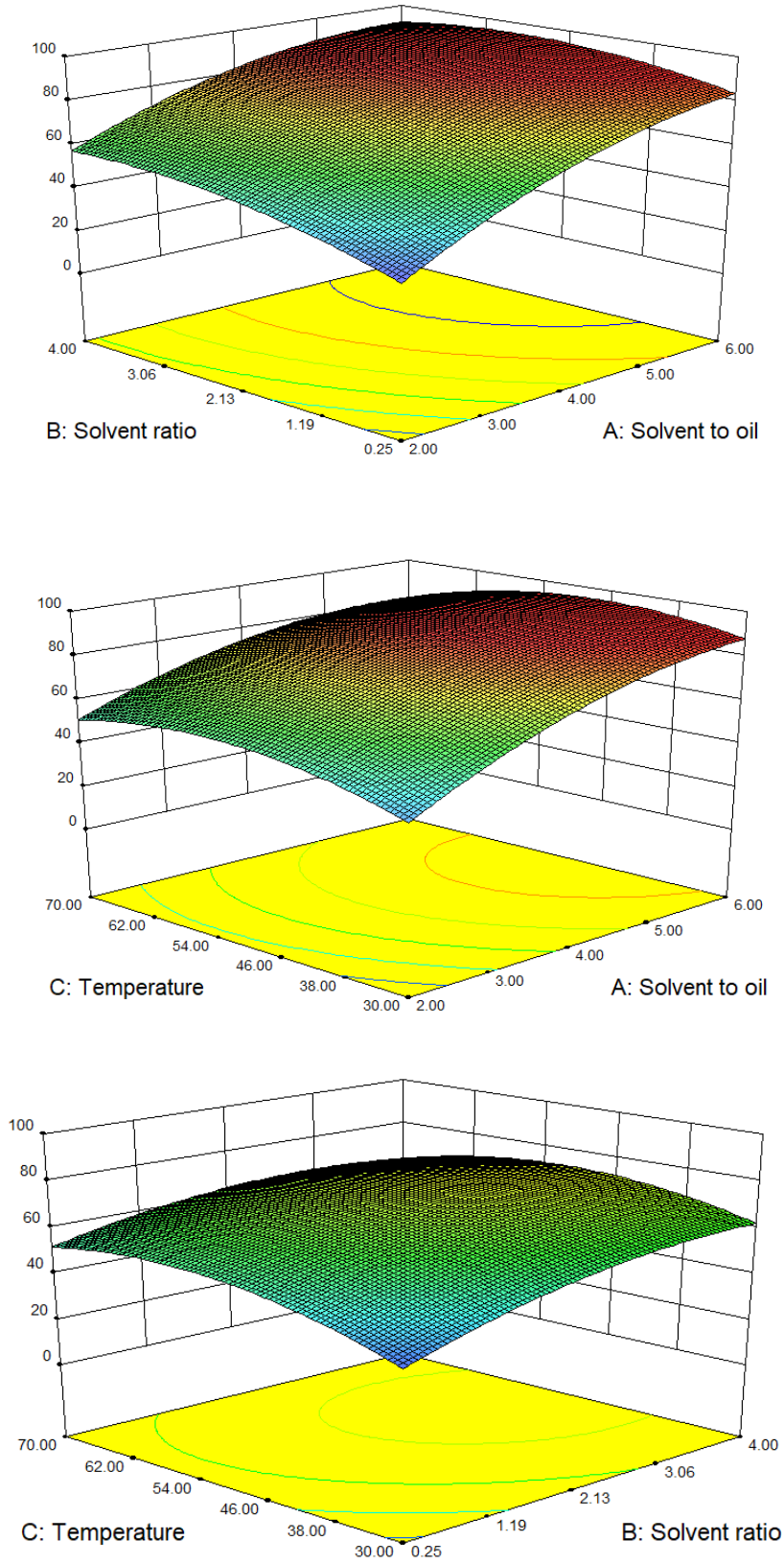

Figure 8. 3D response surface map of the thermal extraction and sedimentation using double solvents

Table 6. Simulated optimal values for the two solvents

Number	Solvent:Oil	Solvent ratio	Temperature /℃	Yield/%	Desirability	
1	6	2.7	47.09	95.1234	0.364	Selected
2	6	2.7	46.99	95.1227	0.364	
3	6	2.7	47.94	95.1227	0.364	
4	6	2.7	47.29	95.1222	0.364	
5	6	2.7	46.85	94.1213	0.364	

Based on Equation 1, the optimal conditions were calculated (Table 6). The optimal conditions were the ratio of solvent: waste lubricating oil of 6:1, n-butanol: isobutanol (vol ratio) of 2.7:1, temperature of 47.1℃, and stirring time of 45 min.

Table 7. Verification of the optimal conditions for the two solvents

Number	Solvent:Oil	Solvent ratio	Temperature /℃	Yield /%
1	6	2.7	47.1	91.56
2	6	2.7	47.1	89.65

The optimal conditions were further experimentally verified. The yield of the waste lubricating oil product obtained under the above conditions was 90.60 ± 1.35%, and the viscosity at 40°C was 50.2 mPa·s, and the ash content was 0.23%. Intuitively, the appearance color is lighter than the single extractant n-butanol as a solvent but still reddish brown. The acid value was 0.1 mg·KOH/g.

Compared with the single extractant n-butanol, the yield of the recovered waste lubricating oil of the double-solvent extraction was slightly increased and the ash content decreased. In this test, the ratio of the solvent to the lubricating oil has the greatest influence, the solvent ratio has the secondary influence on the yield of the waste lubricating oil, and the temperature has the least effect. The optimal conditions experimentally verified were close to the simulated values, indicating that the method has certain persuasive power, and there are certain rules for each factor and response value.

3.4 Bleaching with Activated Bleaching Earth

The waste lubricating oil treated with thermal extraction and sedimentation was further purified by using activated bleaching earth. As shown in Figure 9, when the temperature was below 110°C, the chromaticity of the waste lubricating oil did not change too much, and the activated bleaching earth obtained was dark yellow and did not play an adsorption role. When the bleaching temperature rose to 120°C, the situation changed significantly, and the chromaticity of the waste lubricating oil dropped sharply. The bleaching earth obtained at this time was dark brown, and the colored materials in the oil were basically taken out. When the temperature was raised to 130 ° C, the oil is

already clear. Therefore, the choice of 125°C for the bleaching temperature, not only can get better oil, but also reduce heat and save costs.

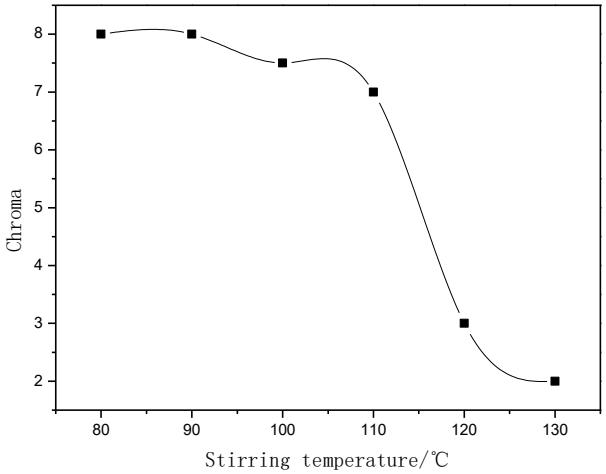

Figure 9. Relationship between temperature and oil color under excessive bleaching earth

After determining the bleaching temperature to be 125°C, the relationship between the amount of bleaching earth added (% of white soil quality: oil quality) and the color and the recovery rate of the final base oil were determined (Figure 10).

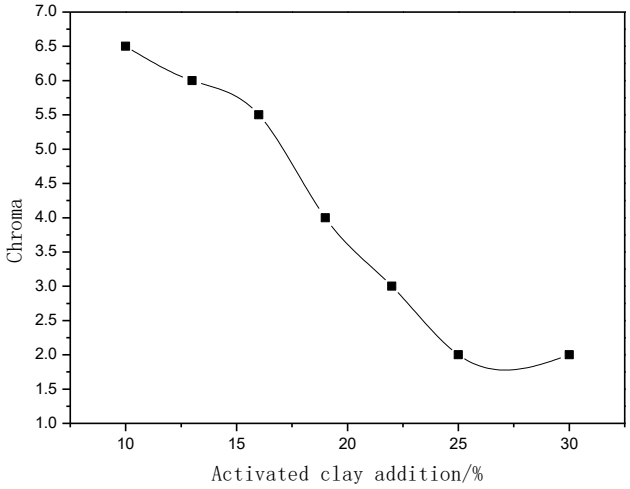

Figure 10. Effect of the amount of activated bleaching earth on the chromaticity

There is a strong correlation between the amount of activated bleaching earth and the degree of refining of the oil. As the amount of activated bleaching earth increased, the color of the waste lubricating oil gradually decreased. When the amount of activated bleaching earth reached 25%, the color of lubricating oil was basically unchanged and became a relatively pure yellow transparent liquid. Figure 11 shows the change of appearance chromaticity of the waste lubricating oil with the addition of activated bleaching earth.

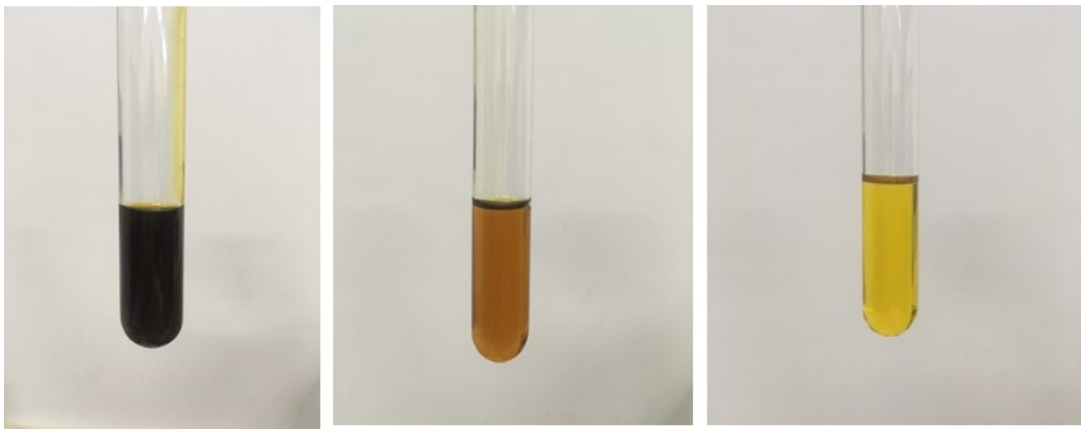

Figure 11. Appearance chromaticity change of waste lubricating oil
Left: the waste lubricating oil after thermal extraction and sedimentation; Middle: Treated with 15 wt% of activated bleaching earth; Right: Treated with 25 wt% of activated bleaching earth

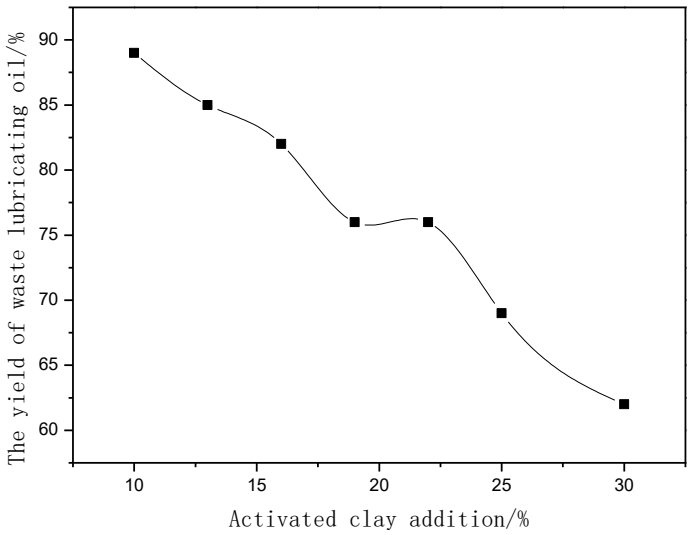

Figure 12. Effect of the amount of activated bleaching earth on the yield of waste lubricating oil

As can be seen from Figure 12, as the amount of activated bleaching earth increased, the yield of waste lubricating oil has been decreasing. On the one hand, too much bleaching earth will absorb a part of the oil, resulting in a decrease in the amount of recycled oil. On the other hand, due to the rise of the bleaching earth, the bleaching earth in the oil is difficult to settle in the process of the final thermal settling, and the separation speed is slow, resulting in oil turbidity and lowering the yield of the base oil.

In summary, in order to achieve a better purification effect, the amount of bleaching earth added was 25 wt%, and the yield of refined lubricating oil was 69%.

Table 8. Properties of recycled lubricating oil

Properties	Value
Dynamic viscosity@40℃ (mPa•s)	24.0
Kinematic viscosity@40℃ (mm^2/s)	21.8
Viscosity index	98.2
Acid value (mg•KOH/g)	0.04
Moisture (%)	0
Mechanical impurities (%)	0
Ash content (%)	0.02
Pour point (℃)	-14

Table 9. HVI-100 Lubricant Standard

Kinematic viscosity @40℃ (mm^2/s)	Appearance	Chromaticity	Viscosity index	Pour point (℃)	Acid value (mg•KOH/g)	Ash content (%)
20~22	Transparent	1	100	<-9	<0.02	<1.5

Comparing Table 8 with Tables 9, it is found that the finally obtained lubricating oil sample basically conforms to the standard of the grade HVI-100 lubricating oil.

4. CONCLUSIONS

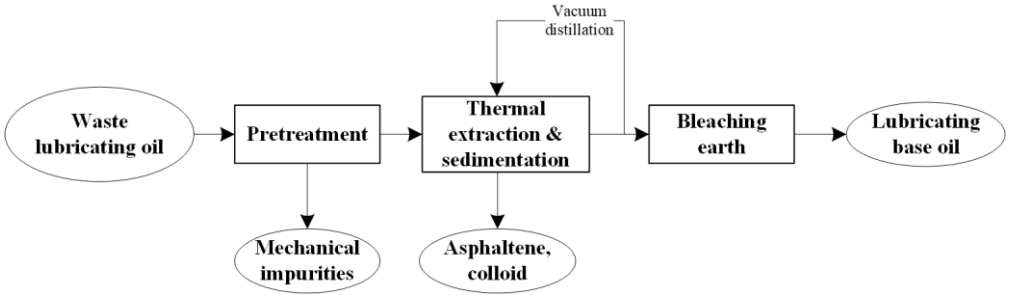

Figure 13. Green refining process of waste lubricating oil developed in this study

This paper proposes a new process for the regeneration of waste lubricating oil into lubricating base oil (Figure 13). The process has three stages. The first pretreatment stage removes mechanical impurities and large particulate matter from the waste lubricating oil via thermal settling. By comparing the effects of different temperatures and settling times on mechanical impurities, a reasonable settling time of 24 h and an optimum settling temperature of 70°C were found. The second stage is a thermal extraction and sedimentation process to remove impurities such as asphaltenes and gums. The thermal extraction and sedimentation process was carried out using a single solvent of isopropanol, n-butanol or isobutanol. It was found that the most economical ratio of the ratio of the solvent to oil was 3:1, the stirring time was 30 min, and the operation temperature was around 50°C. When using double solvents of n-butanol and isobutanol, the optimal conditions were the solvent to oil ratio of 6:1, the solvent ratio of 2.71:1, and the temperature of 47.1 °C. Under these conditions, the yield of the oil experimentally

obtained was 90.60±1.35%. The third stage is bleaching with the activated bleaching earth, which adsorbs the pigments and the impurities such as colloid and asphaltene. The optimal temperature was determined as 125°C when the mass of bleaching earth was 25 wt% of the oil mass. The refined lubricating oil is basically in accordance with the standard of the HVI-100 lubricating base oil. The total recovery rate of the process was about 63.5%.

ACKNOWLEDGMENTS

This work is partially supported by Graduate Innovative Fund of Wuhan Institute of Technology (NO: CX2017129 and CX2018019) and the School of Chemical Engineering and Pharmacy at the Wuhan Institute of Technology.

CONFLICTS OF INTEREST

The authors declare that there is no conflict of interests regarding the publication of this paper.

REFERENCES

[1] An, J. (2017). Global lubricant market analysis and development forecast. *Petroleum Products Application Research*(3), 4-9.

[2] Wang, Q., Tao, C., and Yang, N. (2017). Automotive lubrication efficiency and long oil change period. *Lubricating Oil*(1), 1-6.

[3] Gao, X., and Tang, W. (2002). Replacing and Inspecting of Lubricant for Engine of Automobile. *Shandong Metallurgy*(4), 69-70.

[4] Speight, J. G. (2014). *The chemistry and technology of petroleum*, CRC press.

[5] Thom, R., Kollmann, K., Warnecke, W., and Frend, M. (1995). Extended oil drain intervals: Conservation of resources or reduction of engine life. *SAE transactions*, 706-718.

[6] Li, Y., Wu, J., Jiang, G., Wu, H., Huai, Y., and Zhao, W. (2016). Progresses in regeneration technologies for used lube oils. *Petrochemical Technology*(2), 244-250.

[7] Liu, J., Zhang, Z., Gao, W., Lei, Y., and Bai, J. (2004). Technique for regenerating waste lubricating oil. CN1539936A.

[8] Liu, J. (2012). Solvent Extraction of Waste Gasoline Engine Oil-Flocculation Composite Regeneration Technology. China Academy of Machinery Science and Technology

[9] Whisman, M. L., Reynolds, J. W., Goetzinger, J. W., and Cotton, F. O. (1978). Process for preparing lubricating oil from used waste lubricating oil. Google Patents.

[10] Durrani, H. A., Panhwar, M. I., and Kazi, R. A. (2011). Re-Refining of waste lubricating oil by solvent extraction. *Mehran University Research Journal of Eng. & Tech*, 30(2), 237-246.

[11] Hsu, Y.-L., and Liu, C.-C. (2011). Evaluation and selection of regeneration of waste lubricating oil technology. *Environmental monitoring and assessment*, 176(1-4), 197-212.
[12] Lam, S. S., Liew, R. K., Jusoh, A., Chong, C. T., Ani, F. N., and Chase, H. A. (2016). Progress in waste oil to sustainable energy, with emphasis on pyrolysis techniques. *Renewable and Sustainable Energy Reviews*, 53, 741-753.
[13] Ackerman, A. H. (1929). Process for treating mineral oils. U.S. Patent No. 1,742,020.
[14] Audibert, F. (2006). *Waste engine oils: rerefining and energy recovery*, Elsevier, Amsterdam. DOI: 10.1016/B978-0-444-52202-3.X5018-8
[15] Zhang, B., Wu, J., Yang, C., Qiu, Q., Yan, Q., Li, R., Wang, B., Wu, J., and Ding, Y. (2018). Recent Developments in Commercial Processes for Refining Bio-Feedstocks to Renewable Diesel. *BioEnergy Research*, 11(3), 689-702. DOI: 10.1007/s12155-018-9927-y
[16] Zhang, B., and Seddon, D. (2018). *Hydroprocessing Catalysts and Processes: The Challenges for Biofuels Production*, World Scientific Publishing, Singapore. DOI: 10.1142/q0141
[17] Iwao, Y., Yamamoto, S., and Kunihiro, T. (1979). Method of preparing base stocks for lubricating oil. U.S. Patent 4,157,294.
[18] Manley, R. E., Mccarty, B. Y., and Gross, H. H. (1938). Solvent refining process. U.S. Patent 2,121,323.
[19] Sequeira Jr, A., Smith Jr, B. F., and Mead, T. C. (1981). Solvent refining process. U.S. Patent 4,294,689
[20] Gould, R. M., White, L. S., and Wildemuth, C. R. (2001). Membrane separation in solvent lube dewaxing. *Environmental Progress*, 20(1), 12-16. DOI: 10.1002/ep.670200110
[21] Lu, Y., Yang, J., and Wang, L. (2016). Study on Coloring Substances of Refined Lubricating Oil. *Acta Petrolei Sinica*, 32(1), 132-142.
[22] Alves dos Reis, M. (1991). Waste lubricating oil rerefining by extraction-flocculation. 3. A pilot plant study. *Industrial & Engineering Chemistry Research*, 30(11), 2449-2456.
[23] Mohammed, R. R., Ibrahim, I. A., Taha, A. H., and McKay, G. (2013). Waste lubricating oil treatment by extraction and adsorption. *Chemical Engineering Journal*, 220, 343-351.

Trends in Renewable Energy
OPEN ACCESS ISSN: 2376-2144
Peer-Reviewed Article futureenergysp.com/index.php/tre

Enhancing the Statistical Hybrid Model Performance in Overhead and Underground Medium Voltage Broadband over Power Lines Channels by Adopting Empirical Channel Attenuation Statistical Distribution

Athanasios G. Lazaropoulos*

School of Electrical and Computer Engineering / National Technical University of Athens / 9 Iroon Polytechniou Street / Zografou, GR 15780

Received April 09, 2019; Accepted May 19, 2019; Published May 29, 2019

Statistical hybrid model is a statistical channel model suitable for the broadband over power lines (BPL) networks while it is based on the statistical processing of channel attenuation and capacity values of preassumed BPL topology classes. One of the key operation elements of the statistical hybrid model, which affects its results fidelity, is the selection of the appropriate channel attenuation statistical distribution among a set of well-known channel attenuation statistical distributions (i.e., such as Gaussian, Lognormal, Wald, Weibull and Gumbel distributions). The selection of the appropriate channel attenuation statistical distribution becomes a hard task since it depends on a number of factors such as the power grid type –either overhead (OV) or underground (UN) power grid–, the representative distribution BPL topology of the examined class, the applied electromagnetic interference (EMI) policies and the used coupling scheme type. The contribution of this paper is to identify the conditions whether the Empirical channel attenuation statistical distribution can act as the default distribution of statistical hybrid model (modified statistical hybrid model) thus replacing the required comparison analysis prior to the selection of the aforementioned distributions of the initial statistical hybrid model. The evaluation comparison is based on the already applied metrics of capacity percentage change and average absolute capacity percentage change.

Keywords: Smart Grid; Broadband over Power Lines (BPL) networks; Power Line Communications (PLC); Distribution Power Grids; Capacity; Statistics; Modeling

1. Introduction

Living in the era of Internet of Things, we are witnessing an ever increasing number of devices with ubiquitous intelligence, which are interconnected via embedded systems and networks, that can communicate with humans and other devices changing our lives [1]. Under the auspices of the smart grid, further interoperability between electrical and electronic equipment can be delivered for the Internet of Things and, thus, new tremendous opportunities concerning the supported broadband applications of power utilities can be achieved [2]-[4]. Among the available communications solutions that have

**Corresponding author:* AGLazaropoulos@gmail.com

Tr Ren Energy, 2019, Vol.5, No.2, 181-217. doi: 10.17737/tre.2019.5.2.0096

been proposed and are used across the smart grid, Broadband over Power Lines (BPL) technology can play an important role, since it may support an electronic communications channel (*i.e.*, BPL channel) upon the already installed wired power grid infrastructure without adding extra complexity and cost in contrast with other communications solutions of the smart grid [4]-[16].

The initial statistical hybrid model that deals with the transmission and distribution BPL channel modeling through a statistical point of view has been demonstrated in [5], [6]. The core of the initial statistical hybrid model remains the deterministic well-validated hybrid model that has extensively been employed to examine the behavior of various multiconductor transmission line (MTL) configurations in transmission and distribution BPL networks [12]-[22]. Through the two interconnected submodules of the hybrid model, namely: (i) the bottom-up approach module; and (ii) the top-down approach module, the hybrid model acts as an internal phase of the statistical hybrid model flowchart that delivers as output crucial broadband performance metrics such as the channel attenuation and the capacity for given BPL topology, MTL configuration, coupling scheme, electromagnetic interference (EMI) policy and noise level. Actually, the initial statistical hybrid model consists of six phases where a set of indicative distribution BPL topologies act as the representative topologies of a set of respective distribution BPL topology classes. The statistical analysis of the distribution BPL topology classes offers the capacity range of each distribution BPL topology class for given power grid type, EMI policy, noise level, coupling scheme and channel attenuation statistical distribution. Actually, each distribution BPL topology class is filled with statistically equivalent BPL topologies, which are generated by appropriately deploying a random number generator, that are characterized by the same maximum likelihood estimators (MLEs) with the representative topology of the examined class for given power grid type, coupling scheme and channel attenuation statistical distribution. In [5], [6], a number of five well-known channel attenuation statistical distributions of the communications literature, say, Gaussian, Lognormal, Wald, Weibull and Gumbel distributions, have been benchmarked since they are involved in the MLE estimation and the operation of the random number generator. In accordance with [6], Weibull and Wald channel attenuation statistical distributions perform the best capacity estimations in OV MV and UN MV power grid types regardless of the examined BPL topology class and the applied coupling scheme when EMI policies committed to the broadband character of BPL technology are adopted (e.g., FCC Part 15 of [23]). When EMI policies less protective to the BPL technology are adopted (e.g., German Reg TP NB30 and the BBC / NATO Proposal of [13], [24], [25]), a more complex situation occurs in terms of the most suitable channel attenuation statistical distribution for the capacity estimations while the number of unsuccessful estimations significantly increases in all the cases examined. In this paper, it is investigated the potential of using only one channel attenuation statistical distribution, say, the Empirical channel attenuation statistical distribution, instead of trying to identify the best channel attenuation statistical distribution by taking into consideration each time the current operation settings. In accordance with [26], [27], the Empirical channel attenuation statistical distribution, which is the distribution function associated with the Empirical measure of coupling scheme channel attenuation differences, exploits the existing coupling scheme channel attenuation data of the examined distribution BPL topology class by computing their cumulative density function (CDF) for given coupling scheme while the adoption of the self-channel attenuation statistical distribution affects the flowchart of the statistical

hybrid model in the MLE computation module (Phase C of the statistical hybrid model) and the random number generator module (Phase D of the statistical hybrid model). In this paper, the initial hybrid statistical model performance after the adoption of the Empirical channel attenuation statistical distribution, which is hereafter denoted as modified statistical hybrid model, is compared against the best case of the scenarios presented in [6] that deal with the initial statistical hybrid model. The performance metrics are going to be used for the benchmark are the percentage capacity change and absolute percentage capacity change.

The rest of this paper is organized as follows: In Section II, the OV MV and UN MV MTL configurations with the indicative BPL topology classes are presented. Section III summarizes the basics of the statistical hybrid model as well as the required flowchart changes for the adoption of the Empirical channel attenuation statistical distribution. In Section IV, a small briefing is given regarding the required operation settings of the initial and modified statistical hybrid model, say EMI policies, noise levels and applied coupling schemes. Section V compares the modified statistical hybrid model performance against the initial statistical hybrid model one for a number of different scenarios concerning the operation settings.

2. OV MV and UN MV MTL Configurations and BPL Topologies

In this Section, OV MV and UN MV MTL configurations, which are used in this paper, are here presented while the topological characteristics of the indicative representative OV MV and UN MV BPL topologies of the respective BPL topology classes are also reported.

2.1 OV MV and UN MV MTL Configurations

Typical cases of OV MV and UN MV distribution lines are depicted in Figs. 1(a) and 1(b) of [5], respectively. With reference to these figures, the examined OV MV distribution line consists of three parallel non-insulated phase conductors ($n^{\mathrm{OVMV}} = 3$) spaced by Δ^{OVMV} and hang at typical heights h^{OVMV} above lossy ground while the examined UN MV distribution line is the three-phase sector-type PILC distribution-class cable (8/10kV, 3×95mm^2 Cu, PILC) surrounded by the shield and the armor conductor while the whole UN MV MTL configuration is buried to 1m depth in lossy ground. Due to the common UN grounding practices, the analysis in this UN MV MTL configuration is focused only on the inner conductor set of the three phases surrounded by the shield ($n^{\mathrm{UNMV}} = 3$). The exact dimensions of the OV MV and UN MV MTL configurations are given in [17] as well the applied grounding practices and the impact of the considered lossy ground on BPL signal propagation.

2.2 Indicative OV MV and UN MV BPL Topologies of Respective Topology Classes

With reference to Fig. 2 of [5], BPL networks are divided into cascaded BPL topologies. Each BPL topology is bounded by the transmitting and receiving end repeaters while different number of branches $k,\ k = 1, \cdots, N$, distribution cable lengths $L_k,\ k = 1, \cdots, N+1$ and branch lengths $L_{\mathrm{b}k},\ k = 1, \cdots, N$ are encountered across the

BPL signal transmission path. In accordance with [12]-[18], hybrid model treats each BPL topology separately as cascaded network modules.

With reference to Fig. 2 of [5], five indicative OV MV and UN MV BPL topologies are reported in Table 1 and 2, respectively. These indicative distribution

Table 1
Indicative OV MV BPL Topologies and Respective BPL Topology Classes [5], [28]

Topology Number (OV MV *l*)	**Indicative BPL Topology Name**	**BPL Topology Class Description**	**Number of Branches**	**Length of Distribution Lines**	**Length of Branching Lines**
OV MV 1	Urban case A	Typical OV MV BPL urban topology class	3	L_1=500m, L_2=200m, L_3=100m, L_4=200m	L_{b1}=8m, L_{b2}=13m, L_{b3}=10m
OV MV 2	Urban case B	Aggravated OV MV BPL urban topology class	5	L_1=200m, L_2=50m, L_3=100m, L_4=200m, L_5=300m, L_6=150m	L_{b1}=12m, L_{b2}=5m, L_{b3}=28m, L_{b4}=41m, L_{b5}=17m
OV MV 3	Suburban case	OV MV BPL suburban topology class	2	L_1=500m, L_2=400m, L_3=100m	L_{b1}=50m, L_{b2}=10m
OV MV 4	Rural case	OV MV BPL rural topology class	1	L_1=600m, L_2=400m	L_{b1}=300m
OV MV 5	"LOS" case	OV MV BPL Line-of-Sight transmission class	0	L_1=1000m	-

Table 2
Indicative UN MV BPL Topologies and Respective BPL Topology Classes [5], [28]

Topology Number (UN MV *l*)	**Indicative BPL Topology Name**	**BPL Topology Class Description**	**Number of Branches**	**Length of Distribution Lines**	**Length of Branching Lines**
UN MV 1	Urban case A	Typical UN MV BPL urban topology class	3	L_1=70m, L_2=55m, L_3=45m, L_4=30m	L_{b1}=12m, L_{b2}=7m, L_{b3}=21m
UN MV 2	Urban case B	Aggravated UN MV BPL urban topology class	5	L_1=40m, L_2=10m, L_3=20m, L_4=40m, L_5=60m, L_6=30m	L_{b1}=22m, L_{b2}=12m, L_{b3}=8m, L_{b4}=2m, L_{b5}=17m
UN MV 3	Suburban case	UN MV BPL suburban topology class	2	L_1=50m, L_2=100m, L_3=50m	L_{b1}=60m, L_{b2}=30m
UN MV 4	Rural case	UN MV BPL rural topology class	1	L_1=50m, L_2=150m	L_{b1}=100m
UN MV 5	"LOS" case	UN MV BPL "LOS" transmission class	0	L_1=200m	-

BPL topologies act as the representative BPL topologies of respective BPL topology classes. Note that average long end-to-end connections of 1000m and 200m are assumed for the indicative OV MV and UN MV BPL topologies, respectively.

3. Initial and Modified Statistical Hybrid Model

In this Section, the flowchart of the initial statistical hybrid model, which exploits MLEs of the five channel attenuation statistical distributions, and the phases involved are presented with respect to [5], [6]. Then, the required changes in the flowchart and the

new phases of the modified statistical hybrid model after the replacement of the five channel attenuation statistical distributions of the initial statistical hybrid model from the Empirical channel attenuation statistical distribution are defined as well as the Empirical channel attenuation statistical distribution itself.

3.1 Statistical Hybrid Model with MLEs (Initial Statistical Hybrid Model)

The initial statistical hybrid model, which exploits the five well-known channel attenuation statistical distributions (say, Gaussian, Lognormal, Wald, Weibull and Gumbel distributions), has been detailed and numerically validated in [5], [6]. In Fig. 1(a), the flowchart of the initial statistical hybrid model is given in terms of a business process model notification (BPMN) diagram.

In accordance with [5] and with respect to Fig. 1(a), the initial statistical hybrid model consists of six phases, namely: (i) *Phase A*. The hybrid model takes as inputs the distribution power grid type, the indicative distribution BPL topology, the respective distribution MTL configuration and the applied coupling scheme while it gives as output the coupling scheme channel transfer function 1×Q line vector $\mathbf{H}_{l,1}^{\mathrm{G,C}}(\mathbf{f})$ where Q is the number of flat-fading subchannels in the examined frequency range, $[\cdot]^{\mathrm{G}}$ denotes the examined distribution power grid type (i.e., OV MV or UN MV), $[\cdot]^{\mathrm{C}}$ denotes the applied coupling scheme (see Sec.3.2 of [5]), $\mathbf{f}$ is the 1×Q line vector that consists of the flat-fading subchannel start frequencies f_q, $q = 1, \ldots, Q$ and l is the topology number (see Table 1 and 2). (ii) *Phase B*. The coupling scheme channel attenuation difference module Δ of this Phase receives as input the coupling scheme channel transfer function line vector from Phase A and gives as output the coupling scheme channel attenuation difference $\Delta\mathbf{A}_{l,1}^{\mathrm{G,C}}(\mathbf{f})$ between each indicative distribution BPL topology and its respective "LOS" case for given power grid type and BPL topology class. (iii) *Phase C*. MLE computation module receives as input the coupling scheme channel attenuation difference and gives as output the MLEs for each of the five channel attenuation statistical distributions for given distribution BPL topology and coupling scheme. Note that this Phase is a synonym of the application of the five channel attenuation statistical distribution and the business process reengineering of this paper is focused on this Phase. To symbolize the existence of different MLE sets, three small vertical lines are applied to the output files of Phases C-F in Fig. 1(a). (iv) *Phase D*. The random number generator receives as input the MLEs of each channel attenuation statistical distribution and gives as output the random number 1×Q line vector $\mathbf{R}_{l,p}^{\mathrm{G,C,D}}$ for given power grid type, coupling scheme and indicative distribution BPL topology where $[\cdot]^{\mathrm{D}}$ denotes the applied channel attenuation statistical distribution, p, p=1,…,P+1 is the member number in the BPL topology class and P is the member number of each class. (v) *Phase E*. Δ^{-1} module performs the inverse procedure of Δ module of Phase B since it takes as input the random number line vector for given power grid type, coupling scheme, indicative distribution BPL topology and channel attenuation statistical distribution and gives as output the coupling scheme channel transfer function line vector $\mathbf{H}_{l,p}^{\mathrm{G,C,D}}(\mathbf{f})$ of each of the P members of each BPL topology class for given power grid type, coupling scheme and channel attenuation statistical distribution. After Phase E, each distribution BPL topology class consists of P+1 members whose coupling scheme channel transfer functions for given power grid type, coupling scheme and channel attenuation statistical distribution are considered as the output of the Phase E. (vi) *Phase F*. This Phase receives as input the coupling scheme

channel transfer functions of each distribution BPL topology class for given power grid type, coupling scheme and channel attenuation statistical distribution and gives as output

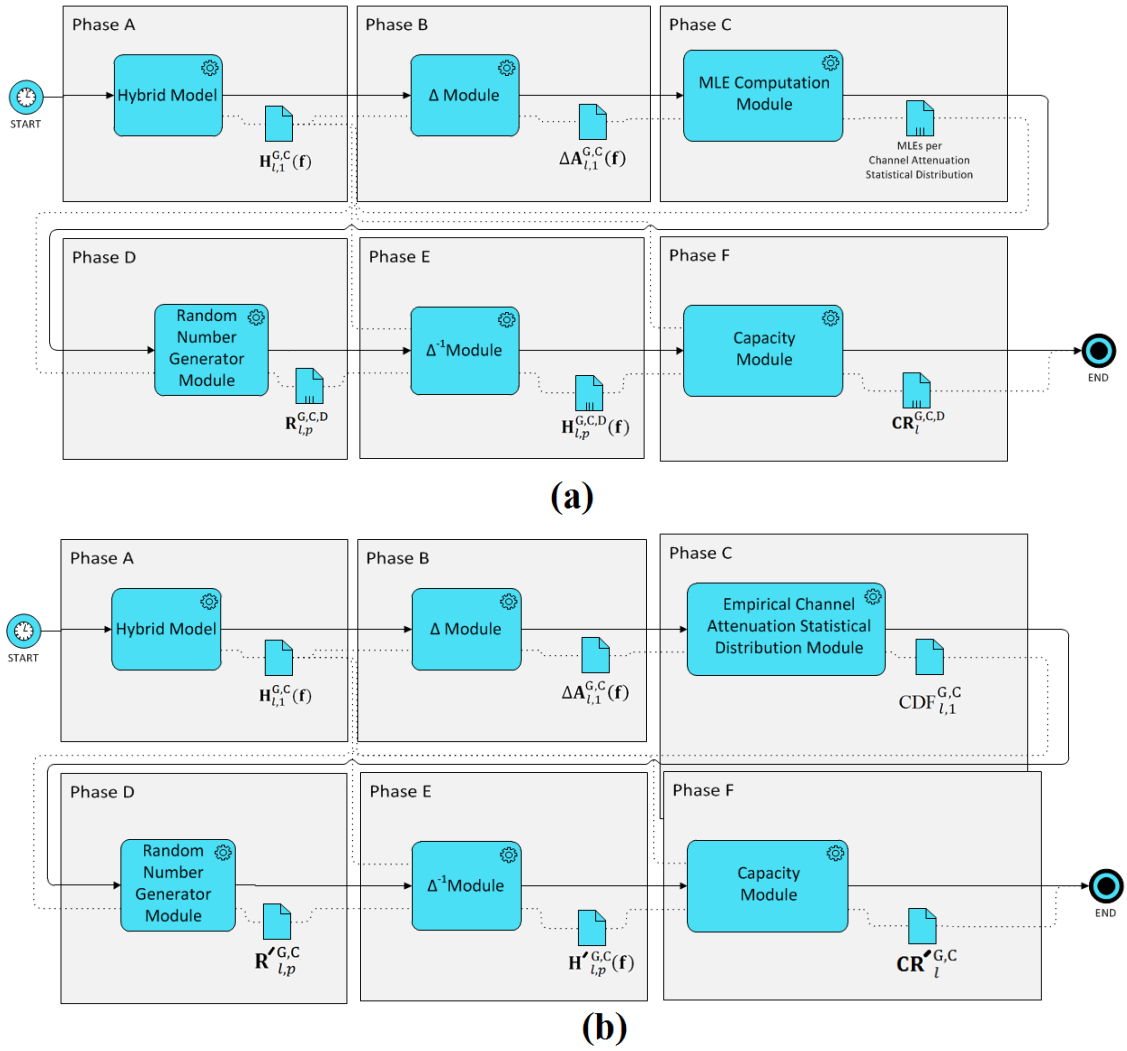

Fig. 1. Business Process Reengineering of the Statistical Hybrid Model. (a) BPMN diagram of the Initial Statistical Hybrid Model [5]. (b) BPMN diagram of the Modified Statistical Hybrid Model.

the capacity range of each distribution BPL topology class $\mathbf{CR}_{l}^{G,C,D} = [min\{\mathbf{C}_{l}^{G,C,D}\}\ average\{\mathbf{C}_{l}^{G,C,D}\}\ max\{\mathbf{C}_{l}^{G,C,D}\}]$ where $min\{\cdot\}$, $average\{\cdot\}$ and $max\{\cdot\}$ computes the minimum, the average and the maximum value of distribution BPL topology class capacity $\mathbf{C}_{l}^{G,C,D}$ that consists of all the capacities of its P+1 members.

In accordance with [6], the results of the initial statistical hybrid model are benchmarked in terms of the capacity percentage change and the average absolute capacity percentage change with respect to the applied channel attenuation statistical distribution, namely the Gaussian, Lognormal, Wald, Weibull and Gumbel distribution. A capacity estimation can be considered as successful when: (i) the capacity range of each distribution BPL topology class comprises the capacity of the respective indicative distribution BPL topology; and (ii) the average capacity value remains very close to the respective one of the indicative distribution BPL topology. In [6], it has been

demonstrated that Weibull and Wald channel attenuation statistical distributions perform the best maximum likelihood estimations in OV MV and UN MV power grid types, respectively, regardless of the examined BPL topology class and the applied coupling scheme for EMI policies of high injected power spectral density (IPSD) limits such as those of FCC Part 15 (see Sec.4.2). As the IPSD limits become lower, a mixed scenario regarding the selection of the most suitable channel attenuation statistical distribution for the capacity estimation among the BPL topology classes and power grid types occurs.

3.2 The Empirical Channel Attenuation Statistical Distribution of the Modified Statistical Hybrid Model

The insertion of the Empirical channel attenuation statistical distribution aims at bypassing the difficult task of the evaluation and the selection among the available channel attenuation statistical distributions that are based on MLEs. In Fig. 1(b), the flowchart of the modified statistical hybrid model is given in terms of a BPMN diagram thus allowing the process comparison between the initial and the modified statistical hybrid models.

By comparing Figs. 1(a) and 1(b), the following observations concerning the operation of the modified statistical hybrid model can be made, namely:

- Phases A and B remain identical between the initial and modified statistical hybrid model.
- The insertion of the Empirical channel attenuation statistical distribution mainly affects Phases C and D. More specifically, the following changes occur for the Phases C and D:
    - *Phase C*. Instead of the MLE computation module, the Empirical channel attenuation statistical distribution module is here added that receives as input the coupling scheme channel attenuation difference while it gives as output the Empirical CDF of the coupling scheme channel attenuation difference $\mathrm{CDF}_{l,1}^{G,C}$ for given distribution BPL topology and coupling scheme. Note that each coupling scheme channel attenuation difference of the indicative distribution BPL topologies is characterized by its own CDF and, for this reason, the term of Empirical channel attenuation statistical distribution is used to describe this unique statistical distribution behaviour [29].
    - *Phase D*. Conversely to the initial statistical hybrid model, the random number generator receives as input the Empirical CDF of the examined coupling scheme channel attenuation difference instead of MLEs. With reference to [26], [27], random number generator module performs an inverse interpolation to achieve CDF projection of the random values thus giving as output the random number $1\times Q$ line vector $\mathbf{R}'^{G,C}_{l,p}$ for given coupling scheme and indicative distribution BPL topology. Actually, given the MLE sets, the random number generator module of the initial statistical hybrid model computes the corresponding continuous CDF as reported in Appendix A of [5] for each of the five channel attenuation statistical distribution and then the reverse interpolation is easily applied to these continuous CDFs. In contrast, an additional interpolation for the

discrete CDF of the modified hybrid statistical model may be required if the random number is not among the available discrete CDF values.

- Phases E and F are slightly affected since these two Phases now operate with only one statistical distribution, say the Empirical channel attenuation statistical distribution, instead of the five ones of the initial statistical hybrid model.
- The output of the modified statistical hybrid model, which coincides with the output of the Phase F, is the capacity range of each distribution BPL topology class $\mathbf{CR}_l^{G,C} = [min\{\mathbf{C}_l^{G,C}\} \ \ average\{\mathbf{C}_l^{G,C}\} \ \ max\{\mathbf{C}_l^{G,C}\}]$ where distribution BPL topology class capacity $\mathbf{C}_l^{G,C}$ consists of all the capacities of its P+1 members when the Empirical channel attenuation statistical distribution is applied.

Similarly to the benchmark of the initial statistical hybrid model, the performance results of the modified statistical hybrid model are going to be investigated by the application of the metrics of capacity percentage change and average absolute capacity percentage change for the set of scenarios presented in [6]. In fact, each scenario is characterized by its own operation settings on the basis of a default operation setting set presented in Sec.4.

4. Operation Settings of Statistical Hybrid Model

In this Section, the default operation settings of the statistical hybrid model, which remain common for the initial and the modified model and constitute the baseline scenario, are presented. Also, the set of scenarios of [6], which is here deployed in order to assess the performance of the initial and modified statistical hybrid model performance comparison, is detailed as well as the respective operation settings.

4.1 Primary and Secondary Operation Settings

As already identified in [6], the distribution power grid type, the BPL topology class, the channel attenuation statistical distribution, EMI policy, noise level and applied coupling scheme are the primary factors that influence the performance of the initial statistical hybrid model. The same primary factors are also going to influence the modified statistical hybrid model performance apart from the channel attenuation statistical distributions since the Empirical channel attenuation statistical distribution is used in the latter model case to substitute them. As EMI policies, noise levels and applied coupling schemes are concerned, there is a selection of default values (see Secs.4.2, 4.3 and 4.4, respectively) that constitutes the default operation settings while the value variation of the aforementioned three primary factors constitute the different scenarios that are examined in the following numerical analysis.

Except for the primary operation settings, there is a number of secondary operation settings that are required by both the initial and the modified statistical hybrid model for their fine operation, namely:

- *Circuital parameters of the hybrid model*. To apply the hybrid model of Phase A of the statistical hybrid model, the set of circuital parameters, which is detailed in [7]-[9], [11]-[17], [19], [20], [22], [30]-[41], needs to be assumed, synoptically:
  - The identicalness of the branching and the distribution cables.
  - The full activation of the interconnections between the distribution and branch conductors.

  - The matched termination in the transmitting and receiving ends.
  - The open-circuit branch terminations.
- *Representative distribution BPL topology of each topology class*. With reference to Tables 1 and 2, the indicative OV MV and UN MV BPL topologies are assumed to be the representative ones for the respective OV MV and UN MV BPL topology classes. The OV MV and UN MV MTL configurations, which are used in this paper, are presented in Fig. 1(a) and 1(b) of [5], respectively.
- *Number of members of each distribution BPL topology class*. 100 member distribution BPL topologies (i.e., P=100) are assumed to be added in each BPL topology class of Tables 1 and 2.
- *Frequency range and flat-fading subchannel frequency spacing*. The BPL operation frequency range and the flat-fading subchannel frequency spacing are assumed to be equal to 3-30MHz and 0.1MHz (i.e, f_s =0.1MHz), respectively. Hence, there are 270 subchannels in the frequency range of interest (i.e., Q =270).
- *Negative and zero values of the coupling scheme channel attenuation differences*. During the computation of the coupling scheme channel attenuation differences in the Phase B of [5], values that are greater or equal to zero are expected in the vast majority of the cases. However, in the scarce cases of negative coupling scheme channel attenuation differences and in "LOS" cases, the coupling scheme channel attenuation differences are assumed to be equal to an arbitrarily low value, say 1×10^{-11}. Since the MLE computation of Lognormal, Wald and Weibull channel attenuation distributions comprises natural logarithms and denominators, this low value is used in order not to render the aforementioned terms infinite in the case of the initial statistical hybrid model. For comparison reasons between the initial and modified statistical hybrid model and in accordance with [5], [6], the same assumption remains valid for the modified statistical hybrid model.

4.2 EMI Policies and Default Operation Settings

BPL networks and systems operate in frequency ranges that are already occupied by other licensed communications services. Since, BPL networks and systems are, at the same time, unintentional EMI transmitters to these already licensed communications services (e.g., aeronautical radionavigation, radio astronomy, mobile satellite and maritime mobile) and EMI receivers from the aforementioned services, EMI policies that try to regulate these EMI emissions have been proposed by a number of regulation bodies. These EMI policies may correspond to respective IPSD limits $p(\cdot)$ that regulate the EMI emissions of BPL networks and systems so that BPL networks and systems do not interfere with the other already licensed communications services in the same frequency band of operation.

Among the proposals concerning EMI policies, the most noted are FCC Part 15, German Reg TP NB30 and the BBC / NATO Proposal. The electric field strength limits proposed by the above proposals are presented in [43], [44], [112] while the respective IPSD limits are determined in [13], [15], [25], [44]. During the following analysis, FCC Part 15 defines the default primary operation setting concerning EMI policy while German Reg TP NB30 and the BBC / NATO Proposal are the different scenarios concerning the EMI policy.

4.3 Noise and Default Operation Settings

In accordance with Sec. 4.3 of [5], capacity of distribution BPL networks depends on the applied MTL configuration, the examined BPL topology, the coupling scheme applied, the EMI policies adopted and the noise environment [7]-[14]. Actually, with reference to eq. (3) of [5], noise can be identified as a leading inherent BPL deficiency that critically degrades the BPL network capacities [45]. However, a typical noise scenario for capacity computations is the adoption of uniform AWGN PSD levels that can be considered as a very accurate approximation during the capacity computations as presented through FL noise model in [45], [46]. Therefore, as the default operation properties of noise properties in distribution BPL networks, -105dBm/Hz and -135dBm/Hz are the default AWGN PSD limit levels $N(\cdot)$ for OV MV and UN MV BPL networks, respectively, in the 3-30MHz frequency range are considered. Note that only default noise operation settings are assumed without other noise scenarios.

4.4 Coupling Schemes and Default Operation Settings

BPL signals are injected into and extracted from the lines of OV MV and UN MV BPL networks through different coupling schemes that are implemented by coupling scheme modules (CS modules) [11], [17], [19], [28], [47]. CS modules are integrated into the deterministic hybrid model of Phase A of the initial and modified statistical hybrid model. In accordance with [28], [47], CS2 module that is applied in this paper and remains the most recently upgraded coupling CS module for BPL networks may support three types of coupling schemes, namely: (1) *Coupling Scheme Type 1: Wire-to-Ground (WtG)* or *Shield-to-Phase (StP)* coupling schemes for OV or UN BPL networks, respectively; (2) *Coupling Scheme Type 2: Wire-to-Wire (WtW)* or *Phase-to-Phase (PtP)* coupling schemes for OV or UN BPL networks, respectively; and (3) *Coupling Scheme Type 3: MultiWire-to-MultiWire (MtM)* or *MultiPhase-to-MultiPhase (MtM)* coupling schemes for OV or UN BPL networks, respectively. Depending on the involved conductors of the examined MTL configuration and the power restrictions of [28], [47] concerning the power allocation among the involved conductors, different coupling schemes can occur for given coupling scheme type. In accordance to [6], to give a broader image of the coupling scheme selection impact, coupling scheme types 1, 2 and 3 are examined in this paper, namely:

- *Coupling Scheme Type 1*. WtG^{1} and StP^{1} coupling schemes are deployed for the assessment of OV MV and UN MV BPL topology classes, respectively.
- *Coupling Scheme Type 2*. WtW^{1-2} and PtP^{1-2} coupling schemes are deployed for the assessment of OV MV and UN MV BPL topology classes, respectively.
- *Coupling Scheme Type 3*. $\mathrm{MtM}_{0.8\ -0.1\ -0.1}^{1-2-3}$ coupling scheme is deployed for the assessment of both OV MV and UN MV BPL topology classes.

In accordance with [6], the two coupling schemes of type 1 are assumed to be the default ones while the coupling schemes of type 2 and 3 define the different coupling scheme type scenarios.

5. Numerical Results and Discussion

In this Section, numerical results concerning the performance comparison of the initial and modified statistical hybrid model are presented. Taking into account the

already identified default operation settings of Secs.4.1-4.4, the possibility of only adopting the Empirical channel attenuation statistical distribution of the modified statistical hybrid model against the five aforementioned channel attenuation statistical distributions of the initial statistical hybrid model is assessed. In fact, the comparison is based on the paper format of [6].

5.1 Initial and Modified Statistical Hybrid Model – Coupling Scheme Channel Attenuation Differences and CDFs of the Indicative OV MV and UN MV BPL Topologies for the Default Operation Settings

By comparing the flowcharts of the initial and modified statistical hybrid model of the respective Figs. 1(a) and 1(b), their main difference is located at the Phase C where MLE computation module and Empirical channel attenuation statistical distribution module are deployed for the initial and modified statistical hybrid model, respectively.

However, both modules receive as input the coupling scheme channel attenuation difference data for given indicative distribution BPL topology and coupling scheme. In Fig. 2, the coupling scheme channel attenuation difference of the indicative OV MV BPL topology of urban case A, which is reported in Table 1, is plotted versus the frequency in the 3-30MHz frequency band when WtG^1 coupling scheme, which is anyway the default coupling scheme for OV MV BPL topologies, is applied. In the same figure, the plots of the indicative OV MV BPL topologies of urban case B, suburban case and rural case, which are also reported in Table 1, are shown. It should be reminded here that the "LOS" case of Table 1 is not presented in Fig. 2 since its coupling scheme channel attenuation differences are equal to zero. Note that the plots of the indicative OV MV BPL topologies are computed with reference to the OV MV BPL "LOS" case –see eq. (5) of [5]–. In Fig. 3, same curves with Fig. 2 are demonstrated but for the case of the indicative UN MV BPL topologies of Table 2 when StP^1 coupling scheme is applied in the same operation frequency band.

Since the coupling scheme channel attenuation difference data are received by the MLE computation module and Empirical channel attenuation statistical distribution module, MLE computation module and Empirical channel attenuation statistical distribution module give as output the MLEs of the five statistical distribution and the Empirical CDF, respectively. In the case of the initial statistical hybrid model, the random number generator module of Phase D initially and internally computes CDFs of the five channel attenuation statistical distribution on the basis of the respective MLEs of Phase C. Hence, either initial or modified statistical hybrid model compute CDFs of the applied channel attenuation statistical distributions. With reference to Fig. 2, in Fig. 4(a), CDFs of the five channel attenuation statistical distributions (say, Gaussian, Lognormal, Wald, Weibull and Gumbel distributions) of the initial statistical hybrid model and of the Empirical channel attenuation statistical distribution of the modified statistical hybrid model are plotted versus the coupling scheme channel attenuation difference for the case of the OV MV BPL urban case A. In Figs. 4(b)-(d), same plots with Fig. 4(a) are given bur for the case of the OV MV BPL urban case B, suburban case and rural case, respectively. In Figs. 5(a)-(d), same curves are presented with Figs. 4(a)-(d) but for the case of the indicative UN MV BPL topologies.

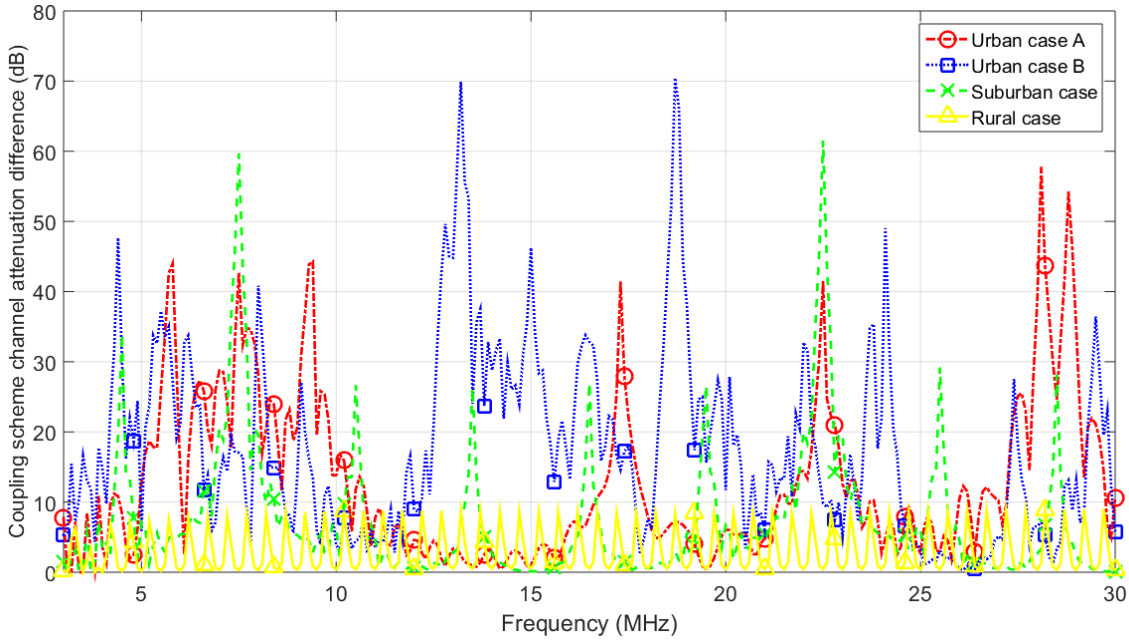

Fig. 2. Coupling scheme channel attenuation difference of the indicative OV MV BPL topologies of Table 1 in the 3-30MHz frequency band when WtG[1] coupling scheme is deployed (the subchannel frequency spacing is equal to 0.1MHz).

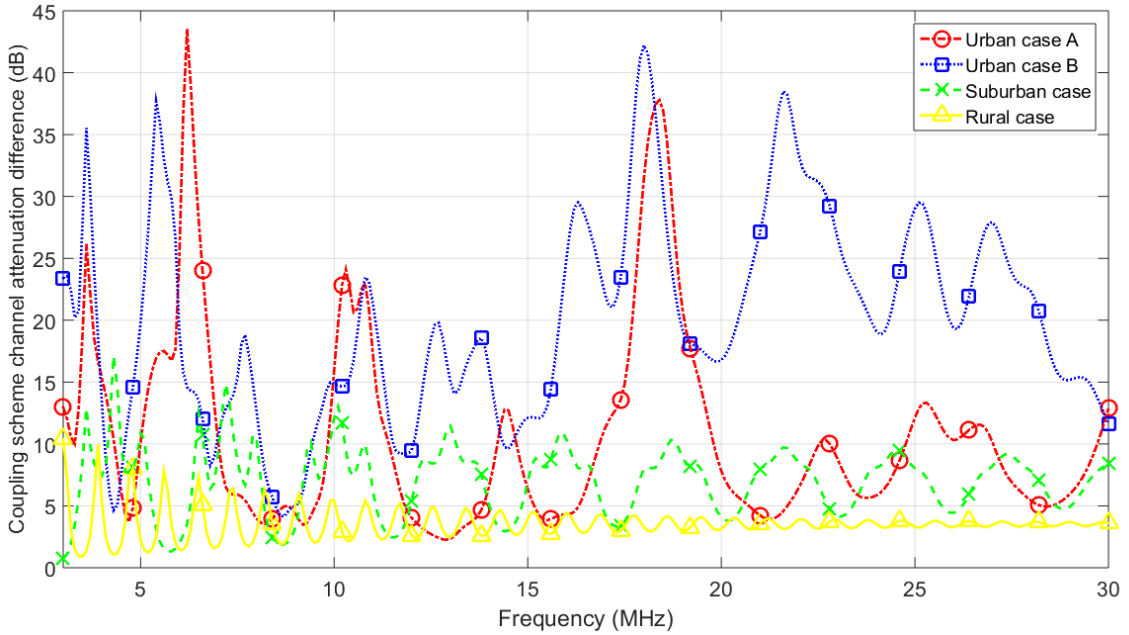

Fig. 3. Coupling scheme channel attenuation difference of the indicative UN MV BPL topologies of Table 2 in the 3-30MHz frequency band when StP[1] coupling scheme is deployed (the subchannel frequency spacing is equal to 0.1MHz).

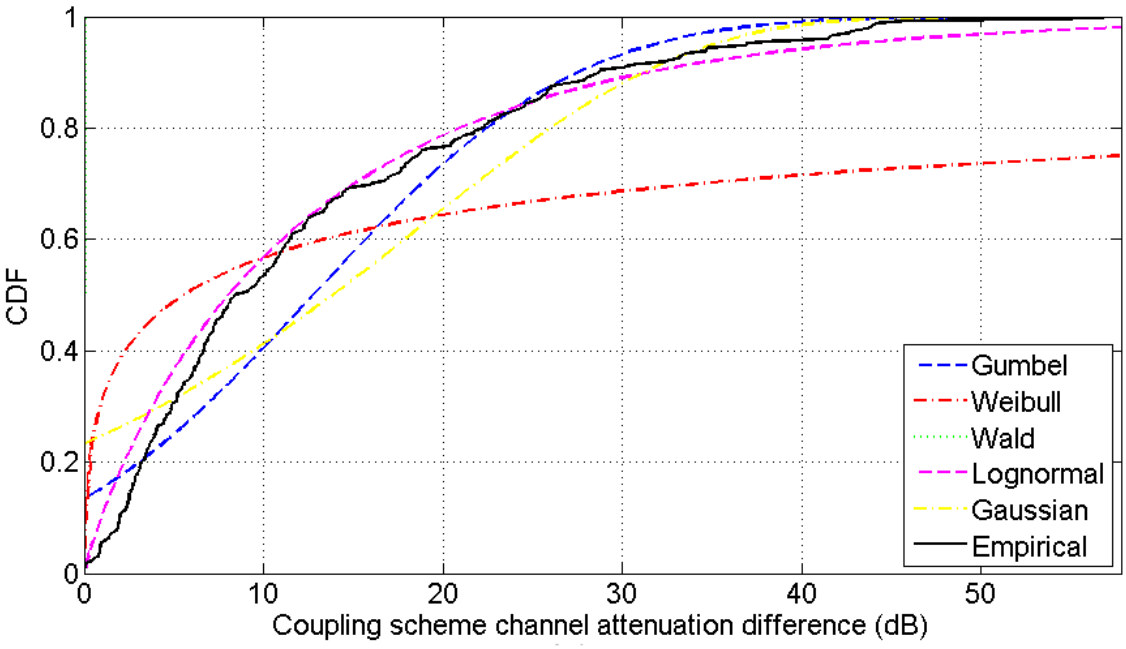
CDF
Coupling scheme channel attenuation difference (dB)
Gumbel
Weibull
Wald
Lognormal
Gaussian
Empirical

(a)

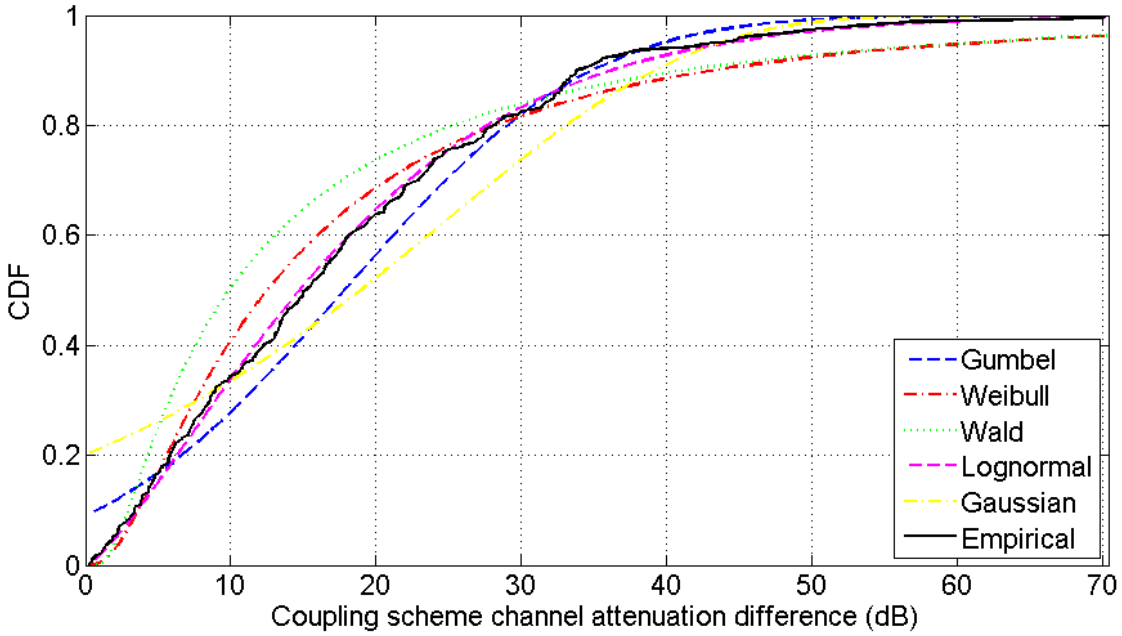
CDF
Coupling scheme channel attenuation difference (dB)
Gumbel
Weibull
Wald
Lognormal
Gaussian
Empirical

(b)

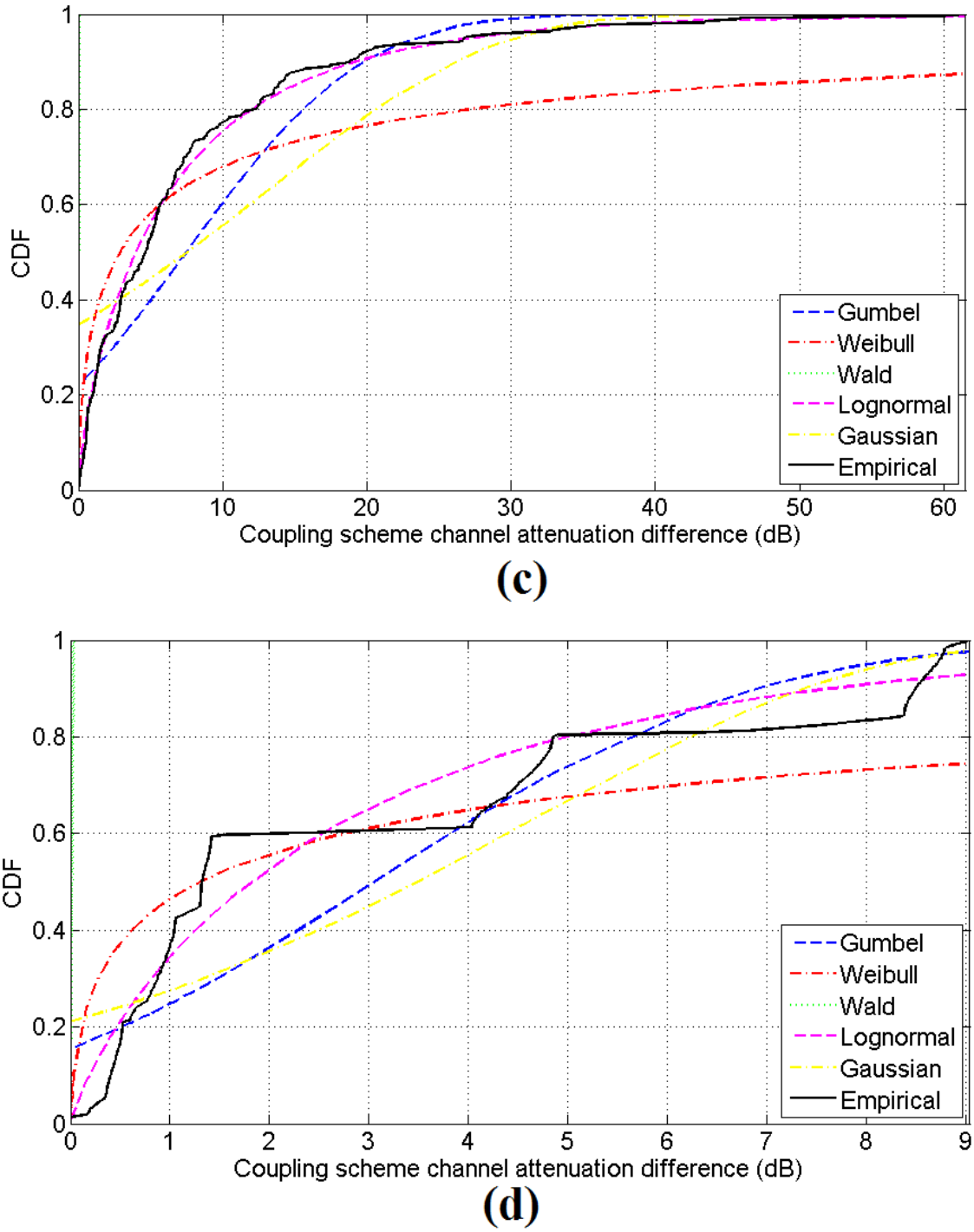

Fig. 4. CDF of the indicative OV MV BPL topologies of Table 1 versus coupling scheme channel attenuation difference in the 3-30MHz frequency band when WtG[1] coupling scheme is deployed. (a) Urban case A. (b) Urban case B. (c) Suburban case. (d) Rural case.

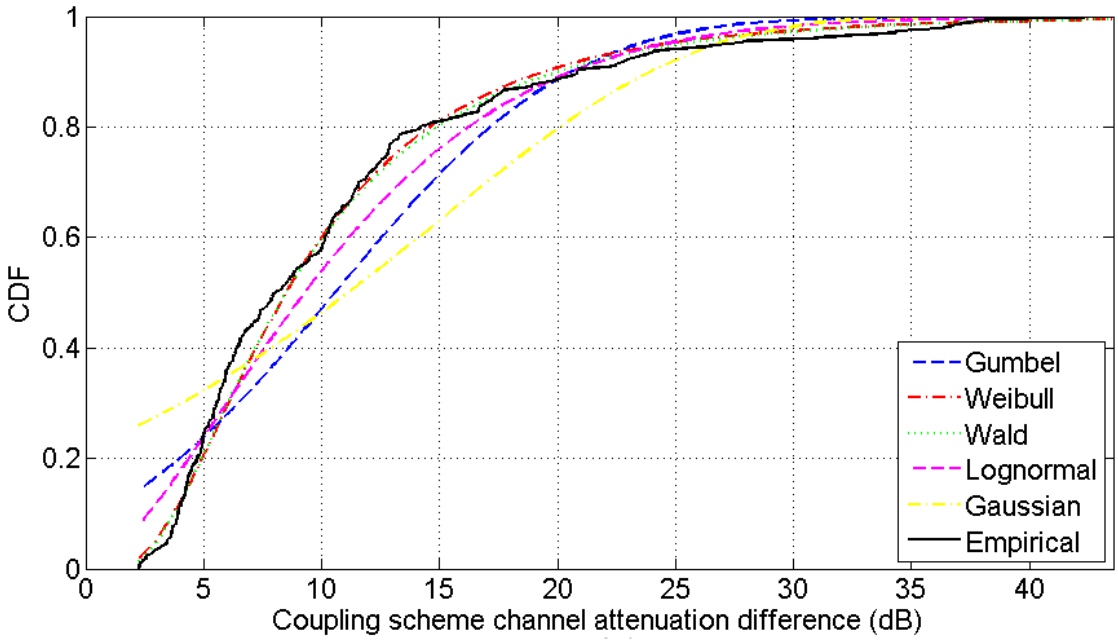
CDF
Coupling scheme channel attenuation difference (dB)
Gumbel
Weibull
Wald
Lognormal
Gaussian
Empirical

(a)

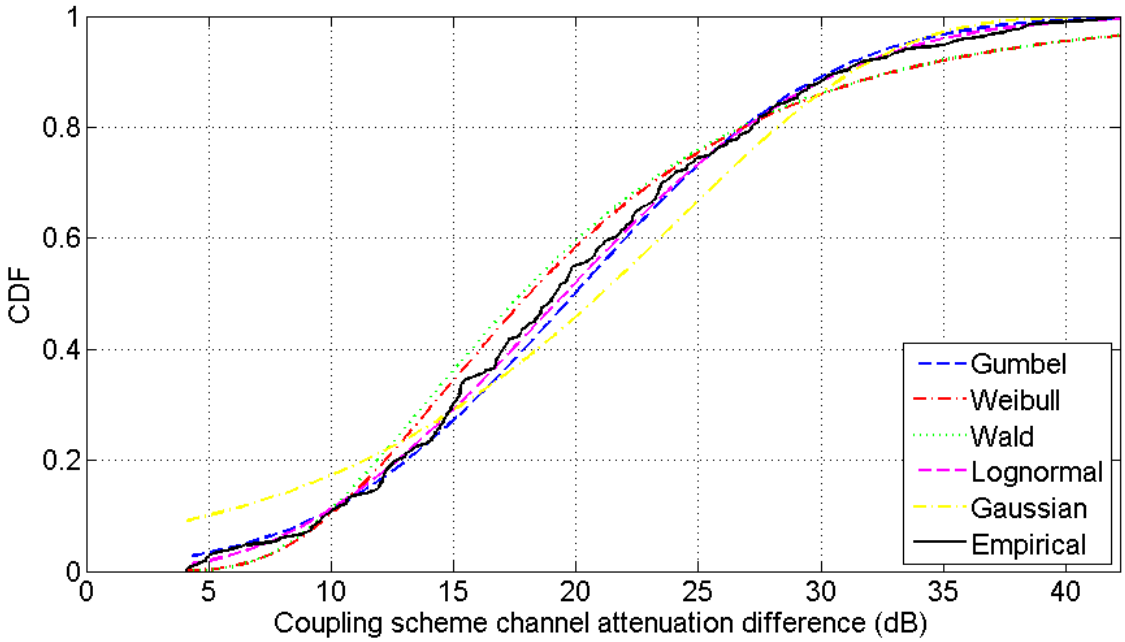
CDF
Coupling scheme channel attenuation difference (dB)
Gumbel
Weibull
Wald
Lognormal
Gaussian
Empirical

(b)

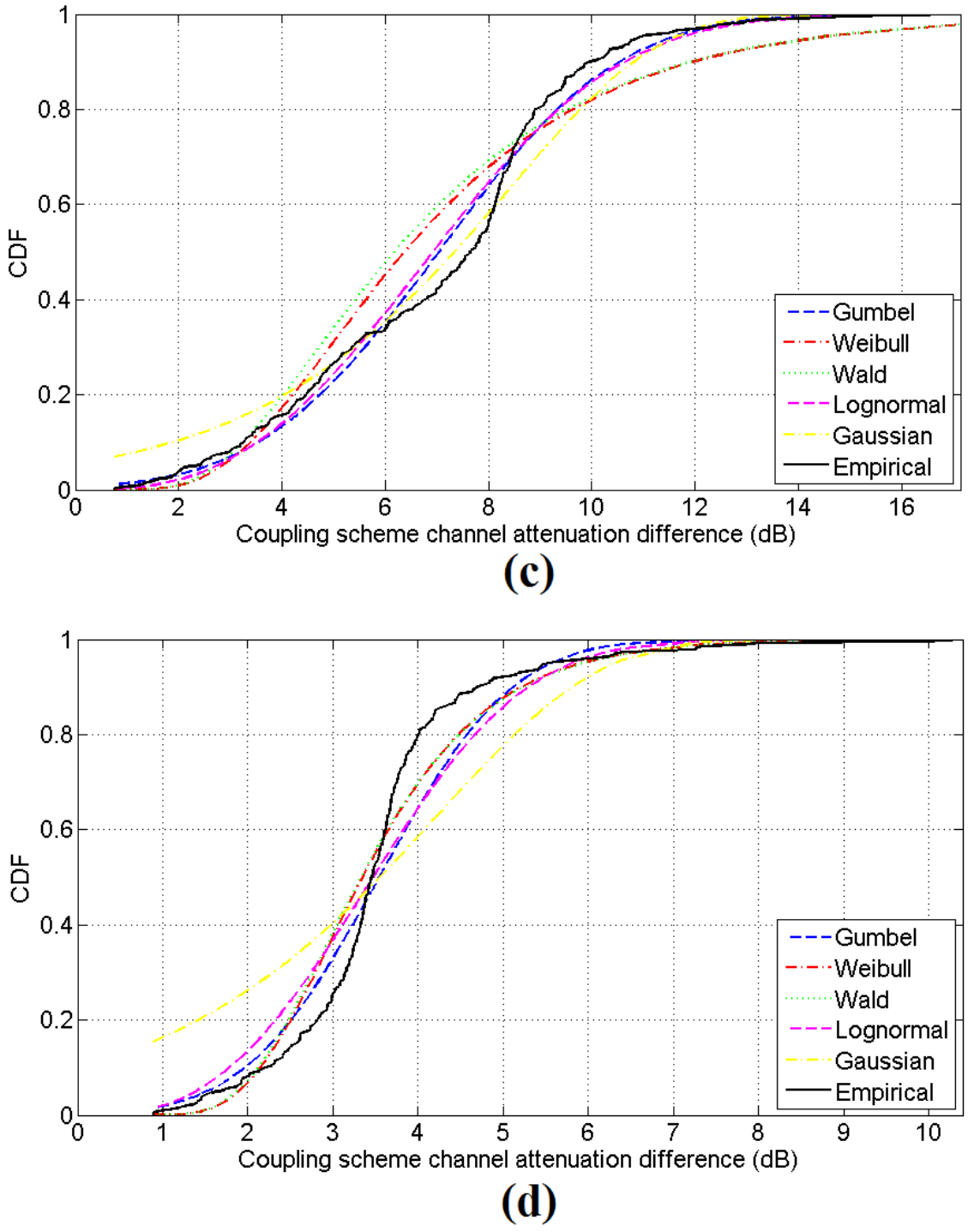

Fig. 5. Same plots with Fig. 4 but for the case of the indicative UN MV BPL topologies of Table 2 when StP[1] coupling scheme is deployed.

From Figs. 2-5, several interesting remarks can be reported concerning the CDF behavior of the channel attenuation statistical distributions of the initial and modified statistical hybrid model. More specifically:

- By comparing Figs. 2 and 3, it is evident that the coupling scheme channel attenuation difference of OV MV BPL topologies presents higher spectral notches in comparison with the ones of UN MV BPL topologies. This is due to the fact that the main channel attenuation mechanism of OV MV BPL networks is the multipath propagation in contrast with the high "LOS" propagation of UN MV BPL networks [8], [12]-[15], [17]. Due to this attenuation mechanism, the Empirical CDFs of OV MV BPL topologies, which are demonstrated in Figs. 4(a)-(d), normally start to increase from zero whereas Empirical CDF of UN MV BPL topologies, which are presented in Figs. 5(a)-(d), start to increase from positive values greater than zero depending on the examined indicative UN MV BPL topology. Also, apart from the distribution BPL rural case, Empirical CDFs of OV MV BPL topologies reach up to 1 at significant higher coupling scheme channel attenuation differences in contrast with the CDFs of UN MV BPL topologies.
- In the vast majority of the indicative distribution BPL topologies examined, Gaussian, Lognormal, Wald, Weibull and Gumbel channel attenuation statistical distributions asymptotically approach heights of 0 and 1 out of the range of minimum and maximum coupling scheme channel attenuation difference of the examined BPL topology. Conversely, the Empirical channel attenuation statistical distribution accurately represents the coupling scheme channel attenuation difference for given distribution BPL topology. For that reason, horizontal steps occur in the Empirical channel attenuation statistical distribution whose extent depends on the examined distribution BPL topology. Distribution BPL topologies that are characterized by frequent and of the same height coupling scheme channel attenuation difference notches (e.g., indicative OV MV BPL rural case) tend to be characterized by CDFs of important horizontal steps.
- Since shorter horizontal steps occur in indicative UN MV BPL topologies, the CDFs of the five channel attenuation statistical distributions of the initial statistical hybrid model can better fit the CDF of the Empirical distribution of the modified statistical hybrid model in contrast with their fit in indicative OV MV BPL topologies. Despite the fact of the better fit in indicative UN MV BPL topologies, the five channel attenuation statistical distributions fail to accurately approach the CDF heights of 0 and 1 thus entailing that the random number generator module of Phase D is going to produce: (i) lower coupling scheme channel attenuation differences than the real ones and a lot of zero coupling scheme channel attenuation differences; and (ii) higher coupling scheme channel attenuation differences than the real ones, respectively, for given distribution BPL topology.
- The CDF of the Wald channel attenuation statistical distribution fails to fit the Empirical distribution in the indicative OV MV BPL urban case A, suburban case and rural case. This is due to the MLEs provided by the MLE computation module of Phase C for the given coupling scheme channel attenuation differences (see Table 1 of [6]).
- Although the random number generator module of Phase D is going to produce random coupling scheme channel attenuation differences for the distribution BPL topology members that are more realistic to the indicative ones when the Empirical channel attenuation statistical distribution is applied, this does not

automatically imply that the Empirical distribution can achieve better capacity metrics than the Gaussian, Lognormal, Wald, Weibull and Gumbel channel attenuation statistical distributions. In accordance with [6], the performance metrics, which are used in this paper during the comparison evaluation of the initial and modified statistical hybrid model, are the capacity percentage change and average absolute capacity percentage change whose values also depend on the positions of the random coupling scheme channel attenuation differences, EMI policy and coupling scheme.

Consequently, after Phases A-D of either the initial or the modified statistical hybrid model, each BPL topology class is enriched with 100 topology members per each channel attenuation statistical distribution through the random coupling scheme channel attenuation differences that are produced by the random number generator (see in [5], [6]) for given power grid type and coupling scheme. Then, Phase E determines the coupling scheme transfer function of the members of each BPL topology class for given power grid type and coupling scheme. In the following subsections, the maximum, the average and the minimum capacity of each BPL topology class, which are hereafter denoted as capacity range of each BPL topology class, are going to be computed by the Phase F while the critical performance metrics of the capacity percentage change and average absolute capacity percentage change are evaluated so that the success of the channel attenuation statistical distribution of the initial and modified statistical hybrid model are assessed for the default operation settings as well as a number of different scenarios.

5.2 Initial and Modified Statistical Hybrid Model – Capacity Ranges of OV MV and UN MV BPL Classes for the Default Operation Settings

Since coupling scheme transfer functions of each distribution BPL topology class member are well computed by Phase E of the statistical hybrid model for each channel attenuation statistical distribution for given power grid type and coupling scheme, Phase F of the initial or modified statistical hybrid model computes the maximum, the average and the minimum capacity of each BPL topology class among its 100 BPL topology members for given power grid type, coupling scheme, channel attenuation statistical distribution and EMI policy.

Based on the theoretical framework of [5] and the findings of [6], the comparison of the initial and modified statistical hybrid model is going to be based on the successful capacity for given channel attenuation statistical distribution in terms of the metrics of capacity percentage change and average absolute capacity percentage change. In [6], it has been demonstrated for the initial statistical hybrid model that Weibull and Wald channel attenuation statistical distributions perform the best capacity estimations in OV MV and UN MV power grid types, respectively, regardless of the examined BPL topology class when the default operation settings are assumed. In fact, the previous observations are validated by the metrics of capacity percentage change and average absolute capacity percentage change in Table 3 of [6]. In order to evaluate the success performance of the Empirical channel attenuation statistical distribution, in Fig. 6(a), the maximum, average and minimum capacity of the typical OV MV urban topology class is plotted for the Weibull distribution of the initial statistical hybrid model and the Empirical distribution of the modified statistical hybrid model when the default operation settings are assumed. Also, the capacity of the indicative BPL topology of the

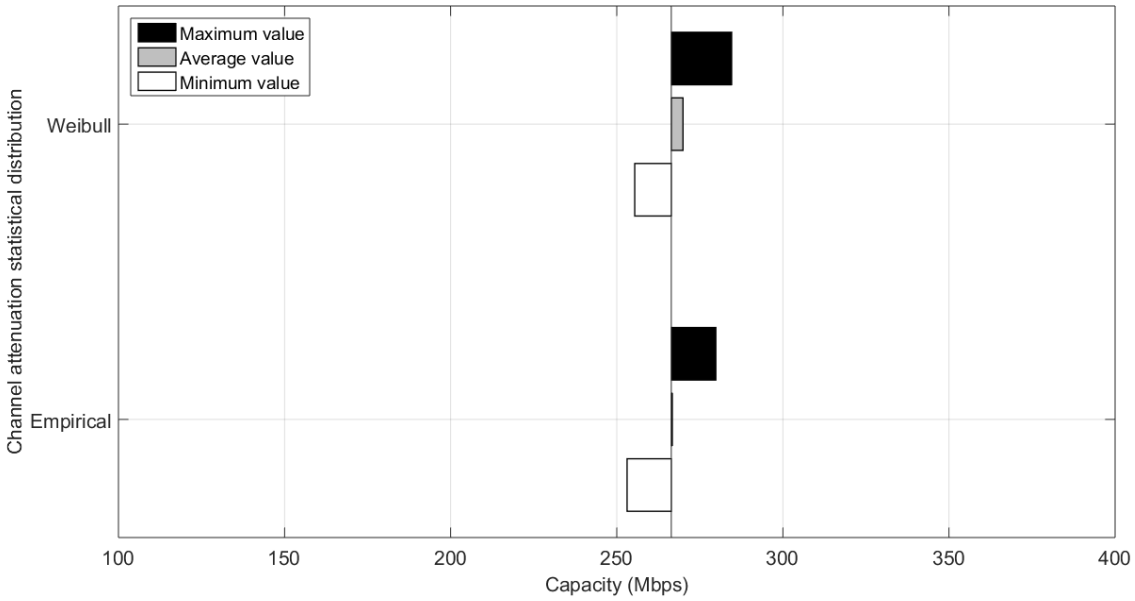
Maximum value
Average value
Minimum value
Channel attenuation statistical distribution
Weibull
Empirical
100
150
200
250
300
350
400
Capacity (Mbps)

(a)

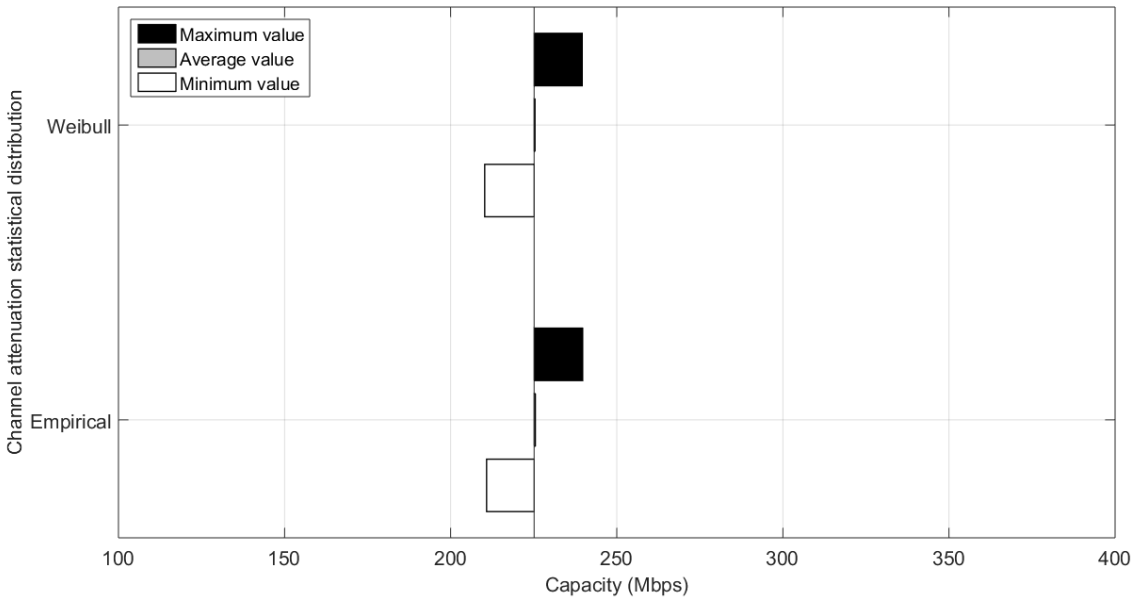
Maximum value
Average value
Minimum value
Channel attenuation statistical distribution
Weibull
Empirical
100
150
200
250
300
350
400
Capacity (Mbps)

(b)

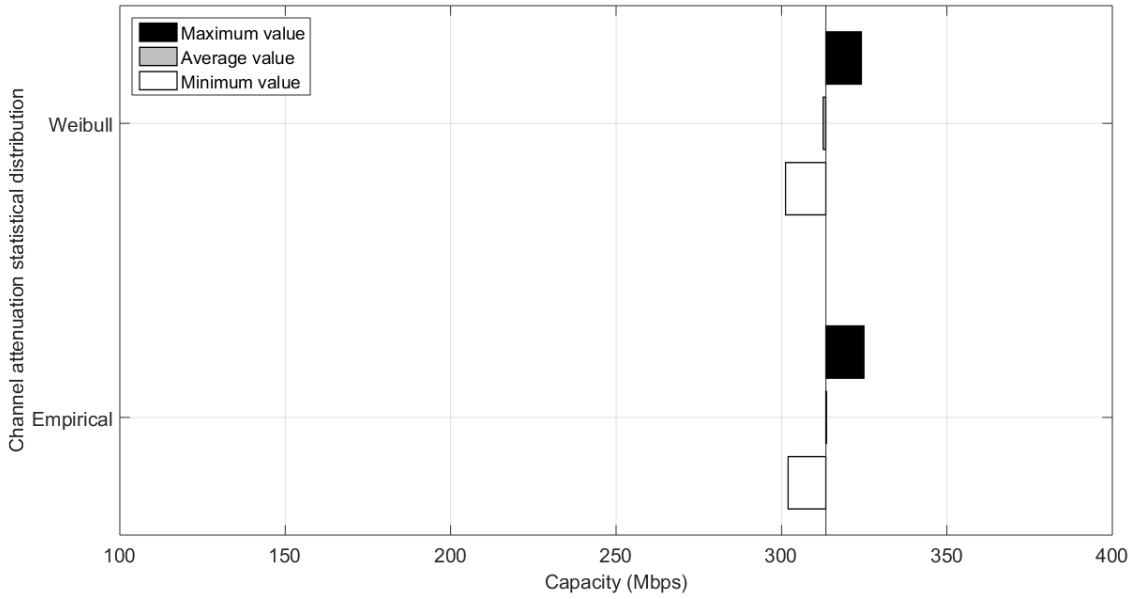

(c)

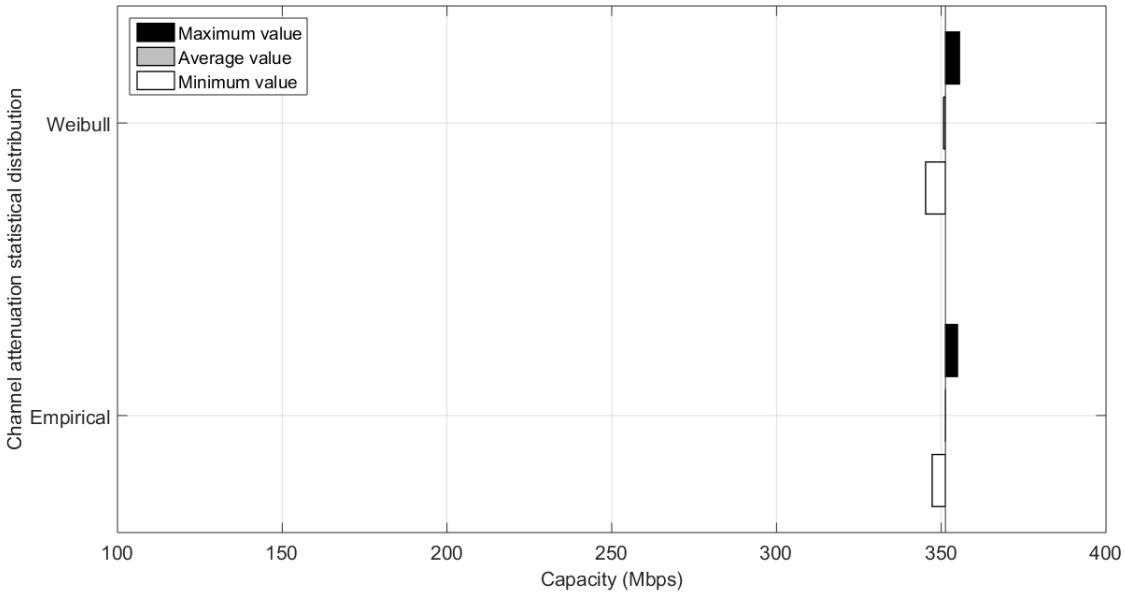

(d)

Fig. 6. Maximum, average and minimum OV MV BPL topology class capacities for the Weibull and Empirical channel attenuation statistical distribution of the initial and modified statistical hybrid model, respectively. (a) Typical OV MV BPL urban topology class. (b) Aggravated OV MV BPL urban topology class. (c) OV MV BPL suburban topology class. (d) OV MV BPL rural topology class.

BPL topology class, say, OV MV urban case A, that is computed by the hybrid model is used as the reference value of the figure. In Figs. 6(b)-(d), same bar graphs are demonstrated with Fig. 6(a) but for the aggravated OV MV BPL urban topology class, OV MV BPL suburban topology class and OV MV BPL rural topology class, respectively. Figs. 7(a)-(d) are the same with the respective Figs. 6(a)-(d) but for the UN MV BPL topology classes and Wald channel attenuation statistical distribution instead of Weibull one.

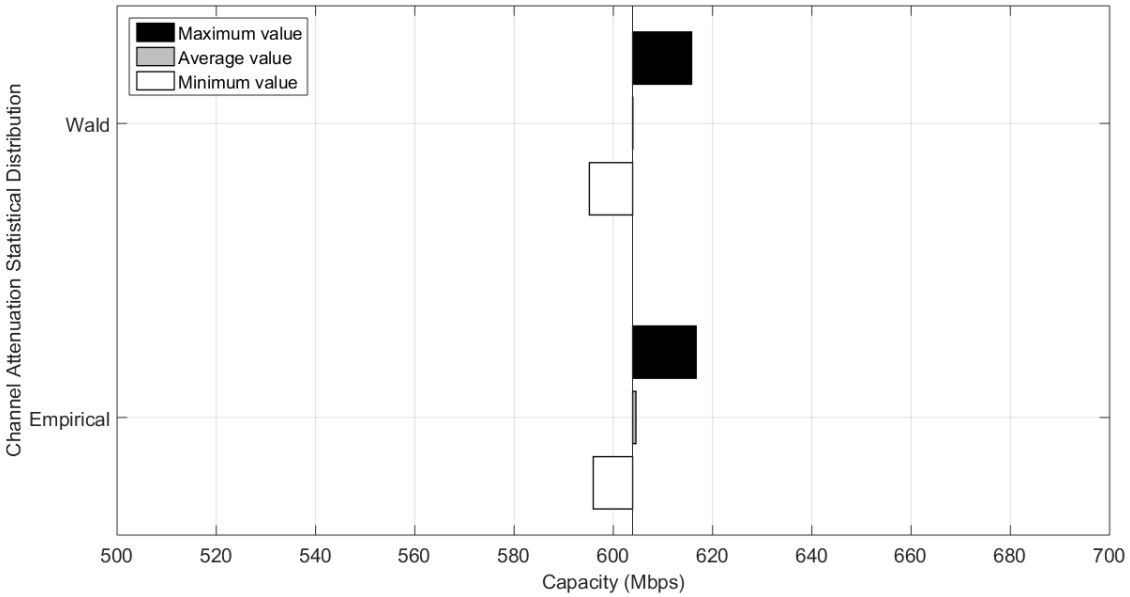
Maximum value
Average value
Minimum value
Channel Attenuation Statistical Distribution
Wald
Empirical
500
520
540
560
580
600
620
640
660
680
700
Capacity (Mbps)

(a)

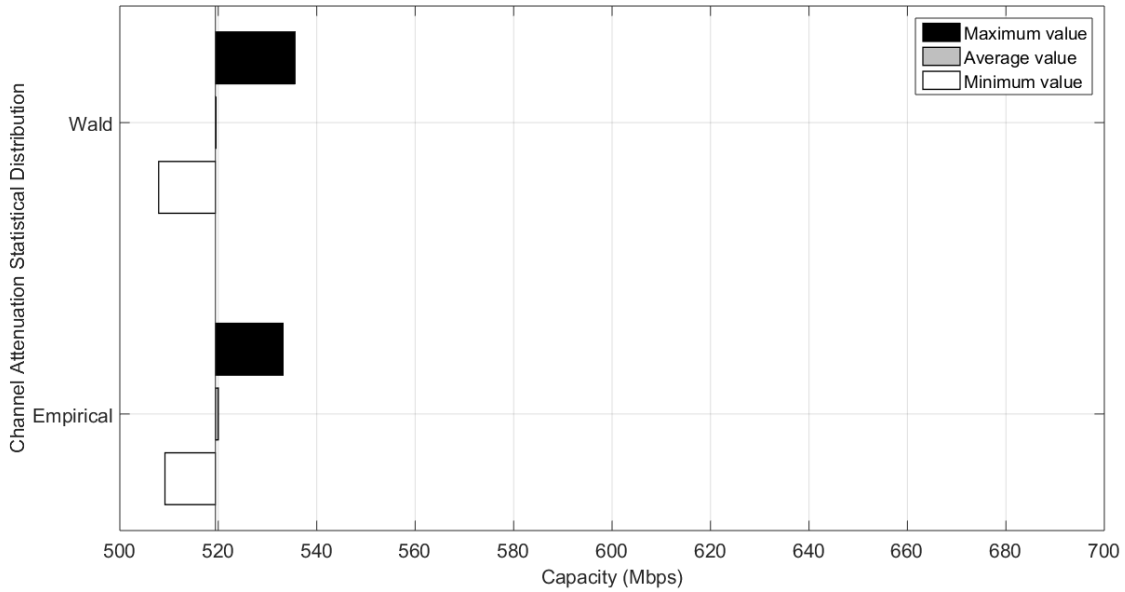
Maximum value
Average value
Minimum value
Channel Attenuation Statistical Distribution
Wald
Empirical
500
520
540
560
580
600
620
640
660
680
700
Capacity (Mbps)

(b)

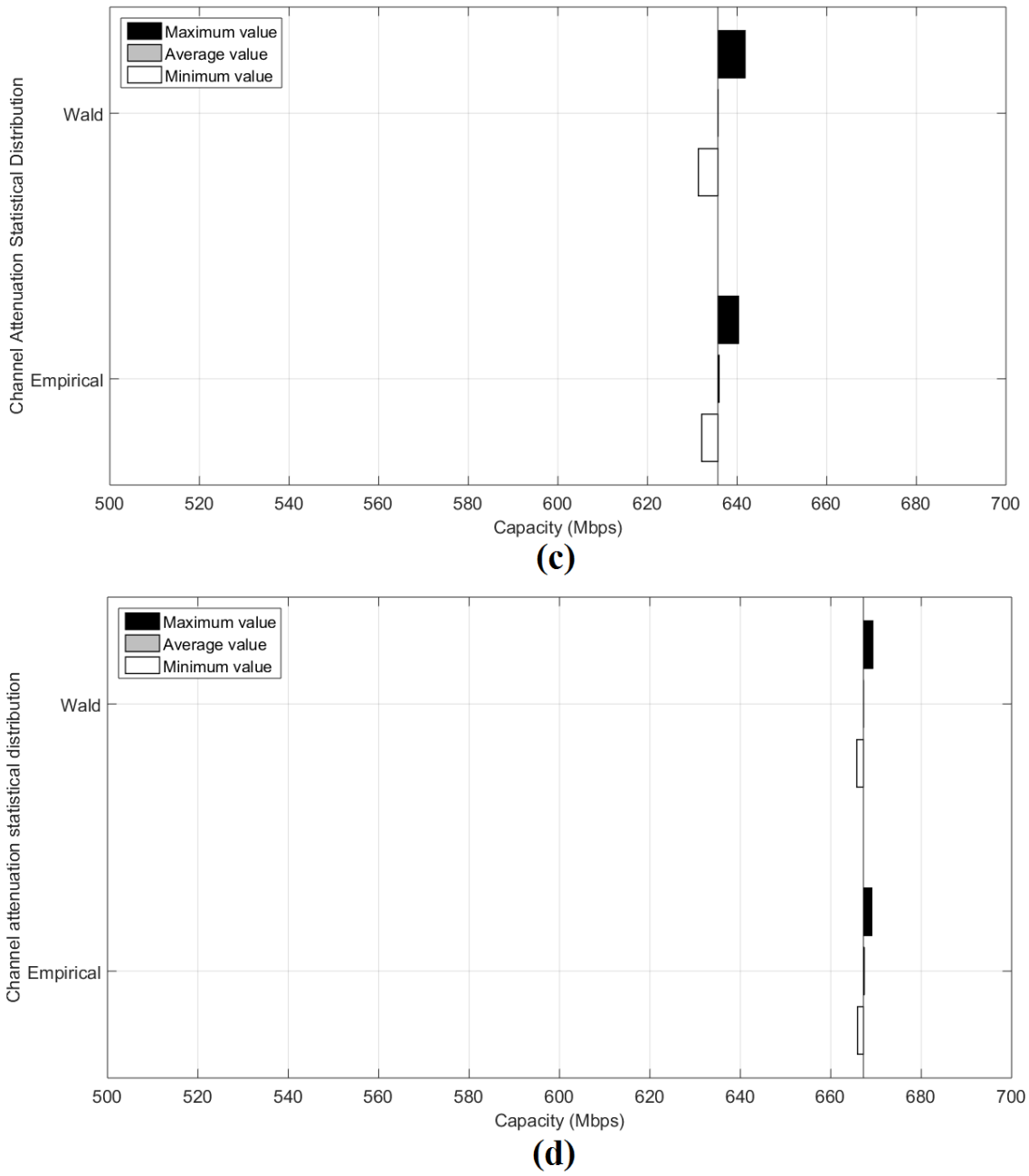

Fig. 7. Same curves with Fig. 6 but for the UN MV BPL topology classes and the Wald channel attenuation statistical distribution instead of the Weibull one .

The behavior of channel attenuation statistical distribution CDFs of Figs. 4(a)-(d) and 5(a)-(d) can be reflected on the respective Figs. 6(a)-(d) and 7(a)-(d), namely:

- In accordance with [6], a channel attenuation statistical distribution is considered to be successful if the following two criteria are satisfied, namely: (i) capacity range of each distribution BPL topology class (say, the minimum and the maximum capacity value of the distribution BPL topology class) comprises the capacity of the respective indicative distribution BPL topology; and (ii) the average capacity value of the distribution BPL topology class remains very

close to the respective one of the indicative distribution BPL topology. Already been validated for the Weibull and Wald statistical distributions, which present the best performance for the OV MV and UN MV BPL topology classes, respectively, the Empirical channel attenuation statistical distribution also satisfies both the criteria in all the examined OV MV and UN MV BPL topology classes.

- To numerically assess the capacity estimation success of channel attenuation statistical distributions of the initial and modified statistical hybrid model, the metrics of percentage change and the average absolute percentage change, which have been proposed in [6], are applied apart from the graphical comparison of Figs. 6 and 7. Here, it should be reminded that the percentage change computes the difference percentage between the capacity average value of the examined distribution BPL topology class in relation with the respective indicative distribution BPL topology for given channel attenuation statistical distribution. Then, the average absolute percentage change is equal to the average value of the absolute percentage changes of the four distribution BPL topology classes for given power grid type and channel attenuation statistical distribution.
- In accordance with [6], high values of percentage change indicate that the estimation of the applied channel attenuation statistical distribution is unsuccessful while a threshold of 3% (i.e., first rule of thumb in [6]) has been proposed either in the percentage change or in the average absolute percentage change so that the partial and overall success capacity estimation can be numerically checked. With reference to Table 3 of [6], it is also numerically validated that Weibull and Wald channel attenuation statistical distributions perform the best capacity estimations in OV MV and UN MV power grid types, respectively, regardless of the examined BPL topology class when the default operation settings are assumed.

In Table 3, the percentage change of each OV MV BPL topology class is reported for the Weibull channel attenuation statistical distribution, which performs the best capacity estimation in OV MV BPL topology classes for the initial statistical hybrid model, and for the Empirical channel attenuation statistical distribution for the modified statistical hybrid model. Similarly to the OV MV BPL topology class case, the percentage change of each UN MV BPL topology class is reported in the same Table but for the Wald channel attenuation statistical distribution, which performs the best capacity estimation in UN MV BPL topology classes for the initial statistical hybrid model. Also, at the bottom of the Table, the average absolute percentage change of each channel attenuation statistical distribution is given per each power grid type.

The results that are reported in Table 3 numerically verify the graphical observations of Figs. 6 and 7. More specifically:

- The rule of thumb of 3% threshold, denoted as first rule of thumb, is valid in all the cases examined for the applied channel attenuation statistical distributions when the default operation settings are assumed. The first rule of thumb is valid for the Empirical channel attenuation statistical distribution either in all distribution BPL topology classes (i.e., the absolute value of percentage change significantly remains below 3% in all the examined distribution BPL topology classes) or in the examined power grid type as a whole

Table 3
Percentage Change of the Distribution BPL Topology Classes for the Best Channel Attenuation Statistical Distributions of the Initial Statistical Hybrid Model and the Empirical Channel Attenuation Statistical Distribution of the Modified Statistical Hybrid Model (The Default Settings Are Assumed, say, WtG^1/StP^1 coupling scheme and FCC Part 15)
(black background: unsuccessful CDF estimation)

Indicative BPL Topology Name (OV MV Capacity / UN MV Capacity in Mbps)	**BPL Topology Class Description**	**Percentage Change (%)**			
		Initial Statistical Hybrid Model		**Modified Statistical Hybrid Model**	
		Best Channel Attenuation Statistical Distribution		**Empirical Channel Attenuation Statistical Distribution**	
		OV MV (Weibull)	UN MV (Wald)	OV MV	UN MV
Urban case A (266 / 604)	Typical BPL urban class	1.32	0.01	0.10	0.11
Urban case B (225 / 519)	Aggravated BPL urban	0.12	0.02	0.18	0.11
Suburban case (313 / 636)	BPL suburban class	-0.26	0.003	0.07	0.04
Rural case (351 / 667)	BPL rural class	-0.16	0.0004	0.01	0.02
Average Absolute Percentage Change (%)		**0.47**	**0.01**	**0.09**	**0.07**

(i.e., the average absolute percentage change of OV MV and UN MV BPL networks also remains below 3%). In accordance with [6] and the Table 3, Weibull and Wald channel attenuation statistical distributions comply with the first rule of thumb in OV MV and UN MV BPL topology classes, respectively. In total, since all the examined cases are in compliance with the first rule of thumb, there is no cell in black background.

- In addition, the metrics of the percentage change and the average absolute percentage change assess the success of the channel attenuation statistical distributions, namely:
    - In OV MV BPL topology classes, the application of the Empirical channel attenuation statistical distribution has achieved better percentage change results in 3 out of 4 classes (i.e., typical OV MV BPL urban class, OV MV BPL suburban class and OV MV BPL rural class) with significant improvement while the percentage change difference between the Weibull and Empirical channel attenuation statistical distributions remain low in the case of the aggravated OV MV BPL class.
    - In UN MV BPL topology classes, the application of the Empirical channel attenuation statistical distribution has not achieved the best percentage change results in comparison with the ones of the Wald channel attenuation statistical distribution but the differences remain low.
    - The results of the average absolute percentage change verify that the Empirical channel attenuation statistical distribution can provide reliable results that are comparable to the best ones that can be achieved by the initial statistical hybrid model through its five channel attenuation statistical distribution.

After the graphical analysis and the performance metric analysis for the default operation settings, it is shown that the Empirical channel attenuation statistical distribution of the modified statistical hybrid model can safely substitute the statistical distributions of the initial statistical hybrid model with very satisfactory results. It should be noted that the application of the Empirical channel attenuation statistical distribution allows the bypass of the comparison/selection process among the five statistical distributions that is anyway a time consuming process and imply the application of all the five statistical distributions. However, the performance of the Empirical channel attenuation statistical distributions is investigated in Sec.5.3 and Sec.5.4 when different scenarios concerning the operation scenarios are applied similarly to Sec.2.2 and Sec.2.3 of [6], respectively.

5.3 Initial and Modified Statistical Hybrid Models for Different EMI Policies

Already been mentioned in Sec.4.2, EMI policies regulate the EMI of BPL system operation so that OV MV and UN MV BPL networks do not become sources of EMI to other already existing wireless and telecommunications systems [8], [13], [15], [48]-[50]. Apart from the IPSD limits of the FCC Part 15, that are considered anyway among the default operation settings, respective IPSD limits of German Reg TP NB30 and the BBC/NATO Proposal, which are computed in [43], [44], [112], can be assumed to act as the different scenarios in order to examine the impact of different EMI policies on the performance of the initial and modified statistical hybrid models.

Similarly to [6], since no MTL configuration, BPL topology and coupling scheme changes occur in the examined scenario, the CDFs and the coupling scheme channel attenuation values of the channel attenuation statistical distributions of the initial and modified statistical hybrid models concerning the indicative OV MV and UN MV BPL topologies remain the same with the respective ones of Sec. 5.1 and 5.2.

To numerically assess the performance of the initial and modified statistical hybrid model when lower IPSD limits in comparison with those of FCC Part 15 ones are applied, the percentage change and the average absolute percentage change are reported for the indicative distribution BPL topology classes of Tables 1 and 2; in Tables 4 and 5, the percentage change and the average absolute percentage change are computed when German Reg TP NB30 and BBC/NATO Proposal are applied, respectively.

In accordance with [6] and by comparing Tables 4 and 5 with Table 3, it is obvious that the more EMI protective to other telecommunication services IPSD limits (i.e., German Reg TP NB30 and BBC/NATO proposal) entail significant capacity reductions and unsuccessful capacity estimations either in OV MV or in UN MV BPL topologies regardless of the applied statistical hybrid model and channel attenuation statistical distribution. The following observations can be pointed out:

- As the initial statistical hybrid model is concerned, Weibull and Wald channel attenuation statistical distributions are not the dominant distributions to estimate in total the capacity of the OV MV and UN MV BPL topology classes, respectively. A mix of different channel attenuation statistical distributions can now describe the different distribution BPL topology classes. For each distribution BPL topology class, the selection of the best channel attenuation statistical distribution in terms of the percentage change among the five ones depends on the power grid type, the BPL topology class and

Table 4
Same with Table 3 but for German Reg TP NB30.

Indicative BPL Topology Name (OV MV Capacity / UN MV Capacity in Mbps)	**BPL Topology Class Description**	**Percentage Change (%)**			
		Initial Statistical Hybrid Model		**Modified Statistical Hybrid Model**	
		Best Channel Attenuation Statistical Distribution		**Empirical Channel Attenuation Statistical Distribution**	
		OV MV	UN MV	OV MV	UN MV
Urban case A (5.99 / 218)	Typical BPL urban class	1.97 (Gaussian)	-0.27 (Weibull)	4.99	0.87
Urban case B (3.93 / 144)	Aggravated BPL urban	1.61 (Lognormal)	0.09 (Lognormal)	-3.37	-0.88
Suburban case (10.75 / 248)	BPL suburban class	2.38 (Weibull)	0.001 (Gaussian)	0.29	0.12
Rural case (14.88 / 280)	BPL rural class	1.97 (Weibull)	-0.001 (Gaussian)	0.50	0.06
Average Absolute Percentage Change (%)		**1.98**	**0.09**	**2.28**	**0.48**

Table 5
Same with Table 3 but for BBC/NATO Proposal.

Indicative BPL Topology Name (OV MV Capacity / UN MV Capacity in Mbps)	**BPL Topology Class Description**	**Percentage Change (%)**			
		Initial Statistical Hybrid Model		**Modified Statistical Hybrid Model**	
		Best Channel Attenuation Statistical Distribution		**Empirical Channel Attenuation Statistical Distribution**	
		OV MV	UN MV	OV MV	UN MV
Urban case A (0.0017 / 9.83)	Typical BPL urban class	10.92 (Gaussian)	10.02 (Wald)	7.31	13.53
Urban case B (0.0011 / 4.65)	Aggravated BPL urban	-2.54 (Lognormal)	8.41 (Gumbel)	-5.13	-35.74
Suburban case (0.0032 / 14.28)	BPL suburban class	2.37 (Gumbel)	-0.28 (Lognormal)	0.21	-1.73
Rural case (0.0045 / 22.09)	BPL rural class	2.16 (Weibull)	0.09 (Lognormal)	0.67	0.35
Average Absolute Percentage Change (%)		**4.50 (mixed)**	**4.70 (mixed)**	**3.33**	**12.84**

the applied EMI policy. As the modified statistical hybrid model is examined, the Empirical channel attenuation statistical distribution demonstrates a fairly stable behavior that anyway depends on the same aforementioned factors.

- As German Reg TP NB30 is applied in the indicative OV MV BPL topology classes, a mix of three different channel attenuation statistical distributions of the initial statistical hybrid model (say, Gaussian, Lognormal and Weibull) needs to be adopted so that a fine capacity estimation can be achieved in compliance with the first rule of thumb. At the same time, the Empirical channel attenuation distribution of the modified statistical hybrid model performs better estimations than the ones of the aforementioned distributions of the initial statistical hybrid model when OV MV BPL suburban and rural topology classes are examined.

In contrast, the Empirical channel attenuation statistical distribution fails to provide a successful estimation in OV MV BPL urban topology classes.

- As BBC/NATO proposal is applied in the indicative OV MV BPL topology classes, the number of unsuccessful capacity estimations of the initial and modified statistical hybrid model skyrockets, which is anyway shown from the dramatic increase of the percentage change values. Actually, Lognormal, Gumbel and Weibull channel attenuation statistical distributions of the initial statistical hybrid model are the most suitable to estimate the capacity of the indicative OV MV BPL urban case B, suburban and rural topology classes, respectively, in compliance with the first rule of thumb while the capacity estimation of the indicative OV MV BPL urban case A topology class remains unsuccessful. Again, the Empirical channel attenuation statistical distribution of the modified statistical hybrid model achieves better capacity estimation results than the ones of the statistical distributions of the initial statistical hybrid model in the suburban and rural cases while its capacity estimation remains unsuccessful during the capacity computations of the urban cases.
- Similarly to the OV MV BPL topology classes, as German Reg TP NB30 is applied in the indicative UN MV BPL topology classes, a mix of three different channel attenuation statistical distributions of the initial statistical hybrid model (say, Weibull, Lognormal and Gaussian) needs to be implemented so that a fine capacity estimation can be achieved on the basis of the first rule of thumb. Note that the Lognormal channel attenuation statistical distribution achieves the best capacity estimations in urban case B topology class when German Reg TP NB30 is applied regardless of the examined power grid type. Here, the capacity estimations of the distributions of the initial statistical hybrid model remains better than the ones of the Empirical channel attenuation statistical distribution but with a decent percentage change difference.
- As BBC/NATO proposal is applied in the indicative UN MV BPL topology classes, the best channel attenuation statistical distribution of the initial statistical hybrid model is the Lognormal one when the suburban and rural BPL topology classes are examined. In the case of the urban BPL topology classes, the channel attenuation statistical distributions of the initial statistical hybrid model fail to perform a successful capacity estimation. In a similar way to the statistical distributions of the initial statistical hybrid model, the Empirical channel attenuation statistical distribution successfully estimates the capacity of the BPL suburban and rural topology classes in contrast with the BPL urban topology classes. Anyway, the percentage change difference between the Lognormal and the Empirical channel attenuation statistical distribution in UN MV BPL suburban and rural topology classes remains low.
- All the previous observations can be explained through the prism of the second rule of thumb proposed in [6]. In accordance with this second rule of thumb, the percentage change of the channel attenuation statistical distributions of the initial statistical hybrid model remains inversely proportional to the capacity. Indeed, when strict EMI policies are adopted, the capacity of all the indicative distribution BPL topologies is significantly reduced. Thus, the percentage changes of the channel attenuation statistical distributions of the initial statistical hybrid model increase while these percentage changes are more affected when

BBC/NATO proposal is adopted and urban distribution BPL topology classes are examined. The same results occur in the Empirical channel attenuation statistical distribution.

- With reference to the average absolute percentage change, the modified hybrid statistical model presents almost the same behavior with the initial one. When German Reg TP NB30 is adopted, both hybrid statistical models successfully estimate the capacities of the BPL topology classes in a whole regardless of the power grid type. Conversely, both the statistical hybrid models fail to successfully estimate the capacities of the BPL topology classes in a whole when BBC/NATO proposal is applied.
- To detect the best channel attenuation statistical distribution of the initial statistical hybrid model in terms of the percentage change, the percentage change of each statistical distribution should be computed for given distribution BPL topology class and after comparing their percentage change results, the minimum percentage change is added in Tables 3-5 for given distribution BPL topology as well as the name of the statistical distribution. Since different channel attenuation statistical distributions of the initial hybrid model are used for the different distribution BPL topology classes, the average absolute percentage change is considered as the average value of the percentage changes of the best channel attenuation statistical distributions of distribution BPL topology classes for given power grid type, coupling scheme and EMI policies. The result of the average absolute percentage change describes the best possible average absolute percentage change for the initial statistical hybrid model that is anyway unachievable by only one channel attenuation statistical distribution. Conversely, the evaluation of the percentage change of the Empirical channel attenuation statistical distribution of the modified statistical hybrid model, which is added in Tables 3-5, is a straightforward process since there is no need for comparison delays among channel attenuation statistical distributions. At the same time, the evaluation of the average absolute percentage change of the Empirical channel attenuation statistical distribution of the modified statistical hybrid model, which is added in Tables 3-5, is the average among the four percentage changes for given power grid type, coupling scheme and EMI policy, which is again an easy and straightforward computation task.
- In accordance with [6], the unsuccessful capacity estimations of the channel attenuation statistical distributions when strict EMI policies are adopted is due to the fact that the German Reg TP NB30 and BBC/NATO proposal EMI policies present a strong frequency selective behavior [24]. Hence, the random position of the random coupling scheme channel attenuation differences produced by the random number generator module of Phase D is the suspect of the unsuccessful capacity estimations rather CDFs of random number generator.
- A trade-off between the computation / comparison time and the capacity estimation accuracy is here defined for the UN MV BPL topology classes. The initial statistical hybrid model achieves a slight improved percentage change and average absolute percentage change results in UN MV BPL topology classes in comparison with the ones of the modified statistical hybrid model regardless of the applied EMI policies but the computational time of the initial statistical hybrid model remains significantly higher in comparison with the one of the modified

statistical hybrid model. In contrast, when OV MV BPL topology classes are examined, the Empirical channel attenuation statistical distribution achieves significantly better percentage change and average absolute percentage change results in comparison with the ones of the five channel attenuation statistical distributions of the initial statistical hybrid model. At the same time, the Empirical channel attenuation statistical distribution achieves significantly better computational times. As the OV MV BPL topology classes are concerned, the modified statistical hybrid model is a straightforward selection.

In accordance with [6], strict EMI policies undermine the capacity estimations of the channel attenuation statistical distributions. Taking into account the high comparison delays of the initial statistical hybrid model, the Empirical channel attenuation statistical distribution of the modified statistical hybrid model proposes a fair and fast capacity estimation. Also, when OV MV BPL topology classes are examined, the Empirical channel attenuation statistical distributions offers the best possible and rapid capacity estimation. Apart from the different ISPD limits, the capacity estimation performance of the Empirical channel attenuation statistical distributions should also be examined when different coupling schemes are applied.

5.4 Initial and Modified Statistical Hybrid Models for Different Coupling Schemes

Already detailed in [5], [28], [47], CS2 module, which is the most updated BPL coupling scheme module, describes the injection of the input BPL signal onto and the extraction of the output BPL signal from the power lines of BPL networks through three different types of coupling schemes, namely: (1) *Coupling Scheme Type 1: Wire-to-Ground (WtG)* or *Shield-to-Phase (StP)* coupling schemes for OV or UN BPL networks, respectively; (2) *Coupling Scheme Type 2: Wire-to-Wire (WtW)* or *Phase-to-Phase (PtP)* coupling schemes for OV or UN BPL networks, respectively; and (3) *Coupling Scheme Type 3: MultiWire-to-MultiWire (MtM)* or *MultiPhase-to-MultiPhase (MtM)* coupling schemes for OV or UN BPL networks, respectively.

In [6], one representative coupling scheme per each coupling scheme type of CS2 module and power grid type has been chosen to be presented, namely: (i) *Coupling Scheme Type 1:* WtG^{1} and StP^{1} coupling schemes have been chosen for the OV MV and UN MV BPL networks, respectively; (ii) *Coupling Scheme Type 2:* WtW^{1-2} and PtP^{1-2} coupling schemes are applied for OV MV and UN MV BPL topology classes, respectively; and (iii) *Coupling Scheme Type 3:* $\mathrm{MtM}_{0.8\ -0.1\ -0.1}^{1-2-3}$ coupling scheme is applied for OV MV and UN MV BPL topology classes. In this paper, the aforementioned coupling schemes are applied for comparison reasons.

As the five channel attenuation statistical distributions of the initial statistical hybrid model are concerned, the different coupling schemes entail changes in coupling scheme channel attenuation and capacity values and for that reason new MLEs for the indicative OV MV BPL topologies of Table 1 and indicative UN MV BPL topologies of Table 2 should be recomputed. In fact, the MLEs of the five channel attenuation distributions of the initial statistical hybrid model for the indicative OV MV BPL topologies are reported in Table 6 of [6] when the default operation settings are assumed and WtW^{1-2} and $\mathrm{MtM}_{0.8\ -0.1\ -0.1}^{1-2-3}$ coupling schemes are applied. In Table 7 of [6], MLEs of the five channel attenuation distributions of the initial statistical hybrid model for the indicative UN MV BPL topologies are reported when the default operation settings are assumed and PtP^{1-2} and $\mathrm{MtM}_{0.8\ -0.1\ -0.1}^{1-2-3}$ coupling schemes are applied. As

the capacity and the corresponding metrics are regarded, the percentage change between each average capacity of the distribution BPL topology class and the capacity of the indicative topology of the respective class for the channel attenuation distributions of the initial and modified statistical hybrid model is given in Table 6 when the default operation settings are applied but for the WtW^{1-2} and PtP^{1-2} coupling schemes for OV MV and UN MV BPL topology classes, respectively. Here it should be noted that the respective MLEs of Table 6 and 7 of [6] for the five channel attenuation statistical distributions are applied while the best channel attenuation statistical distribution in terms of the percentage change and the Empirical channel attenuation statistical distribution are considered in the case of the initial and the modified statistical hybrid model, respectively. Similarly to Table 3, at the bottom of the Table, the average percentage change of each channel attenuation statistical distribution is given per each power grid type. In Table 7, same Table with Table 6 is given but for the application of $MtM_{0.8\ -0.1\ -0.1}^{1-2-3}$ coupling scheme for OV MV and UN MV BPL topology classes.

By comparing Tables 6 and 7 with Table 3, important observations can be made concerning the capacity estimation performance from the channel attenuation statistical distributions when different coupling schemes of CS2 module are applied, namely:

- In accordance with [6] and [47], by adopting CS2 module, WtW coupling schemes of OV MV BPL topologies and PtP coupling schemes of UN MV BPL topologies become almost equivalent to respective WtG coupling schemes and StP coupling schemes in terms of channel attenuation and capacity. MtM coupling schemes can achieve slightly better channel attenuation and capacity results in comparison with the ones of the previous coupling schemes due to their adaptive use of the available conductors of the examined MTL configurations.
- The impact of the different coupling schemes on the percentage change remains significantly lower in comparison with the impact of the different EMI policies. Additional evidence of this assertion is that among the channel attenuation statistical distributions of the initial statistical hybrid model, Weibull and Wald channel attenuation statistical distributions still best estimate capacity in OV MV and UN MV BPL topology classes, respectively, regardless of the coupling scheme applied when the default operation settings are adopted. In the case of the Empirical channel attenuation statistical distribution, the strongest evidence is that the percentage change values remain extremely lower in the case of the different coupling schemes rather than in the case of the different EMI policies.
- The second rule of thumb does not occur during the application of the Empirical channel attenuation statistical distribution since the observed percentage changes of the OV and UN MV BPL topology classes remain comparable. This is due to the fact that Empirical channel attenuation statistical distribution is based on Empirical CDFs in both power grid types and not on the best CDF of channel attenuation statistical distributions of the initial statistical hybrid model in terms of the percentage change.
- Different coupling schemes have little impact on the percentage change of Empirical channel attenuation statistical distribution for given power grid type and BPL topology class. Anyway, small percentage change differences among coupling schemes can be observed when MtM coupling schemes are applied.

Table 6
Same with Table 3 but for WtW^{1-2} and PtP^{1-2} coupling schemes for OV MV and UN MV BPL topology classes, respectively

Indicative BPL Topology Name (OV MV Capacity / UN MV Capacity in Mbps)	**BPL Topology Class Description**	**Percentage Change (%)**			
		Initial Statistical Hybrid Model		**Modified Statistical Hybrid Model**	
		Best Channel Attenuation Statistical Distribution		**Empirical Channel Attenuation Statistical Distribution**	
		OV MV (Weibull)	UN MV (Wald)	OV MV	UN MV
Urban case A (232 / 550)	Typical BPL urban class	1.72	0.01	0.10	0.12
Urban case B (193 / 465)	Aggravated BPL urban	0.66	0.04	0.28	0.12
Suburban case (278 / 582)	BPL suburban class	-0.27	0.003	0.09	0.05
Rural case (317 / 613)	BPL rural class	-0.20	0.0005	0.02	0.03
Average Absolute Percentage Change (%)		**0.71**	**0.02**	**0.12**	**0.08**

Table 7
Same with Table 3 but for $MtM_{0.8\_-0.1\_-0.1}^{1-2-3}$ coupling scheme for OV MV and UN MV BPL topology classes

Indicative BPL Topology Name (OV MV Capacity / UN MV Capacity in Mbps)	**BPL Topology Class Description**	**Percentage Change (%)**			
		Initial Statistical Hybrid Model		**Modified Statistical Hybrid Model**	
		Best Channel Attenuation Statistical Distribution		**Empirical Channel Attenuation Statistical Distribution**	
		OV MV (Weibull)	UN MV (Wald)	OV MV	UN MV
Urban case A (243 / 571)	Typical BPL urban class	1.60	0.01	0.26	0.12
Urban case B (203 / 487)	Aggravated BPL urban	0.34	0.03	0.51	0.12
Suburban case (290 / 603)	BPL suburban class	-0.27	0.003	0.16	0.04
Rural case (327 / 635)	BPL rural class	-0.12	0.0004	0.44	0.03
Average Absolute Percentage Change (%)		**0.58**	**0.01**	**0.34**	**0.08**

- Also in the case of different coupling schemes, the same trade-off relation between the computation / comparison time and the capacity estimation accuracy occurs during the selection of the initial and modified statistical hybrid model. With reference to the average absolute percentage change of Tables 3, 6 and 7, Weibull and Wald channel attenuation statistical distributions remain a permanent selection when the OV MV and UN MV BPL topology classes are examined,

respectively, but Empirical channel attenuation statistical distribution can very satisfactorily cope with both distribution power grid types.

Concluding this Section, the main disadvantage that has been highlighted in [6] is mitigated in this paper when relatively high EMI policies occur; without estimating MLEs and without losing MLE computation and comparison time, the Empirical channel attenuation statistical distribution can successfully estimate the capacity of OV MV and UN MV BPL topology classes by achieving results that are better in at least the half of the cases in comparison with the respective results of the best channel attenuation statistical distribution of the initial statistical hybrid model. Even in the cases where the Empirical channel attenuation statistical distribution does not achieve the best capacity estimation results, the performance differences in comparison with the best channel attenuation statistical distribution remain limited.

6. Conclusions

In this paper, the performance results of the modified statistical hybrid model have been compared against the results of the initial statistical hybrid model when various scenarios occur such as different power grid types, BPL topology classes, EMI policies and coupling schemes. In fact, based on the benchmark of [6], the Empirical channel attenuation statistical distribution has been compared against the Gaussian, Lognormal, Wald, Weibull and Gumbel channel attenuation statistical distributions with reference to the aforementioned scenarios. With reference to the capacity metrics of percentage change and average absolute percentage change as well as the first rule of thumb, the Empirical channel attenuation statistical distribution of the modified hybrid statistical model better estimates the capacity of the OV MV BPL topology classes in comparison with the Weibull channel attenuation statistical distribution of the initial statistical hybrid model when the default operation are assumed. Also, the capacity estimation results of the Empirical channel attenuation statistical distribution of the modified hybrid statistical model remain comparable to the ones of the Wald channel attenuation statistical distribution. Note that Weibull and Wald channel attenuation statistical distributions achieve the best capacity estimation results when the initial statistical hybrid model is adopted and the default operation settings are assumed. When different EMI policies, which are more protective to the other telecommunications services that coexist with BPL systems and are characterized by relatively lower IPSD limits (e.g., German Reg TP NB30 and BBC/NATO proposal), are assumed, same results concerning the capacity estimation result comparison between the Empirical channel attenuation statistical distribution and the set of channel attenuation statistical distributions of the initial statistical hybrid model occur although the percentage change and average absolute percentage change significantly increase as IPSD limits of the examined EMI policies decrease. In addition, the same number of unsuccessful capacity estimations approximately occurs between the Empirical channel attenuation statistical distribution and the best channel attenuation statistical distribution of the initial statistical hybrid model in relation with the percentage change. In the scenario of different coupling schemes, the impact of the different coupling schemes remains negligible on the percentage change and the average absolute percentage of all the channel attenuation statistical distributions in comparison with the respective impact of the different EMI policies. Again, the performance results of the Empirical channel attenuation statistical distribution coincide with the ones of the default operation settings scenario. In addition,

a trade-off between the computation / comparison time and the capacity estimation accuracy has been defined for the initial and modified statistical hybrid models. Hence, apart from the high capacity estimation performance of the Empirical channel attenuation statistical distribution, the modified statistical hybrid model achieves low computation time and zero comparison time since only one, say, the Empirical channel attenuation statistical distribution, occurs. Concluding this paper, the proposed modified statistical hybrid model with its Empirical channel attenuation statistical distribution offers a rapid and accurate upgrade of the initial statistical hybrid model that is considered as a valuable simulation tool towards the enrichment of BPL topology classes with realistic BPL topology members.

CONFLICTS OF INTEREST

The author declares that there is no conflict of interests regarding the publication of this paper.

References

[1] F. Xia, L. T. Yang, L. Wang, and A. Vinel, "Internet of things," *International Journal of Communication Systems*, vol. *25, no.* 9, pp. 1101-1102, 2012.

[2] L. Atzori, A. Iera, and G. Morabito, "The Internet of Things: A survey," *Elsevier Comput Netw.*, vol. 54, no. 15, pp. 2787–2805, 2010.

[3] H. Farhangi, "The path of the smart grid," *IEEE Power and Energy Magazine*, vol. 8, no. 1, pp. 18-28, 2010.

[4] A. S. de Beer, A. Sheri, H. C. Ferreira, and A. H. Vinck, "Channel frequency response for a low voltage indoor cable up to 1GHz," In *Power Line Communications and its Applications (ISPLC), 2018 IEEE International Symposium on*, pp. 1-6, 2018.

[5] A. G. Lazaropoulos, "Statistical Broadband over Power Lines Channel Modeling - Part 1: the Theory of the Statistical Hybrid Model," *Progress In Electromagnetics Research C*, vol. 92, pp. 1-16, 2019. [Online]. Available: http://www.jpier.org/PIERC/pierc92/01.19012902.pdf

[6] A. G. Lazaropoulos, "Statistical Broadband over Power Lines Channel Modeling - Part 2: the Numerical Results of the Statistical Hybrid Model," *Progress In Electromagnetics Research C*, vol. 92, pp. 17-30, 2019. [Online]. Available: http://www.jpier.org/PIERC/pierc92/02.19012903.pdf

[7] A. G. Lazaropoulos, "Underground Distribution BPL Connections with (N + 1)-hop Repeater Systems: A Novel Capacity Mitigation Technique," *Elsevier Computers and Electrical Engineering*, vol. 40, pp. 1813-1826, 2014.

[8] A. G. Lazaropoulos, "Review and Progress towards the Capacity Boost of Overhead and Underground Medium-Voltage and Low-Voltage Broadband over Power Lines Networks: Cooperative Communications through Two- and Three-Hop Repeater Systems," *ISRN Electronics*, vol. 2013, Article ID 472190, pp. 1-19, 2013. [Online]. Available: http://www.hindawi.com/isrn/electronics/aip/472190/

[9] A. G. Lazaropoulos, "Broadband over Power Lines (BPL) Systems Convergence: Multiple-Input Multiple-Output (MIMO) Communications Analysis of Overhead

and Underground Low-Voltage and Medium-Voltage BPL Networks (Invited Paper)," *ISRN Power Engineering*, vol. 2013, Article ID 517940, pp. 1-30, 2013. [Online]. Available: http://www.hindawi.com/isrn/power.engineering/2013/517940/

[10] A. Nazem and M. R Arshad, "An Approach in Full Duplex Digital Multipoint Systems Using Large Signal Power Line Communication," *Bentham Recent Patents on Electrical & Electronic Engineering*, vol. 6, no. 2, pp. 138-146, 2013.

[11] A. G. Lazaropoulos, "Deployment Concepts for Overhead High Voltage Broadband over Power Lines Connections with Two-Hop Repeater System: Capacity Countermeasures against Aggravated Topologies and High Noise Environments," *Progress in Electromagnetics Research B*, vol. 44, pp. 283-307, 2012. [Online]. Available: http://www.jpier.org/PIERB/pierb44/13.12081104.pdf

[12] A. G. Lazaropoulos and P. G. Cottis, "Transmission characteristics of overhead medium voltage power line communication channels," *IEEE Trans. Power Del.*, vol. 24, no. 3, pp. 1164-1173, Jul. 2009.

[13] A. G. Lazaropoulos and P. G. Cottis, "Capacity of overhead medium voltage power line communication channels," *IEEE Trans. Power Del.*, vol. 25, no. 2, pp. 723-733, Apr. 2010.

[14] A. G. Lazaropoulos and P. G. Cottis, "Broadband transmission via underground medium-voltage power lines-Part I: transmission characteristics," *IEEE Trans. Power Del.*, vol. 25, no. 4, pp. 2414-2424, Oct. 2010.

[15] A. G. Lazaropoulos and P. G. Cottis, "Broadband transmission via underground medium-voltage power lines-Part II: capacity," *IEEE Trans. Power Del.*, vol. 25, no. 4, pp. 2425-2434, Oct. 2010.

[16] A. G. Lazaropoulos, "Broadband transmission and statistical performance properties of overhead high-voltage transmission networks," *Hindawi Journal of Computer Networks and Commun.*, 2012, article ID 875632, 2012. [Online]. Available: http://www.hindawi.com/journals/jcnc/aip/875632/

[17] A. G. Lazaropoulos, "Towards Modal Integration of Overhead and Underground Low-Voltage and Medium-Voltage Power Line Communication Channels in the Smart Grid Landscape: Model Expansion, Broadband Signal Transmission Characteristics, and Statistical Performance Metrics (Invited Paper)," *ISRN Signal Processing*, vol. 2012, Article ID 121628, pp. 1-17, 2012. [Online]. Available: http://www.hindawi.com/isrn/sp/2012/121628/

[18] A. G. Lazaropoulos, "Towards Broadband over Power Lines Systems Integration: Transmission Characteristics of Underground Low-Voltage Distribution Power Lines," *Progress in Electromagnetics Research B*, vol. 39, pp. 89-114, 2012. [Online]. Available: http://www.jpier.org/PIERB/pierb39/05.12012409.pdf

[19] P. Amirshahi and M. Kavehrad, "High-frequency characteristics of overhead multiconductor power lines for broadband communications," *IEEE J. Sel. Areas Commun.*, vol. 24, no. 7, pp. 1292-1303, Jul. 2006.

[20] T. Sartenaer, "Multiuser communications over frequency selective wired channels and applications to the powerline access network" Ph.D. dissertation, Univ. Catholique Louvain, Louvain-la-Neuve, Belgium, Sep. 2004.

[21] T. Calliacoudas and F. Issa, ""Multiconductor transmission lines and cables solver," An efficient simulation tool for plc channel networks development," presented at the *IEEE Int. Conf. Power Line Communications and Its Applications*, Athens, Greece, Mar. 2002.

[22] T. Sartenaer and P. Delogne, "Deterministic modelling of the (Shielded) outdoor powerline channel based on the multiconductor transmission line equations," *IEEE J. Sel. Areas Commun.*, vol. 24, no. 7, pp. 1277-1291, Jul. 2006.

[23] FCC, "In the Matter of Amendment of Part 15 regarding new requirements and measurement guidelines for Access Broadband over Power Line Systems," FCC 04-245 Report and Order, Jul. 2008.

[24] A. Milioudis, G. Andreou, and D. Labridis, "Optimum transmitted power spectral distribution for broadband power line communication systems considering electromagnetic emissions," *Elsevier Electric Power Systems Research*, vol. 140, pp. 958–964, 2016. DOI: 10.1016/j.epsr.2016.03.047

[25] A. G. Lazaropoulos, "A Panacea to Inherent BPL Technology Deficiencies by Deploying Broadband over Power Lines (BPL) Connections with Multi-Hop Repeater Systems," *Bentham Recent Advances in Electrical & Electronic Engineering*, vol. 10, no. 1, pp. 30-46, 2017.

[26] http://matlabtricks.com/post-44/generate-random-numbers-with-a-given-distribution

[27] http://www.av8n.com/physics/arbitrary-probability.htm

[28] A. G. Lazaropoulos, "Broadband Performance Metrics and Regression Approximations of the New Coupling Schemes for Distribution Broadband over Power Lines (BPL) Networks," *Trends in Renewable Energy*, vol. 4, no. 1, pp. 43-73, Jan. 2018. [Online]. Available: http://futureenergysp.com/index.php/tre/article/view/59/pdf

[29] A. W. van der Vaart, *Asymptotic Statistics*. Cambridge Series in Statistical and Probabilistic Mathematics, Cambridge University Press, Cambridge, 1998. ISBN: 0-521-49603-9; 0-521-78450-6

[30] N. Suljanović, A. Mujčić, M. Zajc, and J. F. Tasič, "Approximate computation of high-frequency characteristics for power line with horizontal disposition and middle-phase to ground coupling," *Elsevier Electr. Power Syst. Res.*, vol. 69, pp. 17-24, Jan. 2004.

[31] OPERA1, D5: Pathloss as a function of frequency, distance and network topology for various LV and MV European powerline networks. IST Integrated Project No 507667, Apr. 2005.

[32] N. Suljanović, A. Mujčić, M. Zajc, and J. F. Tasič, "High-frequency characteristics of high-voltage power line," in *Proc. IEEE Int. Conf. on Computer as a Tool*, Ljubljana, Slovenia, Sep. 2003, pp. 310-314.

[33] N. Suljanović, A. Mujčić, M. Zajc, and J. F. Tasič, "Power-line high-frequency characteristics: analytical formulation," in *Proc. Joint 1st Workshop on Mobile Future & Symposium on Trends in Communications*, Bratislava, Slovakia, Oct. 2003, pp. 106-109.

[34] W. Villiers, J. H. Cloete, and R. Herman, "The feasibility of ampacity control on HV transmission lines using the PLC system," in *Proc. IEEE Conf. Africon*, George, South Africa, Oct. 2002, vol. 2, pp. 865-870.

[35] P. Amirshahi, "Broadband access and home networking through powerline networks" Ph.D. dissertation, Pennsylvania State Univ., University Park, PA, May 2006.

[36] OPERA1, D44: Report presenting the architecture of plc system, the electricity network topologies, the operating modes and the equipment over which PLC access system will be installed, IST Integr. Project No 507667, Dec. 2005.

[37] J. Anatory, N. Theethayi, R. Thottappillil, M. M. Kissaka, and N. H. Mvungi, "The influence of load impedance, line length, and branches on underground cable Power-Line Communications (PLC) systems," *IEEE Trans. Power Del.*, vol. 23, no. 1, pp. 180-187, Jan. 2008.

[38] J. Anatory, N. Theethayi, and R. Thottappillil, "Power-line communication channel model for interconnected networks-Part II: Multiconductor system," *IEEE Trans. Power Del.*, vol. 24, no. 1, pp. 124-128, Jan. 2009.

[39] J. Anatory, N. Theethayi, R. Thottappillil, M. M. Kissaka, and N. H. Mvungi, "The effects of load impedance, line length, and branches in typical low-voltage channels of the BPLC systems of developing countries: transmission-line analyses," *IEEE Trans. Power Del.*, vol. 24, no. 2, pp. 621-629, Apr. 2009.

[40] T. Banwell and S. Galli, "A novel approach to accurate modeling of the indoor power line channel—Part I: Circuit analysis and companion model," *IEEE Trans. Power Del.*, vol. 20, no. 2, pp. 655-663, Apr. 2005.

[41] W. Villiers, J. H. Cloete, L. M. Wedepohl, and A. Burger, "Real-time sag monitoring system for high-voltage overhead transmission lines based on power-line carrier signal behavior," *IEEE Trans. Power Del.*, vol. 23, no. 1, pp. 389-395, Jan. 2008.

[42] NTIA, "Potential interference from broadband over power line (BPL) systems to federal government radio communications at 1.7-80 MHz Phase 1 Study Vol. 1," NTIA Rep. 04-413, Apr. 2004.

[43] M. Gebhardt, F. Weinmann, and K. Dostert, "Physical and regulatory constraints for communication over the power supply grid," *IEEE Commun. Mag.*, vol. 41, no. 5, pp. 84-90, May 2003.

[44] NATO, "HF Interference, Procedures and Tools (Interférences HF, procédures et outils) Final Report of NATO RTO Information Systems Technology," RTO-TR-ISTR-050, Jun. 2007.

[45] A. G. Lazaropoulos, "The Impact of Noise Models on Capacity Performance of Distribution Broadband over Power Lines Networks," *Hindawi Computer Networks and Communications*, vol. 2016, Article ID 5680850, 14 pages, 2016. doi:10.1155/2016/5680850. [Online]. Available: http://www.hindawi.com/journals/jcnc/2016/5680850/

[46] A. G. Lazaropoulos, "Capacity Performance of Overhead Transmission Multiple-Input Multiple-Output Broadband over Power Lines Networks: The Insidious Effect of Noise and the Role of Noise Models (Invited Paper)," *Trends in Renewable Energy*, vol. 2, no. 2, pp. 61-82, Jun. 2016. [Online]. Available: http://futureenergysp.com/index.php/tre/article/view/23

[47] A. G. Lazaropoulos, "New Coupling Schemes for Distribution Broadband over Power Lines (BPL) Networks," *Progress in Electromagnetics Research B*, vol. 71, pp. 39-54, 2016. [Online]. Available: http://www.jpier.org/PIERB/pierb71/02.16081503.pdf

[48] A. G. Lazaropoulos, "Designing Broadband over Power Lines Networks Using the Techno-Economic Pedagogical (TEP) Method–Part I: Overhead High Voltage Networks and Their Capacity Characteristics (Invited Review Article)," *Trends in Renewable Energy*, vol. 1, no. 1, pp. 16-42, Mar. 2015. [Online]. Available: http://futureenergysp.com/index.php/tre/article/view/2

[49] A. G. Lazaropoulos, "Overhead and Underground MIMO Low Voltage Broadband over Power Lines Networks and EMI Regulations: Towards Greener Capacity Performances," *Elsevier Computers and Electrical Engineering*, vol. 39, pp. 2214-2230, 2013.

[50] D. Fenton and P. Brown, "Some aspects of benchmarking high frequency radiated emissions from wireline communications systems in the near and far fields," in *Proc. IEEE Int. Symp. on Power Line Communications and its Applications*, Malmö, Sweden, Apr. 2001, pp. 161-167.

Trends in Renewable Energy
OPEN ACCESS ISSN: 2376-2144
Peer-Reviewed Article futureenergysp.com/index.php/tre

Catalytic Pyrolysis of Kapok Fiber for Production of Olefins

Qi Qiu,* Yingen Cai, Qiuling Ye, Weizhong Lv

College of Chemistry and Environmental Engineering, Shenzhen University, Shenzhen 518060, China

Received May 30, 2019; Accepted July 12, 2019; Published July 14, 2019

Pyrolysis of kapok fibers over mesoporous molecular sieves of MCM-41, Zr-MCM-41 and Cr-MCM-41 (the mole ratio of Si:Zr or Si/Cr=50) was studied by using pyrolysis-gas chromatography-mass spectrometry (Py-GC/MS). Pure silicon MCM-41 showed weak acidity during pyrolysis with furfural as the main product. Zr-MCM-41 showed the dual-functionality of acid and base with both furfural and hydroxy acetone present in the products. Cr-MCM-41 was more acidic with more furfural produced. The optimal conditions for producing olefins were found to be 600°C and the ratio of kapok fiber to catalyst being 1:10 with the Zr-MCM-41 catalyst. The main products obtained via pyrolysis of kapok fiber were acetic acid, furfural, 2,4-di-tert-butylphenol, olefins, and alkanes. The excess of the catalyst and the high temperature of the reaction had certain effects on the pyrolysis of biomass to produce olefins, such as 1-decene, 1-dodecene, 1-undecene, 1-tridecene and heptadecane.

Keywords: Kapok fibers; GCMS; Pyrolysis; MCM-41; Zr-MCM-41; Olefin

Introduction

Energy sources are not only closely related to the country's political stability and economic development, but also the motivating power for the economic growth and the national progress [1]. The advance of energy technologies is an important driving force for the development of the human society.

The Earth has not only a large amount of fossil energy, namely coal, oil and natural gas, but also a large amount of renewable clean energy such as hydropower, wind and sunlight. The traditional fossil fuels greatly promoted the development of human society. After the industrial revolution, due to the relatively low cost of the fossil fuels, people's interest in biomass had greatly reduced. Global energy development is over-reliant on the fossil energy [2]. For example, the fossil coal is being continuously mined, resulting in growing number of problems, such as resource constraints and excessive CO_2 emissions. The resultant greenhouse effect, global warming, environmental pollution, and other issues seriously threaten the survival and the development of human beings. Due to these concerns, scientists have raised interest in renewable energy. In the past few decades, researchers have been dedicated for exploring and developing new renewable energy sources, including the solar energy, wind energy, hydropower generation, biomass energy, geothermal energy, and the ocean energy [3]. Among them, the biomass energy (*i.e.,* bioenergy), accounting for 14% of the world's total primary energy consumption, is

**Corresponding author:* qqiu@szu.edu.cn

Tr Ren Energy, 2019, Vol.5, No.2, 218-228. doi: 10.17737/tre.2019.5.2.0097

the fourth largest energy source in the world, playing an important role in the entire energy system [4].

So far, the world's annual biomass production has reached 180 billion tons, or 3×10^{22} J, 10 times the actual energy consumption in the world. Under the ideal conditions, the biomass potential on Earth could reach 180~200 times the actual energy consumption [5, 6]. The use of the biomass as an energy and chemical source is conducive to not only the energy conservation and emission reduction, but also the adjustment of the energy consumption while promoting the economic development. In order to further develop the bioenergy technology and effectively improve the biomass conversion, it is indispensable to explore the principle of the conversion process [7].

Pyrolysis is one of the mostly studied biomass utilization technologies to produce energy products and fine chemicals [8, 9]. Catalytic pyrolysis has the advantages of selective conversion and fast reaction, a promising method to improve the quality of final products [10, 11]. For this study, kapok fibers were catalytically pyrolyzed over mesoporous molecular sieves of MCM-41 modified with Zr and Cr. The impact of these catalysts on the pyrolysis of kapok fiber was investigated by using pyrolysis-gas chromatography-mass spectrometry (Py-GC/MS).

Materials and Methods

Materials

Kapok fibers were collected locally at Shenzhen, China during the spring 2018. The kapok fibers were dried at 100℃ for 24 h to remove the moisture. The dried fibers were ground to fine powders, with the compositions shown in Table 1. The fibers contain cellulose, lignin, pentosan (hemicellulose), and extractives.

Table 1. The compositions of the kapok fiber (wt%)

Ash	Extractives			Cellulose	Klason lignin	Pentosan
	Hot water	NaOH	Phenyl			
1.43	4.10	26.96	1.93	43.73	11.36	37.43

Catalysts of mesoporous molecular sieves of MCM-41, Zr-MCM-41 and Cr-MCM-41 were provided by the Wuhan Institute of Technology [12]. The mole ratios of Si/Zr in Zr-MCM-41 and Si/Cr in Cr-MCM-41 were 50.

Pyrolysis Coupled with Gas Chromatograph/Mass Spectrometer (Py-GC/MS)

Prior to pyrolysis, the kapok fibers were mixed with the catalyst of MCM-41, Zr-MCM-41 or Cr-MCM-41 to make a feedstock-to-catalyst weight ratio of 1:2，2:1, 1:10 and 10:1. The mixtures were ground in a mortar and placed in an oven at 100°C for 10 h.

Pyrolysis of kapok fibers was conducted in a sample cup of Frontier PY-2020iD pyrolyzer (Fukushima, Japan). Prior to the pyrolysis, a sample of 0.5 mg was weighted by using a METTLER TOLEDO XP6 Automated-S microbalance (Columbus, OH, USA). For each experiment, the pyrolyzer was pre-heated to the desired temperature (400ºC, 500ºC or 600ºC), and then purged with ultra-purity helium to remove oxygen. The pre-weighted sample was allowed to drop into the pyrolyzer, whereby the sample was pyrolyzed for 30 s. The volatilized products were injected directly into a Shimadzu

GCMS-QP2010 gas chromatograph/mass spectrometer (Shimadzu, Japan) equipped with an Agilent DB-5MS capillary column (Santa Clara, CA, USA).

Results and Discussion

Impact of Ratio of Feedstock to Catalyst

The effect of the ratio of the feedstock to catalyst (R) on pyrolysis was explored. Firstly, catalytic pyrolysis was conducted with Zr-MCM-41 at the feedstock to a catalyst ratio (R) of 1:2 and 2:1 at the pyrolysis temperature of 600°C. The total ion chromatogram (TIC) of these two conditions are shown in Figure 1. The results showed an obvious profile change upon the change in the catalyst ratio. Therefore, R was further decreased to 1:10. This ratio was compared to the R of 10:1, with the resultant TIC shown in Figure 2. Figure 2 exhibits evidently higher peak height, higher peak area, and more abundant products at the ratio of the feedstock to catalyst of 1:10. Consequently, a lower R value is preferred in the subsequent experiment.

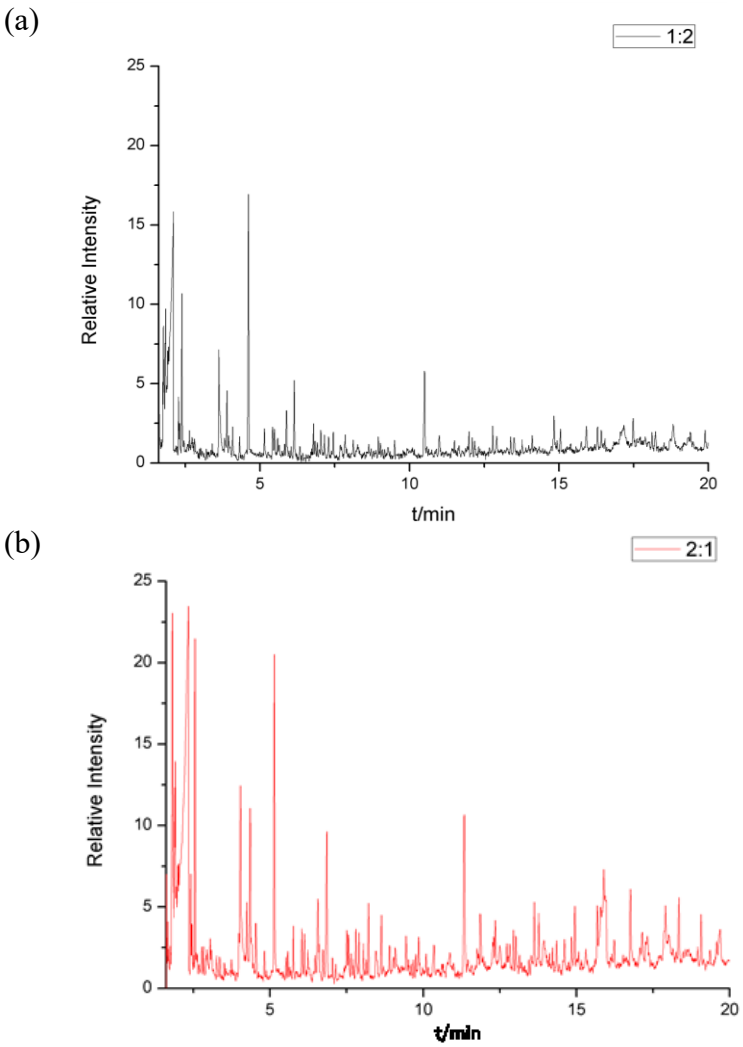

Figure 1. TIC of pyrolysis of kapok fibers with a feedstock to Zr-MCM-41 ratio of (a) 1:2 and (b) 2:1

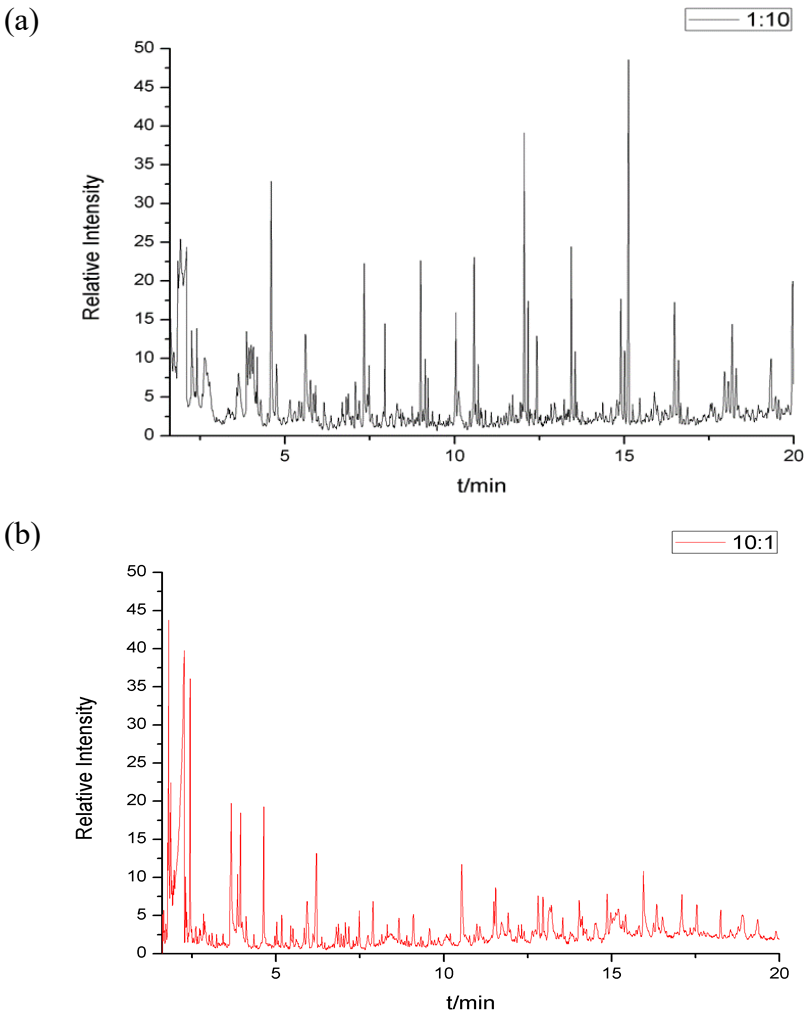

Figure 2. TIC of pyrolysis of kapok fibers with a feedstock to Zr-MCM-41 ratio of (a) 1:10 and (b) 10:1

Impact of Pyrolysis Temperature

The biomass components are difficult to be cracked under low pyrolysis temperature. Contrarily, when the pyrolysis temperature is too high, the pyrolytic products become more complicated with more gaseous products. Accordingly, pyrolysis temperature was chosen as 400ºC, 500ºC, and 600ºC. Figure 3 shows the TIC of catalytic pyrolysis of kapok fibers over Zr-MCM-41 with R =1:10.

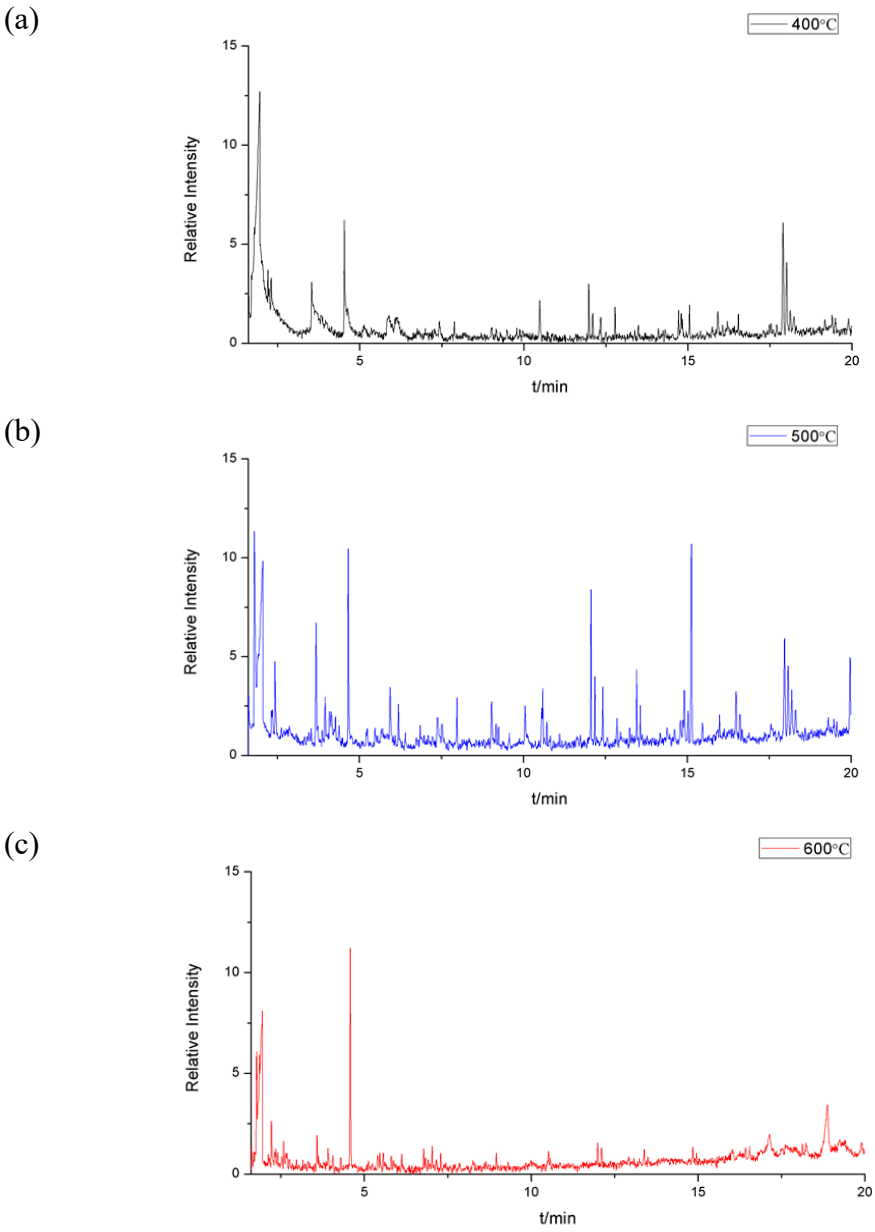

Figure 3. TICs of pyrolysis of kapok fibers at the feedstock to Zr-MCM-41 ratio of 1:10 and (a) 400°C, (b) 500°C and (c) 600°C

The number of chemicals produced at 400°C was less, and it is apparent that the kapok fiber was not fully catalytically cracked. The reactions at 500°C showed more chemicals than that of 400°C, though there were similar small molecular chemicals. At 600°C, cracking of the feedstock was relatively complete, and new substances were formed obviously. Therefore, the following experiments were pyrolyzed at 600°C.

Impact of MCM-41 Catalysts

The experiments on MCM-41 catalysts were conducted at R = 1:10 and 600°C for 30 s. The TICs of MCM-41, Zr-MCM-41 and Cr-MCM-41 are shown in Figure 4, while produced chemicals are summarized in Tables 2- 4, respectively.

(a)

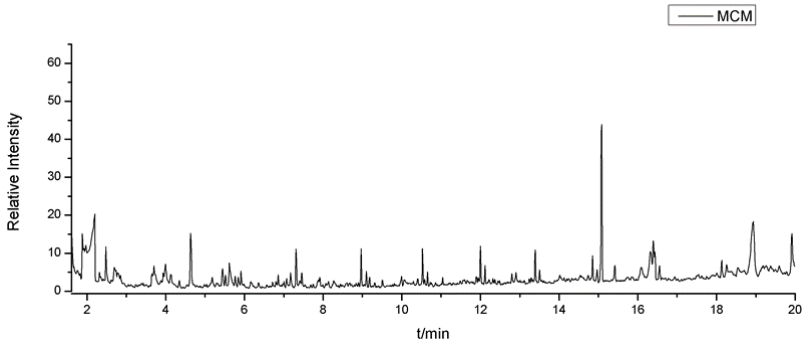

(b)

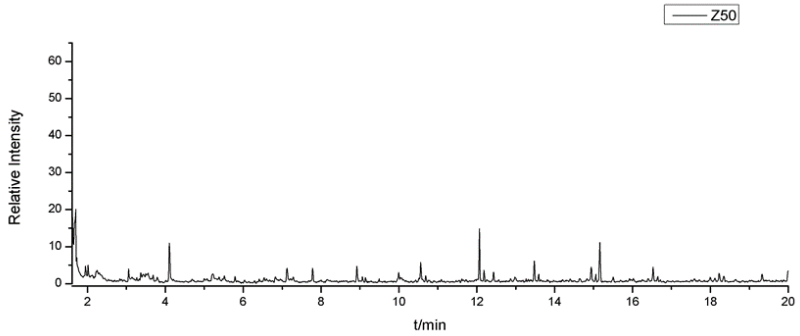

(c)

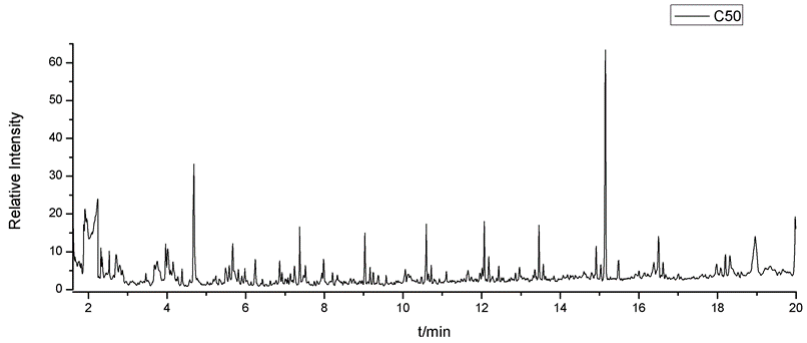

Figure 4. TICs of pyrolysis of kapok fibers over (a) MCM-41, (b) Zr-MCM-41 and (c) Cr-MCM-41 at R = 1:10 and 600°C

Table 2. Pyrolytic products obtained from catalytic (MCM-41) Py-GC-MS analysis

RT (min)	Possible chemical	Similarity (%)	Formula	Areas (%)
2.196	Acetic acid	94	$C_2H_4O_2$	21.55
3.993	1-Octene	91	C_8H_{16}	1.94
4.634	Furfural	83	C_5H_6O	6.87
5.620	1-Nonene	94	C_9H_{18}	3.7
7.316	1-Decene	95	$C_{10}H_{20}$	3.73
8.967	1-Undecene	95	$C_{11}H_{22}$	3.36
9.101	Undecane	92	$C_{11}H_{24}$	1.36
10.529	1-Dodecene	94	$C_{12}H_{24}$	3.3
10.653	Dodecane	93	$C_{12}H_{26}$	1.02
12.002	(3Z)-3-Hexadecene	91	$C_{16}H_{32}$	2.95
12.116	Tridecane	92	$C_{13}H_{28}$	1.47
13.394	1-Pentadecene	95	$C_{15}H_{30}$	2.48
14.850	Pentadecene	94	$C_{15}H_{30}$	2.11
15.080	2,4-Di-tert-butylphenol	96	$C_{14}H_{22}O$	18.1
16.320	1-Heptadecene	91	$C_{17}H_{34}$	5.87
18.931	Oleic acid	85	$C_{18}H_{34}O_2$	20.19

Table 3. GC-MS analysis of pyrolytic products obtained with Zr-MCM-41

RT (min)	Possible chemical	Similarity (%)	Formula	Areas (%)
2.096	Acetic acid	91	$C_2H_4O_2$	11.9
2.251	4-Methyl-2-penten-1-ol	84	$C_6H_{12}O$	1.32
2.401	Hydroxy acetone	86	$C_3H_6O_2$	1.06
4.591	Furfural	89	$C_5H_4O_2$	8.14
4.750	1-Heptene,2,4-dimethyl-	91	C_9H_{18}	2.38
5.604	1-Nonene	95	C_9H_{18}	4.51
7.332	1-Decene	96	$C_{10}H_{20}$	4.67
7.944	2-Ethylhexanol	95	$C_8H_{18}O$	2.01
9.000	1-Undecene	96	$C_{11}H_{22}$	3.9
9.134	Undecane	94	$C_{11}H_{24}$	1.58
10.034	4-Methoxystyrene	88	$C_9H_{10}O$	3.36
10.571	1-Dodecene	95	$C_{12}H_{24}$	4
10.696	Dodecane	95	$C_{12}H_{26}$	1.31
12.051	1-adamantancarboxylic acid, 5-tetradecyl ester	82	$C_{25}H_{44}O_2$	6.3
12.163	Tetradecane	88	$C_{14}H_{30}$	2.78
12.428	o-phthalic anhydride	93	$C_8H_4O_3$	2.69
13.442	(3Z)-3-Hexadecene	96	$C_{16}H_{32}$	3.36
13.549	Tetradecane	94	$C_{14}H_{30}$	1.38
14.898	1-Pentadecene	96	$C_{15}H_{30}$	2.78
15.012	Pentadecane	95	$C_{15}H_{32}$	1.9
15.124	2,4-Di-tert-butylphenol	97	$C_{14}H_{22}O$	10.14
16.481	1-Heptadecene	95	$C_{17}H_{34}$	6.34
16.599	Hexadecane	93	$C_{16}H_{34}$	1.83
18.300	Nonadecane	91	$C_{19}H_4O$	1.7
19.330	Myristic acid	91	$C_{14}H_{28}O_2$	2.2
19.464	(1-Methyldecyl)cyclohexane	87	$C_{17}H_{34}$	0.93
19.553	2-hexyl-1-Decanol	88	$C_{16}H_{34}O$	0.77
19.964	1-Nonadecene	96	$C_{19}H_{38}$	4.68

Table 4. GC-MS analysis of pyrolytic products obtained with Cr-MCM-41

RT (min)	Possible chemical	Similarity (%)	Formula	Areas (%)
2.236	Acetic acid glacial	94	$C_2H_4O_2$	21.53
4.683	Furfural	95	$C_5H_4O_2$	12.54
5.667	1-Nonene	95	C_9H_{18}	2.85
7.374	1-Decene	95	$C_{10}H_{20}$	4.39
9.031	1-Undecene	95	$C_{11}H_{22}$	3.7
10.594	1-Dodecene	94	$C_{12}H_{24}$	5.17
12.068	2-Dodecenal, (2E)-	84	$C_{12}H_{22}O$	4.33
12.181	Tridecane	91	$C_{13}H_{28}$	1.77
13.46	(3Z)-3-Hexadecene	95	$C_{16}H_{32}$	3.71
14.915	1-Pentadecene	95	$C_{15}H_{30}$	2.5
15.150	2,4-Di-tert-butylphenol	97	$C_{14}H_{22}O$	21.59
16.500	1-Heptadecene	94	$C_{17}H_{34}$	3.77
18.199	1-Nonadecene	94	$C_{19}H_{38}$	2.31
18.959	Oleic acid	85	$C_{18}H_{34}O_2$	9.83

Analysis of the above experimental results indicated that there were numerous products obtained via catalytic pyrolysis of kapok fibers. Acetic acid was obtained in all cases with basically the highest peak area. Furfural was another major product. In addition, 2,4-di-tert-butylphenol was produced during pyrolysis using different catalysts with a retention time of ~15 mins. After the retention time of ~5.6 mins, more olefins were formed, including 1-decene, 1-dodecene, 1-undecene, 1-tridecene, heptadecene, etc. Those that catalytic pyrolysis over the modified molecular sieve catalyst contributed to the production of olefins.

CONCLUSIONS

Catalytic pyrolysis of kapok fibers was investigated with various MCM-41 catalysts, the feedstock to catalyst ratios, and the reaction temperatures.

(1) The main products obtained via pyrolysis of kapok fiber were acetic acid, furfural, 2,4-di-tert-butylphenol, olefins and alkanes.

(2) Pure silicon MCM-41 showed its weak acidity during the reaction with the furfural as the main product. Zr-MCM-41 showed the dual-functionality of acid and base, and both furfural and hydroxy acetone were present in the products. Cr-MCM-41 was more acidic and resulted in more furfural.

(3) The excess of the catalyst and the high temperature of the reaction had certain effects on the pyrolysis of biomass to produce olefins.

ACKNOWLEDGMENTS

This work was partially supported by Natural Science Foundation of Guangdong Province (2017A030310133) and the College of Chemistry and Environmental Engineering at Shenzhen University.

CONFLICTS OF INTEREST

The authors declare that there is no conflict of interests regarding the publication of this paper.

REFERENCES

[1] Burke, M. J., and Stephens, J. C. (2018). Political power and renewable energy futures: A critical review. *Energy Research & Social Science*, 35, 78-93. DOI: https://doi.org/10.1016/j.erss.2017.10.018

[2] Team, G. E. A. W. (2012). Global Energy Assessment. *Cambridge Books*.

[3] Quaschning, V. V. (2019). *Renewable energy and climate change*, Wiley.

[4] Yang, X., Zhang, R., Fu, J., Geng, S., Cheng, J. J., and Sun, Y. (2014). Pyrolysis kinetic and product analysis of different microalgal biomass by distributed activation energy model and pyrolysis–gas chromatography–mass spectrometry. *Bioresource Technology*, 163, 335-342. DOI: https://doi.org/10.1016/j.biortech.2014.04.040

[5] Kleijn, R., and van der Voet, E. (2010). Resource constraints in a hydrogen economy based on renewable energy sources: An exploration. *Renewable and Sustainable Energy Reviews*, 14(9), 2784-2795. DOI: https://doi.org/10.1016/j.rser.2010.07.066

[6] Qiu, Q., Zhang, B., and Lv, W. (2018). Green Energy based Thermochemical and Photochemical Hydrogen Production. *Int. J. Electrochem. Sci.*, 13, 6484-6502. DOI: 10.20964/2018.07.06

[7] Zhang, B., and Wang, Y. (2013). *Biomass Processing, Conversion and Biorefinery*, Nova Science Publishers, Inc., New York.

[8] Yang, C., Li, R., Zhang, B., Qiu, Q., Wang, B., Yang, H., Ding, Y., and Wang, C. (2019). Pyrolysis of microalgae: A critical review. *Fuel Processing Technology*, 186, 53-72. DOI: https://doi.org/10.1016/j.fuproc.2018.12.012

[9] Yang, C., Li, R., Cui, C., Wu, J., Ding, Y., Wu, Y., and Zhang, B. (2017). The pyrolysis of duckweed over a solid base catalyst: Py-GC/MS and TGA analysis. *Energy Sources, Part A*, 39(2), 177-183. DOI: 10.1080/15567036.2016.1214641

[10] Wang, H., Zhang, B., Xiu, S., Li, R., and Shi, J. (2016). Densification and Pyrolysis of Lignocellulosic Biomass for Renewable Energy. *Current Organic Chemistry*, 20(23), 2480-2488.

[11] Qiu, Q., Huang, M., Zheng, W., Xuan, C., Wan, Y., Zhang, B., Luo, Z., and Lv, W. (2017). Impact of molar ratio of total metal ions to precipitant on YAG:Ce nanophosphors synthesized by reverse titration coprecipitation. *Ceramics International*, 43(12), 8730-8734. DOI: https://doi.org/10.1016/j.ceramint.2017.04.004

[12] Luo, H., Song, Z., Wu, J., Zhang, B., Yang, C., and Ding, Y. (2019). Effect of Modified Mesoporous Molecular Sieve Zr-MCM-41 on Pyrolysis of Cellulose. *Journal of Wuhan Institute of Technology*, 41(1), 40-45.

CALL FOR PAPERS

Trends in Renewable Energy

ISSN Print: 2376-2136 ISSN online: 2376-2144

http://futureenergysp.com/index.php/tre/

Trends in Renewable Energy (TRE) is an open accessed, peer-reviewed semi-annual journal publishing reviews and research papers in the field of renewable energy technology and science. The aim of this journal is to provide a communication platform that is run exclusively by scientists. This journal publishes original papers including but not limited to the following fields:

- ✧ Renewable energy technologies
- ✧ Catalysis for energy generation, Green chemistry, Green energy
- ✧ Bioenergy: Biofuel, Biomass, Biorefinery, Bioprocessing, Feedstock utilization, Biological waste treatment,
- ✧ Energy issues: Energy conservation, Energy delivery, Energy resources, Energy storage, Energy transformation, Smart Grid
- ✧ Environmental issues: Environmental impacts, Pollution
- ✧ Bioproducts
- ✧ Policy, etc.

We publish the following article types: peer-reviewed reviews, mini-reviews, technical notes, short-form research papers, and original research papers.

The article processing charge (APC), also known as a publication fee, is fully waived for the Trends in Renewable Energy.

Call for Editorial Board Members

We are seeking scholars active in a field of renewable energy interested in serving as volunteer Editorial Board Members.

Qualifications

Ph.D. degree in related areas, or Master's degree with a minimum of 5 years of experience. All members must have a strong record of publications or other proofs to show activities in the energy related field.

If you are interested in serving on the editorial board, please email CV to editor@futureenergysp.com.